Bragg Spectroscopy of a Strongly Interacting Fermi Gas

A thesis submitted for the degree of

Doctor of Philosophy

by

Gopisankararao Veeravalli

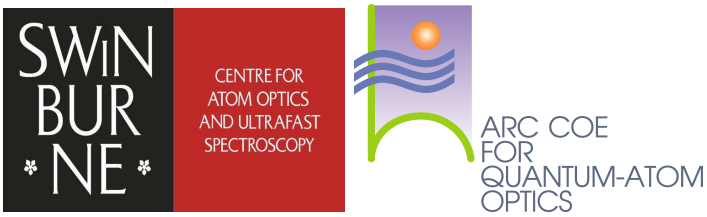

Centre for Atom Optics and Ultrafast Spectroscopy and

ARC Centre of Excellence for Quantum-Atom Optics

Faculty of Engineering and Industrial Sciences

Swinburne University of Technology

Melbourne, Australia

July 26, 2009

"Life is like a box of chocolates, you never know what you are going to get."

— Mrs. Gump in the movie 'Forrest Gump'

Declaration

I, Gopisankararao Veeravalli, declare that this thesis entitled:

"Bragg spectroscopy of a strongly interacting Fermi gas"

is my own work and has not been submitted previously, in whole or in part, in respect of any other academic award.

Gopisankararao Veeravalli

Centre for Atom Optics and Ultrafast Spectroscopy
Faculty of Engineering and Industrial Sciences
Swinburne University of Technology
Melbourne, Australia

Dated this day, July 26, 2009

- To my family

Abstract

The main objective of the research described in this thesis is to probe the many-body quantum effects in a strongly interacting Fermi gas using Bragg spectroscopy. An enriched source of Lithium-6 atoms is used to probe these properties. The broad Feshbach resonance of the two lowest hyperfine levels of ^{6}Li at a magnetic field of 834G is exploited to precisely control the interactions between the atoms.

In our experiments, a beam of hot ^{6}Li atoms produced by an oven is cooled using a σ^- Zeeman slower in an ultra-high vacuum environment. From this slowed atomic beam, 4% of the atoms are cooled and trapped in a magneto-optical trap (MOT) created by six perpendicularly intersecting near-resonant laser beams. This Doppler cooled MOT consists of 10^8 atoms at a temperature of 280 μK. A small fraction (1%) of atoms is then transferred from the MOT to a single optical dipole trap created by a 100 W fibre laser. To obtain the temperatures of degeneracy ($\approx$ 100 nK), the atomic sample is further evaporatively cooled in the presence of Feshbach magnetic fields, by reducing the intensity of the dipole trap laser with the help of a commercial PID controller. Once the degenerate gas is formed, the dipole trap is switched off and the gas is allowed to expand for a certain time of flight before taking an absorption image on a CCD camera for analysis.

At magnetic fields below the Feshbach resonance, the collisional interactions become repulsive and a bound molecular state exists for fermionic atoms with opposite spins. These bound fermions form a composite boson which follows bosonic statistics to

form a molecular Bose-Einstein Condensate (BEC). At magnetic fields above the Feshbach resonance, the interactions become attractive and no stable bound state exists. However at ultracold temperatures, a Bardeen-Cooper-Schrieffer (BCS) state is created through weak coupling between the fermions forming a 'Cooper pair'. When the field is tuned to the Feshbach resonance (unitarity), the scattering length of the atoms diverges and the interactions in the gas become universal. Under such conditions, correlated pairs are predicted to exist due to many-body quantum effects. The size of these pairs becomes comparable to the inter-particle distances, making this system an ideal test bed for studying superfluidity.

Bragg spectroscopy is designed and implemented to probe the composition of the particles at unitarity as well as their correlation properties across the BEC-BCS crossover. A comprehensive study of these properties across the Feshbach resonance is presented for the first time via Bragg scattering of the strongly interacting Fermi gas. The Bragg spectra are analysed in terms of the centre-of-mass displacement of the cloud along the direction of the Bragg pulse. A smooth transition from molecular to atomic spectra is observed with a clear signature of pairing at and above unitarity. Furthermore, the two-body correlations are characterised and their density dependence is measured across the broad Feshbach resonance.

Acknowledgements

During my four years at CAOUS, I met so many interesting and important people who have played a role in shaping both my personal and academic lives. It is a difficult task to acknowledge every one of them and I apologise if I miss out some names.

First and foremost I would like to thank my chief supervisors Prof. Peter Hannaford and Dr. Wayne Rowlands for giving me an opportunity to work in the lab of 'cold molecules'. I appreciate their confidence in offering me this job, as at that time I had no experience in experimental physics. I am also grateful for their unconditional support throughout my PhD work.

In my first year I worked on the 'photo-association of atomic rubidium' project with Heath Kitson, who introduced me to the Australian culture and 'language'. I couldn't have hoped for a better person who could teach me about the experimental techniques so liberally and patiently. He boosted my confidence to work independently by appreciating every simple task I completed. Following that year I joined the project on the 'creation of a molecular BEC', which was the first objective of my PhD. It was a pleasure to work with our postdoc Dr. Grainne Duffy and my colleague Jürgen Fuchs who have, among other things, shown me how to set up vacuum components.

It is not a coincidence that my co-ordinate supervisor Dr. Chris Vale joined our team in early 2007 and we got our first molecular BEC in May, 2007. Chris has brought a wealth of both experimental and theoretical knowledge to our lab. Due to his foresight we have overcome many technical difficulties. This thesis wouldn't have been successful without his timely contribution for which I am greatly indebted. In addition, I would like to thank Chris along with my chief supervisors for proof reading this thesis.

I am extremely fortunate that Paul Dyke and Eva Kuhnle have accompanied me in the lab for the past two years. They have worked hard to ensure that the experiment ran smoothly, sometimes even in my absence. I am thankful to them for spending long hours in taking the data. A special thanks to Eva for analysing some of the data using Matlab.

I would also like to thank the following CAOUS members: Shannon Whitlock for providing the Labview codes, Dr. Brenton Hall and Mandip Singh for designing the electronic circuits, Dr. Michael Volk for advising on the dipole traps, David McDonald for helping with Matlab, Michael Vanner for assisting with earlier Bragg experiments, Dr. Alexander Akoulchine for his suggestion to achieve stable beat frequency, Russell Anderson for teaching me Mathematica, Dr. Chris Ticknor for enhancing my theoretical knowledge, Dr. Michael Mark for his constructive comments in making my CV, Tatiana Tchernova for administrative support and finally Mark 'the magnificent' Kivinen for building the technical tools for our experiment.

Special thanks to Dr. Tom Edwards, Dr. Alex Mazzoloni and Dr. Don Ward Smith for offering a teaching assistantship which provided me with essential additional financial support.

My family has always supported me in all possible ways to help reach this stage. Without their constant support and trust in me I would not have fulfilled my dreams. To them I dedicate this work.

I reserve my final gratitude to the most important person in my life. I cannot thank my wife Bhakti enough for her patience and support during the time of this thesis.

Gopisankararao Veeravalli
Melbourne, Australia
July 26, 2009

Contents

List of Figures

Chapter 1

Introduction

1.1 Background

Ever since the first experimental realisation of long-lived bosonic molecules comprised of fermionic atoms [1, 2, 3, 4, 5] and the Bose-Einstein condensation of these molecules [6, 7, 8], the novel properties of these strongly interacting quantum many-body systems have attracted world-wide attention. These landmark experiments were made possible by the availability of so-called Feshbach resonances [9, 10, 11, 12] which allow the interactions between fermions with opposite spins to be tuned in a very precisely controlled manner. In addition, the techniques of laser cooling and trapping [13, 14, 15, 16] developed to achieve atomic BECs [17, 18, 19] have been applied to create strongly interacting Fermi gases in the laboratory [20, 21, 22, 23, 24, 25, 26]. The behaviour of such many-body interacting Fermi systems have many similarities to that of electrons in metals, superconductors [27], superfluids [28], white-dwarfs and neutron-stars. The fact that strongly interacting Fermi systems can be modelled and manipulated at will in an experimental laboratory makes the research of such systems of great fundamental significance.

At ultracold temperatures, the collisional properties of two-component Fermi gases

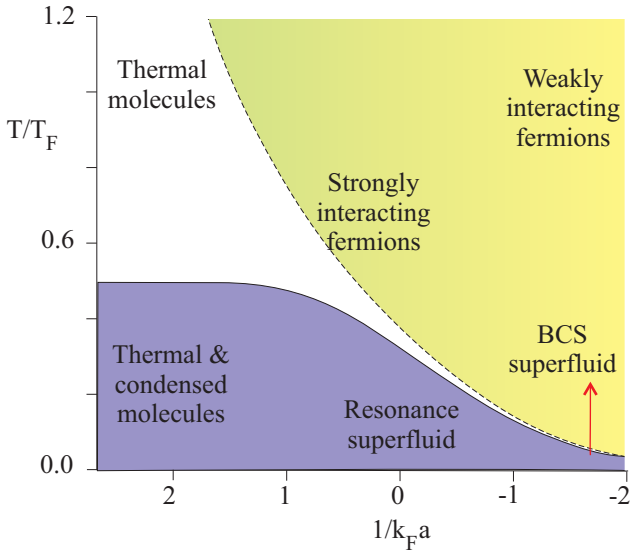

Figure 1.1: Phase diagram of interacting Fermi mixtures in a harmonic trap as a function of temperature T/T_{F} and interaction strength $1/k_{\mathrm{F}}a$ [29], where T_{F} is the Fermi temperature. The dashed line represents the characteristic temperature T^* for pair formation and the continuous line represents the critical temperature T_{c} for superfluid formation. (The plot is re-constructed from Fig. 14 of reference [30])

(spin-up and spin-down) are governed only by their s-wave scattering length a. With the use of a Feshbach resonance, this length can be tuned from a positive to a negative value, creating either a repulsive or an attractive interaction between the fermions. The interaction strength is quantified in terms of the dimensionless quantity $1/k_{\mathrm{F}}a$, where k_{F} is the Fermi wave vector. Figure 1.1 shows the phase space diagram across this crossover in terms of $1/k_{\mathrm{F}}a$. Fermions with opposite spins can form bosonic pairs below the characteristic temperature T^* (dashed line) and can be further cooled below the critical temperature T_{c} (solid line) to form a superfluid. Note that, except for $1/k_{\mathrm{F}}a > 0$, isolated correlated pairs cannot be formed as they are produced purely by many-body quantum effects. Also, it has been shown experimentally [23] that the crossover across the Feshbach resonance is continuous and reversible.

At the crossover $1/k_{\mathrm{F}}a = 0$, the scattering length diverges ($a \to \pm\infty$) and the properties of the system become universal [31, 32, 33, 34, 35, 36]. Under such conditions, strongly correlated fermionic pairs are formed. The size of these

pairs is comparable to the inter-particle distances which facilitates the formation of superfluidity at high temperatures. Thus, a system of strongly interacting Fermi gas provides an ideal platform to probe and understand high-temperature superconductivity in various types of materials [37]. This region ($-1 < 1/k_{\mathrm{F}}a < +1$) of the Feshbach resonance is referred to as unitarity.

When the interactions are attractive $1/k_{\mathrm{F}}a < 0$, weakly bound Cooper pairs are formed. This is analogous to the formation of electron pairs in a superconductor, first explained by Bardeen, Cooper and Schrieffer (BCS) using many-body mean-field theory [38]. These pairs are correlated in momentum space at the surface of the Fermi sea, whereas for momentum $k < k_{\mathrm{F}}$ pair formation is suppressed by Pauli blocking. In real space, these pairs are larger than the inter-particle separation making it experimentally difficult to detect them. Superfluidity is also possible in such systems, though at extremely low temperatures. This side of the Feshbach resonance is often referred to as the BCS side.

When the interactions are repulsive $1/k_{\mathrm{F}}a > 0$, a weakly bound molecular state becomes energetically stable in the presence of a Feshbach resonance. When a gas of two-component fermions is evaporatively cooled at a fixed value of a in a harmonic trap, molecules can be produced via three-body recombination [39]. Experimentally [3, 4], the lifetimes of these molecules are found to be of the order of tens of seconds, long enough to perform evaporative cooling. Because these molecules are composite bosons (consisting of two fermions), they can undergo a phase transition to form a molecular BEC which is a superfluid. This side of the Feshbach resonance is called the BEC side.

1.2 Motivation

It is clear from the previous section, that with the help of Feshbach resonances, the strength and type of interactions within a two-component Fermi gas can be varied very precisely. Due to the presence of interactions in a Fermi gas, correlated pairs are

formed [26, 40]. This eventually leads to the production of superfluidity across the BEC-BCS crossover [42, 43, 44]. The size of these pairs, however, varies from small to large compared to the inter-particle distances depending on the strength of the interaction [45]. One important step towards understanding the dynamic properties of these many-body systems is to quantify these pair correlations in a strongly interacting Fermi gas across the BEC-BCS crossover.

Experiments performed across the BEC-BCS crossover using radio-frequency (RF) spectroscopy [46] have either measured pair sizes [45] or pairing gaps [47, 41], whereas the experiment performed using photoemission spectroscopy has probed only single particle excitations [48]. The first pair correlation measurements between the pair of atoms dissociated from a bound molecule is performed by analysing the atom-shot noise from the time of flight absorption images [49]. However, in order to probe the pair correlations across the BEC-BCS crossover, Bragg spectroscopy has been suggested by various theoretical studies [50, 51, 52] for the following reasons. Unlike RF spectroscopy, during Bragg scattering the internal atomic states are unchanged, as a result there are no final state interactions shifts. Also, the momentum imparted to the gas in Bragg spectroscopy can be very large compared to the Fermi momentum ($\hbar k_{\mathrm{F}}$), giving more freedom to probe wide region of the excitation spectrum. Finally, as shown in this work, the center-of-mass displacement of the cloud along the direction of the Bragg beams can be easily used to probe the pair correlations, compared to tedious numerical analysis of the atom-shot noise from the absorption images.

The experimentally measurable quantity that is related to the pair correlation function, via a Fourier transform, is the dynamic structure factor (DSF). In an inelastic scattering experiment, when the probe particle is weakly coupled to the many-body system, the DSF provides information about the spectrum of collective excitations at low momentum transfers [53, 54, 55]. At high momentum transfer, the DSF gives details about the momentum distribution of the system, where the response is dominated by single-particle effects. The DSF, for example, in superfluid liquid

He is measured through the differential scattering cross-section in neutron scattering experiments [56, 57, 58, 59]. Fortunately, in atom optics, Bragg spectroscopy has proven to be an equivalent technique to probe the dynamic [60] and static structure factors [61] in atomic BECs. The static structure factor (SSF) is the effective line strength of scattering at a particular momentum.

The main objective of this work is to implement Bragg spectroscopy to probe pair correlations across the BEC-BCS crossover in terms of the interaction strength. To probe the single-particle behaviour, the momentum imparted to the system is kept maximum with respect to the Fermi wave vector k_{F}. Since this is a mass-dependent scattering process, it can also be used to probe the relative fraction of the constituent particles in a strongly interacting Fermi gas at unitarity. In fact, on the BCS side, Bragg spectroscopy has been theoretically proposed to detect Cooper pairs in a weakly interacting Fermi gas [62]. In addition to this, on the BEC side, the effects of mean-field interactions on the momentum distribution of a molecular BEC can be probed using Bragg spectroscopy. The first Bragg scattering experiment performed on ultracold sodium dimers [63] has shown a surprisingly large shift in the Bragg resonant frequency, which could not be explained using only mean-field interactions. Further study is anticipated in this direction.

1.3 Thesis outline

With the possibility of probing various dynamic properties of an interacting Fermi gas using Bragg spectroscopy, this work started with setting up the experimental apparatus in several stages, in collaboration with two other postgraduate students. At first, a molecular BEC was created in a low power optical dipole trap, followed by the production of a degenerate Fermi gas [64]. After this achievement, the experiment was upgraded by including a tapered amplifier to create a six-beam magneto-optical trap (MOT) and by setting up a high-power single optical dipole trap using a 100 W fibre

laser. In order to study the strongly interacting properties of the fermions, all the images presented in this thesis were obtained at high magnetic fields. This is achieved by implementing a laser offset-locking technique [65], allowing one to take absorption images at high magnetic fields.

The thesis is structured in the following way : Chapter-2 starts by highlighting the effect of external harmonic confinement on non-interacting and interacting quantum degenerate gases. In Chapter-3, the basic theory required to understand the BEC-BCS crossover physics is described. The idea is to discuss briefly collisions at ultracold temperatures, Feshbach resonances and the atomic structure of ^{6}Li. Chapter-4 describes the experimental set-up involved in performing the experiments. The technical details of the apparatus are described, including the vacuum system, the optical setup, the lasers and absorption imaging. The laser locking schemes and the optical setups discussed here differ from those mentioned in reference [66], the first Ph.D thesis from this group. In Chapter- 5, the results obtained from this new set-up are presented. The experimental details about the production and observation of a molecular BEC and a degenerate Fermi gas are also given.

Chapter-6 outlines the importance of inelastic scattering experiments to probe the internal properties of the many-body system. The principles of Bragg scattering are explained. An expression to relate the density correlation functions to the measured Bragg signal (centre-of-mass displacement of the cloud) is derived. Following this, a new way to analyze the Bragg signal is described in Chapter-7. This chapter also includes the results obtained from Bragg scattering in the collionless regime (without interactions). In this regime, the single-particle properties of atoms and molecules are verified by observing two-photon Rabi oscillations. Chapter-8 presents the key results of the thesis obtained through Bragg scattering in the strongly interacting regime. In this regime, the static structure factor which is related to the pair correlation function is evaluated from Bragg spectra for the first time. It is found to vary smoothly from the BEC side to BCS side in qualitative agreement with the theoretical prediction [51]. In

addition, the measured density dependence of correlated pairs is presented. At the end of this chapter, thermometry of a strongly interacting Fermi gas is briefly discussed. Chapter-9 summarizes the main results from the thesis and also gives an outlook for future experiments that can be performed with the same experimental set-up.

Chapter 2

Trapped quantum degenerate gases

2.1 Introduction

In this chapter, the behaviour of degenerate quantum gases at ultracold temperatures is first discussed briefly. This is followed by a discussion on the properties of trapped degenerate gases. Since the particles are trapped in an optical dipole trap, which can be approximated by a harmonic potential near the bottom of the trap, the properties of the gas are discussed only in such a potential for both non-interacting (sec. 2.3) and interacting (sec. 2.4) gases. A number of textbooks [67, 68] and review articles [30] can provide a detailed discussion on this topic, and hence only the important results are presented here. Physically measurable quantities such as particle number, temperature and density distribution are described in each case. The last section explains the scaling factors required for application to the width of an hydrodynamically expanding cloud.

2.2 Quantum statistics

All fundamental particles are classified either as bosons or fermions owing to their intrinsic angular momentum called spin. Bosons have integral spin quantum number whereas fermions have half-integral spin quantum number. When these particles combine to form a complex structure (like an atom or a molecule), the total spin quantum number can be either an integer, making it a composite boson, or an odd half-integer, making it a composite fermion. The basic difference between bosons and fermions arises as a consequence of the Pauli principle which states that the total wavefunction for a system must be symmetric (anti-symmetric) with respect to exchange of any pair of bosons (fermions). As a result, the Pauli principle forbids two identical fermions from occupying the same quantum state. This quantum behaviour of the particles comes into play only at ultracold temperatures (< 1 mK), when their de Broglie wavelength $\lambda_{\rm dB} = \sqrt{\frac{2\pi\hbar^2}{m\ k_{\rm B}T}}$ becomes comparable to the spacing between the particles, where m is the mass of the particle at temperature T. This is depicted for particles in a harmonic trap in Fig. 2.1 where the phase-space density $D = n\lambda_{\rm dB}^3$ at a particle density n is used to differentiate various temperatures.

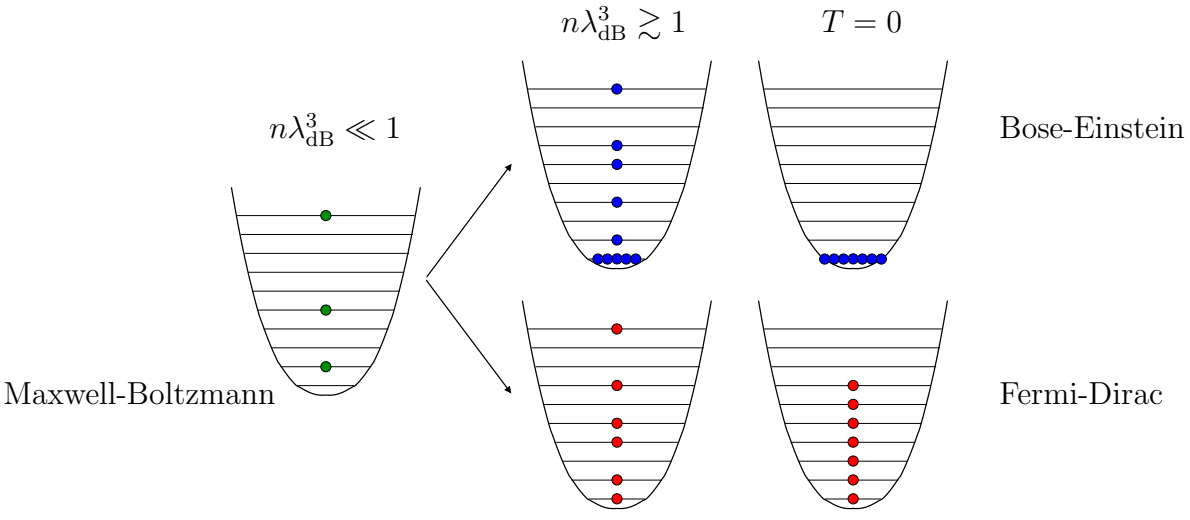

Figure 2.1: Comparison of identical bosons (in blue) and fermions (in red), respectively, at different temperatures. The phase-space density is written as $D = n\lambda_{\rm dB}^3$.

At sufficiently high temperatures, the mean occupation number for all the energy

states is much less than one ($n\lambda_{\mathrm{dB}}^3 \ll 1$) and the particles' behaviour is well described by Maxwell-Boltzmann statistics ($p = 0$ in eq. 2.2). As the temperature is lowered to the point of degeneracy ($n\lambda_{\mathrm{dB}}^3 \gtrsim 1$) quantum statistics becomes crucial. A gas of identical bosons (in blue) begins to occupy the ground state macroscopically according to Bose-Einstein statistics ($p = -1$ in eq. 2.2), whereas fermions (in red) fill up the low-lying energy states following the Pauli principle, with at most one identical atom per state according to Fermi-Dirac statistics ($p = +1$ in eq. 2.2). At $T = 0$ all the bosons are condensed in the ground state while the fermions fill up all the states up to the Fermi energy $E_{\mathrm{F}} = k_{\mathrm{B}}T_{\mathrm{F}}$, where T_{F} is the Fermi temperature.

In our experiments, we use two spin states of fermionic ^{6}Li atoms that can be combined using a Feshbach resonance to make a diatomic bosonic molecule. Because these molecules follow Bose-Einstein statistics, they can be cooled to form a molecular BEC.

2.2.1 Distribution functions

As mentioned above, quantum statistics start to play a crucial role once the gas is cooled below a certain critical temperature T_{c}. To obtain an expression for T_{c}, first consider a gas with N particles trapped in a harmonic potential:

$$V(\mathbf{r}) = \frac{1}{2}m\omega_x^2 x^2 + \frac{1}{2}m\omega_y^2 y^2 + \frac{1}{2}m\omega_z^2 z^2 \tag{2.1}$$

where ω_x, ω_y and ω_z are the trapping frequencies in each direction. Then the mean occupation number $f(\varepsilon_i)$ of a single-particle i^{th} state with energy ε_i is given by

$$f(\varepsilon_i) = \frac{1}{e^{\frac{(\varepsilon_i - \mu)}{k_B T}} + p} \tag{2.2}$$

where the chemical potential μ is obtained from the normalization condition

$$\sum_i f(\varepsilon_i) = N, \tag{2.3}$$

and $p = \pm 1$ for quantum gases or 0 for a classical gas. When the temperature is sufficiently large, the term with p becomes negligible and the gas is described by classical Maxwell-Boltzmann statistics with $p = 0$. Below critical temperatures, the gas is described by Bose-Einstein statistics for bosons (integer spin) with $p = -1$ and by Fermi-Dirac statistics for fermions (odd half-integer spin) with $p = +1$.

The summation in eq. 2.3 can be approximated by an integration when the system occupies many levels to give an almost continuous distribution ($k_{\mathrm{B}}T \gg \hbar\omega_i$). Using the density of states in a harmonic trap

$$g(\varepsilon) = \frac{\varepsilon^2}{2(\hbar\overline{\omega})^3}, \tag{2.4}$$

where $\overline{\omega} = (\omega_x\omega_y\omega_z)^{1/3}$ is the geometric mean of the three trapping frequencies, the integration becomes

$$N = \int g(\varepsilon)\, f(\varepsilon)\, \mathrm{d}\varepsilon. \tag{2.5}$$

and the total energy of the system E can be obtained from the relation

$$E = \int \varepsilon\ g(\varepsilon)\, f(\varepsilon)\, \mathrm{d}\varepsilon. \tag{2.6}$$

All of the thermodynamic quantities like specific heat, entropy etc. can be obtained once the total energy of the system is known.

2.3 Trapped non-interacting degenerate gases

Before discussing interacting degenerate gases, it is worthwhile to summarise the properties of trapped non-interacting degenerate gases.

2.3.1 Bosons

The Hamiltonian H for an ideal (non-interacting) Bose gas trapped in a harmonic potential is

$$H = -\frac{\hbar}{2m}\nabla^2 + V(\mathbf{r}). \tag{2.7}$$

The wavefunction for a BEC is then given by the solution of the Schrödinger equation for the above Hamiltonian. This has the same wavefunction as that of a single particle in the ground state, except for the normalization constant

$$\phi_0(\mathbf{r}) = \sqrt{N}\left(\frac{1}{\sqrt{\pi}a_{ho}}\right)^{3/2} \exp\left(-\frac{\mathbf{r}^2}{2a_{ho}^2}\right), \tag{2.8}$$

where $a_{ho} = \sqrt{\hbar/m\bar{\omega}}$ is the harmonic oscillator length, which gives the size of the cloud. The density distribution of the condensed cloud then becomes $n_0(\mathbf{r}) = |\phi_0(\mathbf{r})|^2$ which increases linearly with N, the total number of particles. Writing N as the sum of condensed atoms N_0 and thermal atoms N_{T}, the critical temperature T_{c} and the condensate fraction N_0/N are evaluated using eq. 2.5 to be [68]

$$T_{\mathrm{c}} = 0.94\frac{\hbar\bar{\omega}N^{1/3}}{k_{\mathrm{B}}}, \tag{2.9}$$

$$\frac{N_0}{N} = 1 - \left(\frac{T}{T_{\mathrm{c}}}\right)^3. \tag{2.10}$$

This relation gives a large condensate fraction of 90% even at a temperature $T/T_{\mathrm{c}} = 0.5$. The density distribution for the thermal cloud $n_{\mathrm{T}}(\mathbf{r})$ is given by

$$n_{\mathrm{T}}(\mathbf{r}) = \frac{1}{\lambda_{\mathrm{dB}}} Li_{3/2}\, \exp\left(-\frac{V(\mathbf{r})}{k_{\mathrm{B}}T}\right) \tag{2.11}$$

where Li represents the poly-logarithmic function. Since the width $R_{\mathrm{T}} = a_{ho}(k_{\mathrm{B}}T/\hbar\bar{\omega})$ associated with this thermal distribution is typically much larger than a_{ho}, a BEC in a harmonic trap is revealed by the appearance of a sharp peak in the central region of

the density distribution. The mean energy per particle is obtained from eq. 2.6 [69]

$$\frac{E}{N} = 2.7 k_{\mathrm{B}} T_{\mathrm{c}} \left(\frac{T}{T_{\mathrm{c}}} \right)^4 . \tag{2.12}$$

2.3.2 Fermions

Consider a sample of N spin polarized fermions trapped in a harmonic potential. For such a system, the chemical potential at $T = 0$ defines the energy of the highest occupied state, also called the Fermi energy E_{F}. It is obtained by integrating eq. 2.5 at $T = 0$

$$E_{\mathrm{F}} = \hbar\overline{\omega}(6N)^{1/3} = k_{\mathrm{B}} T_{\mathrm{F}} \tag{2.13}$$

The Fermi temperature T_{F} marks the crossover to a degenerate Fermi gas (similar to T_{c} for a BEC) where the mean occupation number approaches unity. Note that both temperatures, T_{c} and T_{F}, have the same $N^{1/3}$ dependence on the number of trapped atoms.

The zero temperature density distribution at a position $\mathbf{r}$ can be obtained by first evaluating the number of atoms that fit into a momentum sphere with radius $\hbar k_{\mathrm{F}}(\mathbf{r})$ as

$$n(\mathbf{r}) = \frac{1}{(2\pi\hbar)^3} \frac{4}{3} \pi (\hbar k_{\mathrm{F}}(\mathbf{r}))^3, \tag{2.14}$$

where $1/(2\pi\hbar)^3$ is the density of states. In the Thomas-Fermi approximation, where the trapped gas can be described by a uniform gas, a local Fermi wave vector $k_{\mathrm{F}}(\mathbf{r})$ is defined for each point in space by

$$E_{\mathrm{F}} = \frac{\hbar^2 k_{\mathrm{F}}^2(\mathbf{r})}{2m} + V(\mathbf{r}). \tag{2.15}$$

Combining equations 2.14 and 2.15, the spatial profile of a non-interacting Fermi gas is obtained as

$$n(\mathbf{r}, T = 0) = \frac{1}{6\pi^2} \Big[\frac{2m}{\hbar^2} \big(E_{\mathrm{F}} - V(\mathbf{r}) \big) \Big]^{3/2}. \tag{2.16}$$

which vanishes for $V(\mathbf{r}) > E_{\mathrm{F}}$. Defining the Thomas-Fermi radius R_{F}^{i} as the width at which the density goes to zero in direction $i = x, y, z$, by setting $V(R_{\mathrm{F}}^{i}) = E_{\mathrm{F}}$, the maximum extent of the fermionic cloud is obtained as

$$R_{\mathrm{F}}^{i} = \sqrt{\frac{2k_{\mathrm{B}}T_{\mathrm{F}}}{m\omega_i^2}} \qquad \text{or} \qquad R_{\mathrm{F}}^{i} = \sqrt{\frac{\hbar}{m\overline{\omega}}}\big(48N\big)^{1/6}\frac{\overline{\omega}}{\omega_i}. \tag{2.17}$$

The distribution function then becomes [30]

$$n(\mathbf{r}, T=0) = \frac{8N}{\pi^2 R_{\mathrm{F}}^{x} R_{\mathrm{F}}^{y} R_{\mathrm{F}}^{z}}\Big[1 - \Big(\frac{x}{R_{\mathrm{F}}^{x}}\Big)^2 - \Big(\frac{y}{R_{\mathrm{F}}^{y}}\Big)^2 - \Big(\frac{z}{R_{\mathrm{F}}^{z}}\Big)^2\Big]^{3/2}. \tag{2.18}$$

The mean energy per particle is obtained from eq. 2.6 as [70]

$$\frac{E}{N} = \frac{3}{4}k_{\mathrm{B}}T_{\mathrm{F}}. \tag{2.19}$$

2.4 Trapped interacting degenerate gases

Interactions play a very important role in determining the dynamical behaviour of the gas. They also contribute to modifying the density distributions of the clouds. In the following sections, the main focus is on understanding the effects of interactions on the shape of the clouds.

2.4.1 Bosons

Consider a gas with N interacting bosons trapped in a harmonic potential $V(\mathbf{r})$ at temperature $T = 0$. In a dilute gas, the interactions are dominated by low energy two-body s-wave collisions (see chapter. 3). The interactions can then be treated as a mean-field contact potential whose strength is characterized by the coupling constant $g = 4\pi\hbar^2 a/m$, where a is the s-wave scattering length. This approximation allows us to write the many-body Schrödinger equation for N bosons in terms of a single

macroscopic order parameter $\Psi(\mathbf{r})$ (the condensate wavefunction) [68]. In equilibrium, the density distribution is obtained from the time-independent Gross-Pitaevskii (GP) equation

$$\Big(-\frac{\hbar^2}{2m}\nabla^2 + V(\mathbf{r}) + g\,|\Psi(\mathbf{r})|^2 \Big)\Psi(\mathbf{r}) = \mu\Psi(\mathbf{r}), \tag{2.20}$$

where μ is the chemical potential which characterises the ground state energy of the condensate. From the solution of this equation, the density distribution can be calculated from $n(\mathbf{r}) = |\Psi(\mathbf{r})|^2$.

When the number of atoms is large and the interactions are repulsive, the ratio of kinetic to potential (interaction) energy can become small. In this regime, the first (kinetic) term in the GP equation can be neglected. This assumption is often referred to as the Thomas-Fermi approximation. Then the density distribution is given analytically by

$$n(\mathbf{r}) = \frac{1}{g}(\mu - V(\mathbf{r})). \tag{2.21}$$

The chemical potential μ is determined by the normalising condition $\int \mathrm{d}\mathbf{r}\, n(\mathbf{r}) = N$ and the shape of the density distribution becomes an inverted parabola in 3D [30]

$$n(\mathbf{r}, T=0) = \frac{15N}{8R^xR^yR^z}\Big[1 - \Big(\frac{x}{R^x}\Big)^2 - \Big(\frac{y}{R^y}\Big)^2 - \Big(\frac{z}{R^z}\Big)^2\Big], \tag{2.22}$$

where the Thomas-Fermi radius R^i is defined by the width at which the density goes to zero

$$R^i = \sqrt{\frac{2\mu}{m\omega_i^2}} = a_{ho}\frac{\bar{\omega}}{\omega_i}\left(\frac{15Na}{a_{ho}}\right)^{1/5}. \tag{2.23}$$

The mean energy per particle is obtained from eq. 2.6

$$\frac{E}{N} = \frac{5}{7}\mu. \tag{2.24}$$

At finite temperature T, because the density of the thermal cloud is much lower than that of the condensed component, the coupling between them can be ignored. Therefore, the density distribution is given by eq. 2.22 with N replaced by N_0. To a

first-order correction, the condensate fraction is the same as that of an ideal gas, while the critical temperature is reduced according to the relation [71]

$$\frac{T_{\rm c} - T_{\rm c}^0}{T_{\rm c}^0} = -1.32 N^{1/6} \frac{a}{a_{ho}}, \tag{2.25}$$

where $T_{\rm c}^0$ is the critical temperature of a non-interacting gas.

2.4.2 Fermions

In the case of ultracold spin polarized fermions, interactions are suppressed due to the Pauli exclusion principle. However, if atoms in two different spins are considered then they can interact via s-wave collisions at ultracold temperatures. These interactions give rise to pairing effects which can lead to superfluid properties. Consider a two-component Fermi gas with equal numbers of atoms $N/2$ in each state, spin up ($\sigma = \uparrow$) and spin down ($\sigma = \downarrow$). Because the interaction strength varies across the cloud, as the density varies, there exists no exact analytic solution for the many-body problem of trapped fermions across the BEC-BCS crossover. The results given below use the local density approximation, which assumes that locally the system can be treated like a uniform gas. Also, the results given below are strictly for a *trapped* interacting two-component Fermi gas at temperature $T = 0$. For the case of an interacting *uniform* Fermi gas, the reader is referred to the review article [70]. In general, the interaction strength across the BEC-BCS crossover can be quantified by a dimensionless parameter $1/(k_{\rm F}a)$ which is the ratio of the interparticle spacing to the scattering length.

Weak repulsive interactions :

In the limit of weak repulsive interactions, the scattering length is small and positive $a > 0$ and $1/(k_{\rm F}a) \to +\infty$. For very small positive values of a, a repulsive interacting Fermi gas is formed [30]. However, in the presence of a Feshbach resonance, a positive scattering length is linked to the presence of a molecular bound state in the interparticle potential. Since these molecules are composite bosons formed by two fermions, their

behaviour can be described by standard BEC theory. This limit of the Feshbach resonance is frequently referred to as the BEC-side or BEC-limit.

For a weakly interacting gas, the Thomas-Fermi limit, which requires the interaction energy to dominate over the kinetic energy, can be easily satisfied. This gives the following parabolic density profile

$$n(\mathbf{r}, T=0) = \frac{15N}{16R^xR^yR^z}\Big[1 - \Big(\frac{x}{R^x}\Big)^2 - \Big(\frac{y}{R^y}\Big)^2 - \Big(\frac{z}{R^z}\Big)^2\Big] \tag{2.26}$$

$$R^i = \sqrt{\frac{2\mu_M}{M\omega_i^2}} = a_{ho}\frac{\bar{\omega}}{\omega_i}\left(\frac{15N_M a_M}{a_{ho}}\right)^{1/5} \tag{2.27}$$

where $N_M = N/2$ is the number of molecules with mass $M = 2m$ and $a_M = 0.6a$ is the molecular scattering length [39]. The interaction between the molecules is characterized by the mean-field equation of state

$$\mu(n) = \frac{\pi\hbar^2 a_M n}{m} \tag{2.28}$$

which depends linearly on the density n of the system.

Weak attractive interactions :

In the limit of weak attractive interactions, the scattering length is small and negative $a < 0$ and $1/(k_{\mathrm{F}}a) \to -\infty$. This limit of the Feshbach resonance is frequently referred to as the BCS-side or BCS-limit. For this case ($k_{\mathrm{F}}|a| \ll 1$), the many-body problem can be solved both at $T = 0$ and at finite temperature using BCS theory, which describes superconductivity in metals [38]. The interactions are added as a perturbation to the non-interacting Fermi gas to obtain a first-order correction to the Thomas-Fermi radius

$$R^i = \sqrt{\frac{2\mu_0}{m\omega_i^2}} = R^i_{\mathrm{F}}\big(1 - \frac{256}{315\pi^2}k_{\mathrm{F}}|a|\big) \tag{2.29}$$

where k_{F} is the Fermi wave vector of a non-interacting gas. This result shows that the

width of the cloud is compressed due to attractive interactions. If $k_{\rm F}|a| \ll 1$, then the Thomas-Fermi radius becomes equal to that of a non-interacting gas

$$R_{\rm F}^{i} = \sqrt{\frac{2k_{\rm B}T_{\rm F}}{m\omega_i^2}}, \tag{2.30}$$

and the density distribution is given by

$$n(\mathbf{r}, T=0) = \frac{4N}{\pi^2 R_{\rm F}^x R_{\rm F}^y R_{\rm F}^z}\Big[1 - \Big(\frac{x}{R_{\rm F}^x}\Big)^2 - \Big(\frac{y}{R_{\rm F}^y}\Big)^2 - \Big(\frac{z}{R_{\rm F}^z}\Big)^2\Big]^{3/2}. \tag{2.31}$$

The equation of state is approximated by that of an ideal Fermi gas, that is

$$\mu(n) = \frac{\hbar^2}{2m}(3\pi n)^{2/3}. \tag{2.32}$$

Strong interactions :

In this limit, the scattering length diverges $a \to \pm\infty$ and $1/(k_{\rm F}a) \to 0$, leaving the interparticle distance $1/k_{\rm F}$ as the only relevant length scale. This limit of the Feshbach resonance is frequently referred to as the unitarity limit. At present an exact solution of the many-body problem is not available for $k_{\rm F}|a| \gg 1$. As the scattering length exceeds the inter-particle separation, the properties of the gas become universal [36] and all the thermodynamic quantities can be written as a function of the Fermi energy $E_{\rm F}$ and the inter-particle spacing characterized by a universal constant β. In this regime, the density profile becomes [30]

$$n(\mathbf{r}, T=0) = \frac{4N}{\pi^2 R_{\rm U}^x R_{\rm U}^y R_{\rm U}^z}\Big[1 - \Big(\frac{x}{R_{\rm U}^x}\Big)^2 - \Big(\frac{y}{R_{\rm U}^y}\Big)^2 - \Big(\frac{z}{R_{\rm U}^z}\Big)^2\Big]^{3/2}. \tag{2.33}$$

with $R_{\rm U}^i = (1+\beta)^{\frac{1}{4}} R_{\rm F}^i$. Although the universal constant β has only a very weak dependence on the radius, its value can be obtained by measuring the size of the cloud at unitarity [23, 24, 31, 72]. In this limit, the chemical potential at $T = 0$ is given by

$$\mu = (1+\beta)E_{\rm F} = (1+\beta)\frac{\hbar^2}{2m}(3\pi n)^{2/3} \tag{2.34}$$

which has the same power law as non-interacting fermions.

All the results given above are for interacting fermions at zero temperature. Including finite temperature effects across the BEC-BCS crossover for interacting trapped fermions is very difficult theoretically. However, experimentally, it is found [73, 74] that the shape of finite temperature clouds at unitarity is not different from that of a non-interacting Fermi gas. This has led to the practice of fitting density profiles of a non-interacting gas to the observed data and quoting an effective/empirical temperature $\tilde{T}$ with respect to the Fermi temperature $T_{\rm F}$ [31](see sec 8.6) .

2.5 Hydrodynamic expansion of clouds

When elastic collisions rates in a trapped gas are higher than the trapping frequencies, the gas is said to be in the hydrodynamic regime. Expansion of such a gas after switching off the trap is then simply a re-scaling of the cloud widths. Since, in our experiments, absorption imaging is performed at high magnetic fields, the cloud experiences a saddle-shaped magnetic potential due to the presence of external Feshbach fields. Such an anti-confining potential can be written as

$$V(\mathbf{r}, t > 0) = \frac{1}{2} m \left(\omega_{S_x}^2 x^2 + \omega_{S_y}^2 y^2 + \omega_{S_z}^2 z^2 \right) \tag{2.35}$$

with frequencies ω_{S_i}. If the chemical potential has the power-law dependence $\mu \propto n^\gamma$, then the scaling ansatz

$$n(\mathbf{r}, t) = \frac{1}{\mathcal{V}(t)} \; n \left(\frac{x}{b_x(t)}, \frac{y}{b_y(t)}, \frac{z}{b_z(t)}, t = 0 \right) \tag{2.36}$$

provides the exact solution, where the volume unit $\mathcal{V}(t) = b_x(t) b_y(t) b_z(t)$ [30]. The scaling parameters b_i follow the time-dependent equations

$$\ddot{b_i} = -\omega_{S_i}^2 b_i + \frac{\omega_i^2(0)}{b_i \mathcal{V}^\gamma}, \tag{2.37}$$

which can be solved numerically. Here, ω_i is the initial trapping frequency. In our experiment, $\omega_{S_{x,y}} = \omega_{x,y}$ and $\omega_{S_z} = i\sqrt{2}\,\omega_{S_x}$. As discussed in the previous section, for a Fermi gas both at unitarity and in the non-interacting limit, $\mu \propto n^{2/3}$ giving $\gamma = 2/3$.

2.6 Summary

The spin dependent behaviour of particles at ultracold temperatures is briefly discussed in this chapter. The zero temperature properties of the non-interacting and interacting trapped gases in a harmonic potential are presented. The main focus of the chapter is to introduce the various parameters required to extract useful information from the experimental results. In order to keep the contents relevant to the experiments reported in the thesis, not all the superfluid properties of the degenerate gases are discussed. In particular, the excitation spectrum across the BEC-BCS crossover and the appearance of a pairing gap on the BCS side are excluded. For more details on this topic, the reader is referred to the review paper [30]. However, single particle excitations and pair correlations probed by Bragg scattering are described separately in chapter-6.

Chapter 3

Ultracold collisions and interactions

3.1 Introduction

The collisional properties of degenerate quantum gases at ultracold temperatures are discussed briefly in this chapter. First, the scattering process at low energies is revisited highlighting the dependence of the interactions on the scattering length. This is followed by quantifying the two-body interactions in terms of the scattering length. After that, in section 3.3 the Feshbach resonance, which is an important tool in manipulating ultracold atoms, is explained. Owing to the behaviour of fermionic atoms across this resonance (sec. 3.4), either a molecular BEC or a degenerate Fermi gas can be formed. Finally, in section 3.5, the ^{6}Li energy levels are described in both the absence and presence of external magnetic fields.

3.2 Scattering at ultracold temperatures

Elastic and inelastic collisions not only play a crucial role during evaporative cooling (re-thermalization) of the gas but also control the dynamics of the gas depending on

the particles (bosons or fermions) involved. For simplicity, elastic collisions between two identical particles in their centre-of-mass frame are considered to highlight the important results. The time-independent Schrödinger equation for such a system with a spherical scattering potential $V(\mathbf{r})$ is given as

$$\Big(\frac{\hbar^2}{2m_{\mathrm{r}}}\nabla^2 + V(\mathbf{r})\Big)\Psi(\mathbf{r}) = E\Psi(\mathbf{r}), \tag{3.1}$$

where the energy of the incoming free particle with mass m is

$$E = \frac{(\hbar\mathbf{k})^2}{2m_{\mathrm{r}}}, \tag{3.2}$$

$m_{\mathrm{r}} = m/2$ is the reduced mass and $\hbar\mathbf{k}$ is the initial momentum. The wave function $\Psi_{\mathbf{k}}(\mathbf{r})$ can be described as the sum of the incoming plane wave $e^{i\mathbf{k}\cdot\mathbf{r}}$ and the scattered outgoing spherical wave $\frac{e^{ikr}}{r}$ for very large distances ($r \to \infty$), that is

$$\Psi_{\mathbf{k}}(\mathbf{r}) = e^{i\mathbf{k}\cdot\mathbf{r}} + f(k,\theta)\frac{e^{ikr}}{r} \tag{3.3}$$

where $f(k,\theta)$ is the scattering amplitude which depends on the initial momentum and the angle between the directions of the relative momentum of the particles before and after scattering. The differential cross section, which gives the cross section per unit solid angle $d\Omega$, is defined by

$$\frac{\mathrm{d}\sigma}{\mathrm{d}\Omega} = |f(k,\theta)|^2. \tag{3.4}$$

An expression for $f(k,\theta)$ can be obtained by expanding the wavefunction in terms of spherical harmonics and solving the radial equation before comparing it with eq. 3.3[1]. Finally, integrating eq. 3.4, the total cross section σ is obtained in terms of the phase shifts δ_l as

$$\sigma(k) = \frac{4\pi}{k^2}\sum_{l=0}^{\infty}(2l+1)\sin^2\delta_l(k). \tag{3.5}$$

[1]This derivation is well documented in many standard textbooks, such as [75]

For a finite-range potential which vanishes at large distances, the phase shifts vary as $\delta_l \propto k^{2l+1}$ for small values of k (low energies). Thus at ultracold temperatures, the scattering cross section is dominated only by the $l = 0$ term, the s-wave scattering. In this case, the phase shift is evaluated as $\delta_0 = -ka$ where a is the scattering length, giving

$$\sigma = \frac{4\pi}{k^2}\delta_0^2 = 4\pi a^2 \tag{3.6}$$

This is an important result, which shows that for s-wave scattering the cross section depends only on the scattering length.

Now, consider the scattering of identical particles in the same internal state (both spins up or down). Then, by the Pauli principle, the wave function must be symmetric (anti-symmetric) under exchange of the co-ordinates of the bosons (fermions). Therefore, the differential cross section is written as

$$\frac{\mathrm{d}\sigma}{\mathrm{d}\Omega} = |f(k,\theta) \pm f(k,\pi-\theta)|^2, \tag{3.7}$$

where the plus sign applies to bosons and the minus sign to fermions. In other words, the cross section calculated above in eq. 3.6 are added for bosons, giving $\sigma = 8\pi a^2$, whereas the cross section vanishes for two identical fermions. However, these symmetry arguments only apply to indistinguishable particles in the same internal quantum state, while the scattering cross section in the case of two fermions in different internal states (one spin up and the other spin down) is non-zero.

3.2.1 Mean field interaction

It is interesting to note that the low-energy scattering process does not depend on the details of the microscopic potential. Hence, for a many-particle system, an effective potential can be considered to treat the interactions. One such type of potential is a

zero-range contact potential given by

$$V_{\text{eff}}(\mathbf{r}) = g\delta(\mathbf{r})\frac{\partial}{\partial r}r, \tag{3.8}$$

where $\delta(\mathbf{r})$ is the Dirac-delta function. Substituting this in eq. 3.1, the total cross section for two identical particles is obtained as

$$\sigma = \frac{4\pi a^2}{1 + k^2a^2}, \tag{3.9}$$

giving the relation between the scattering length a and the coupling constant g as $a = \frac{gm}{4\pi\hbar^2}$. This relation is used to obtain the mean-field potential experienced by a particle in a gas of density n due to scattering from all other particles as

$$U_{\text{mf}} = gn = \frac{4\pi a\hbar^2 n}{m}, \tag{3.10}$$

where n and hence U_{mf} can be functions of $\mathbf{r}$.

The significance of eq. 3.9 can be understood by considering the two extreme interacting limits. In the weakly interacting limit ($ka \ll 1$) this equation gives $\sigma_0(k) = 4\pi a^2$, recovering the low energy limit results (eq. 3.6), whereas in the strongly interacting limit ($ka \gg 1$) the scattering cross section $\sigma_0(k) = 4\pi/k^2$ becomes independent of the scattering length giving the maximum possible cross section for s-wave collisions. This is the unitarity regime which can be realised in a Fermi gas at the BEC-BCS crossover.

3.3 Feshbach resonance

Consider a ^{6}Li atom, a fermion, with a single valence electron in its ground state (J=1/2). Together with a nuclear spin of I=1, the total angular momentum becomes F=I$\pm$J, giving F=1/2 and F=3/2. When two such atoms interact, the different

combinations of these hyperfine states give rise to three inter-atomic potential curves. In the presence of magnetic fields, they are further split into several sub-level channels depending on the projection quantum numbers m_F. For a given collision energy, a channel accessible at large interatomic distances ($R = \infty$) is described as an open channel, while energetically detuned channels are called closed channels. Figure 3.1 shows closed and open channel potential curves for two interacting atoms. A Feshbach resonance is said to occur whenever the threshold energy of the colliding atoms in an open channel becomes equal to a bound energy state in the closed channel.

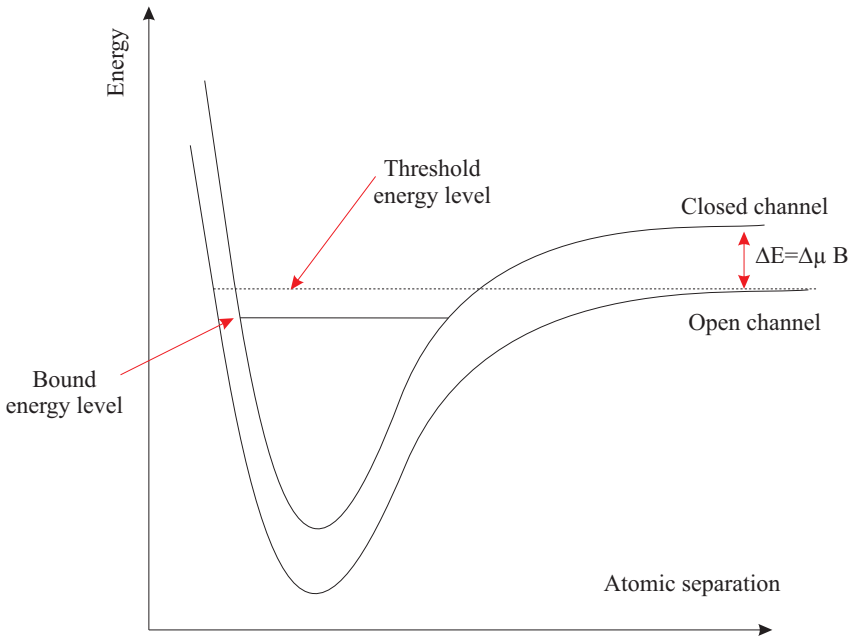

Figure 3.1: Feshbach resonance. Closed and open channel potential curves are shown for two interacting atoms.

Experimentally, the energy difference ΔE between the bound state and the threshold energy level can be tuned by means of a magnetic or electric field, provided the two channels have different magnetic/electric dipole moments. In our experiment, a magnetic field generated by a pair of Helmholtz coils is used to precisely control the scattering length across the Feshbach resonance according to the relation

$$a = a_{bg}\left(1 + \frac{\Delta B}{B - B_0}\right) \tag{3.11}$$

where a_{bg} is the background scattering length of the open channel, B is the strength of the applied external magnetic field, B_0 is the magnetic field at resonance, and ΔB is the width of the resonance which depends on the magnetic moments of the closed and open channels. The Feshbach resonance for the two lowest energy states of ^{6}Li at 834G is plotted in Fig. 3.2.

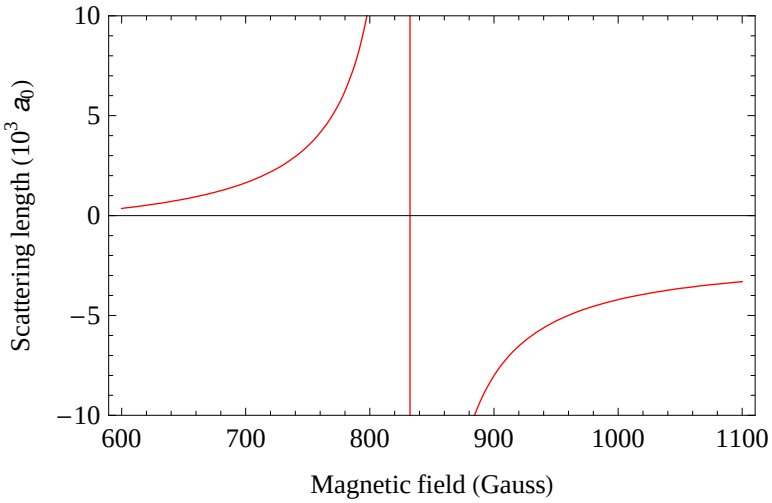

Figure 3.2: Calculated scattering length across the BEC-BCS crossover [76]. Only the broad Feshbach resonance at 834 G (vertical line) is shown.

3.4 The BEC-BCS crossover

3.4.1 BEC side

On the lower-field side of the Feshbach resonance, the scattering length is positive creating a repulsive interaction between fermions in two different spin states. This corresponds to the energy of a weakly bound molecular state, available in the closed channel, lying just below the open channel continuum, and using the Feshbach resonance coupling to this bound state is achieved. The molecules are formed through three-body recombination during the evaporative cooling stage. Although three-body

collisions are expected to be suppressed, even in a two-component Fermi gas, it has been shown theoretically [77] that they can occur near a Feshbach resonance. During evaporation, if the atomic temperature (kinetic energy) decreases below the molecular binding energy $E_{\rm b}$, efficient production of molecules is favoured. These molecules are formed in the highest ro-vibrational states. Due to inelastic collisions among themselves or with atoms, they can relax into a deeper bound state. The size of these molecules is of the order of a and their binding energy is given by $E_{\rm b} \simeq -\hbar^2/ma^2$ [70].

Such bosonic molecules composed of fermionic atoms are found to be much more stable than those composed of two bosonic atoms [4]. This is because inelastic collision rates are suppressed in the first case, due to the Pauli principle. During atom-molecule collisions, since one atom in the molecule will have the same spin as that of the colliding atom, Pauli blocking prevents the atom from colliding with the molecule. This process is also same for molecule-molecule collisions as the size of the molecules is large. Since the scattering lengths of molecule-molecule $a_{\rm M}$ and atom-molecule $a_{\rm am}$ collisions are described in terms of the atomic scattering length a as [39, 78],

$$a_{\rm M} = 0.6a \qquad \text{and} \qquad a_{\rm am} = 1.2a, \tag{3.12}$$

the inelastic collision rate is characterized in terms of the loss coefficient α evaluated [2, 24] for both the cases as

$$\alpha_{\rm M} \propto a^{-2.55} \qquad \text{and} \qquad \alpha_{\rm am} \propto a^{-3.33}. \tag{3.13}$$

These results show that as the scattering length increases, the inelastic collision rates decrease leading to a stable molecular system near the Feshbach resonance. Also, it has been shown theoretically [39] that the inelastic collision rate is significantly smaller than the elastic scattering rate, allowing efficient evaporative cooling of molecules to form a molecular BEC.

3.4.2 BCS side

On the higher-field side of the Feshbach resonance the scattering length is negative creating an attractive interaction between fermions in two different spin states. Even for small attractive interactions, the formation of correlated Cooper pairs is energetically favourable. These pairs are much larger than the inter-particle distance, with constituent atoms correlated in momentum space rather than in real space. Unlike the molecules formed on the BEC side, the pairing gap is smaller than the Fermi energy. One of the long standing goals in ultracold Fermi gas experiments is to observe these Cooper pairs explicitly. In this regard, Bragg scattering of Cooper pairs has been theoretically proposed [62]: the theory predicts the scattering of these pairs spatially half-way between the parent and the scattered atomic cloud, forming a ring structure in momentum space.

3.4.3 Unitarity

Exactly at the Feshbach resonance, the scattering length diverges, and the inter-particle separation becomes the only relevant length scale. In this regime, the size of the pairs becomes comparable to the inter-particle distance. Under such conditions, the properties of the gas become universal [36]. Note that although no bound molecular state exists in this regime, correlated pairs are formed due to strong interactions. Also, the crossover from the BEC side to the BCS side is found to be continuous and reversible experimentally [23].

3.5 Energy levels of ^{6}Li atom

Natural lithium consists of two isotopes, ^{6}Li and ^{7}Li. ^{6}Li has a nuclear spin quantum number of I=1 whereas ^{7}Li has I=1/2. The ground state electronic configuration of

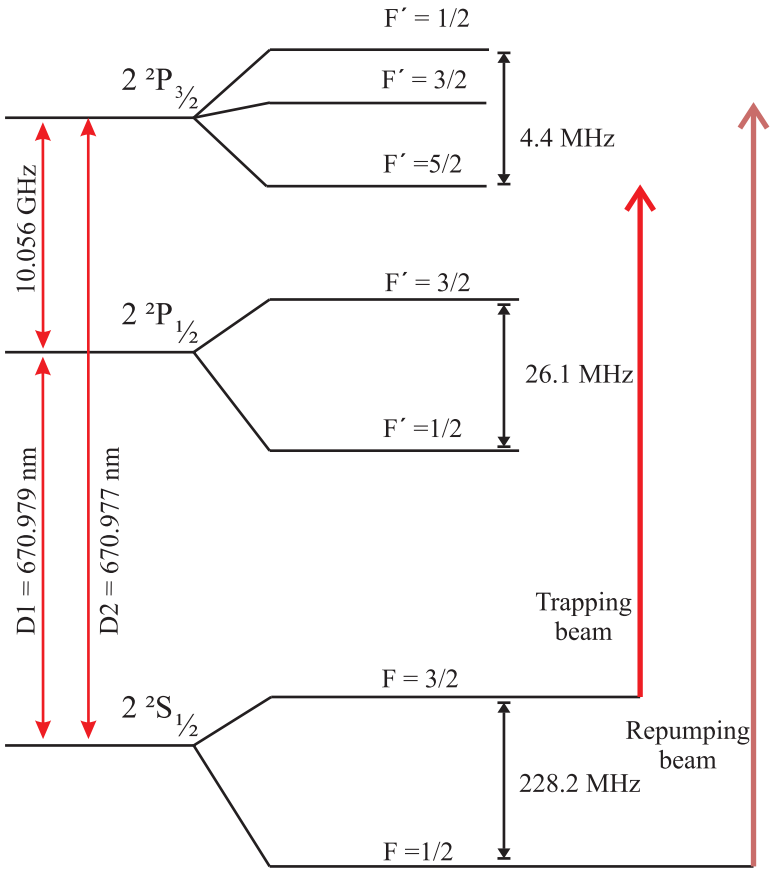

Figure 3.3: Energy level diagram for ^{6}Li (not to scale). Also shown are the trapping and repumping transitions used for the experiment.

^{6}Li is: $1s^2; 2s^1$. Therefore, the total spin of ^{6}Li is 3/2 (I=1 and J=1/2) making it a fermion. With a single $2s^1$ electron outside the closed shell its first excited state is a $2p^1$ electron. Due to spin-orbit coupling, this excited state splits into $2^2P_{1/2}$ and $2^2P_{3/2}$ states. The separation of the $2^2S_{1/2}$ and the $2^2P_{3/2}$ states is 670.977 nm (D2 line), and the separation of the $2^2S_{1/2}$ and $2^2P_{1/2}$ states is 670.979 nm (D1 line). These three states further show hyperfine splitting due to magnetic dipole and electron quadrupole interactions. The ground state $2^2S_{1/2}$ splits into two, F=1/2 and F=3/2, with a separation of 228.2 MHz. Similarly, the excited state $2^2P_{1/2}$ splits into two, F′=1/2 and F′=3/2, with a separation of 26.1 MHz. The $2^2P_{3/2}$ excited state splits into three with a total separation of 4.4 MHz. Although these states are shown schematically in Fig. 3.3, they are not resolved experimentally as their separation is less than the natural

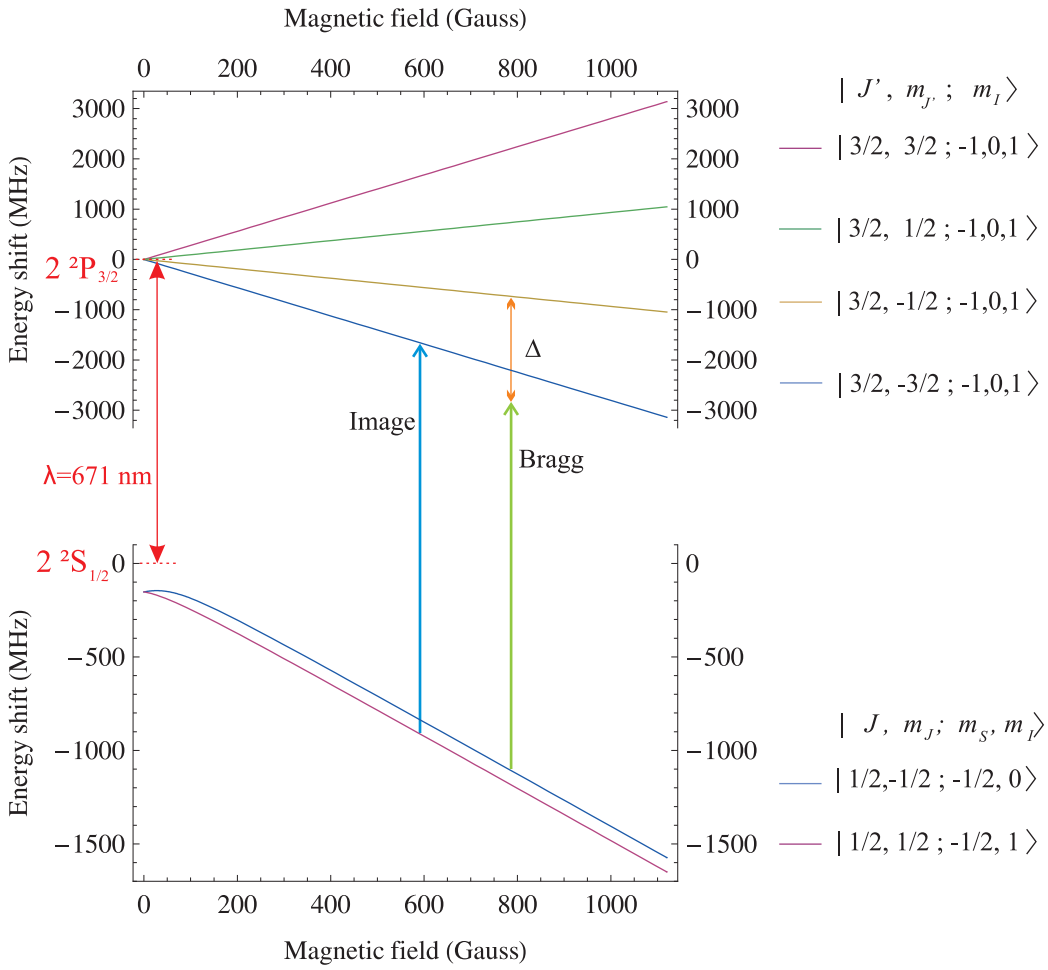

Figure 3.4: Calculated hyperfine energy shifts for the $2^2S_{1/2}$ and $2^2P_{3/2}$ states in the presence of an external magnetic field. Only the F=1/2 state energy shifts are shown for the ground state $2^2S_{1/2}$. This is obtained from the Breit-Rabi formula whereas the energy shifts for $2^2P_{3/2}$ state are obtained in the Paschen-Bach limit. Δ is the detuning of the Bragg beam from $|J' = 3/2, m_{J'} = -1/2; m_I = -1, 0, 1\rangle$ state.

linewidth ($\Gamma/2\pi$=5.9 MHz) of the atomic transitions. For the same reason, sub-Doppler polarization gradient cooling [79] is not possible with ^{6}Li atoms and the temperature of a MOT is limited to Doppler cooling. Figure 3.3 also shows the transitions used for the trapping and repumping beams in the D2 line. For efficient cooling, the intensity of both the trapping and repumping beams should be close to equal.

All the energy levels discussed above are for an atom in the absence of external

fields. Figure 3.4 shows the numerically calculated[2] energy shifts for $2^2S_{1/2}$ and $2^2P_{3/2}$ states in the presence of a magnetic field. Energy splitting of $2^2S_{1/2}$ is plotted just for F=1/2 state as all our experiments are performed using the two Zeeman sub-levels from this state. These states $|J = 1/2, m_J = 1/2; m_S = -1/2, m_I = 1\rangle$ and $|J = 1/2, m_J = -1/2; m_S = -1/2, m_I = 0\rangle$ will hereafter be referred to as state $|1\rangle$ and $|2\rangle$ respectively, representing spin up and spin down states. Owing to the small hyperfine splitting, the $2^2P_{3/2}$ the atom enters the Paschen-Bach regime at relatively low magnetic fields, whereas the $2^2S_{1/2}$ energy levels follow the anomalous Zeeman effect (Briet-Rabi formula). Also shown in the figure are the transitions used for high field imaging ($|1\rangle \rightarrow |J' = 3/2, m_{J'} = -3/2; m_I = -1, 0, 1\rangle$) and Bragg scattering ($|2\rangle \rightarrow |J' = 3/2, m_{J'} = -1/2; m_I = -1, 0, 1\rangle$).

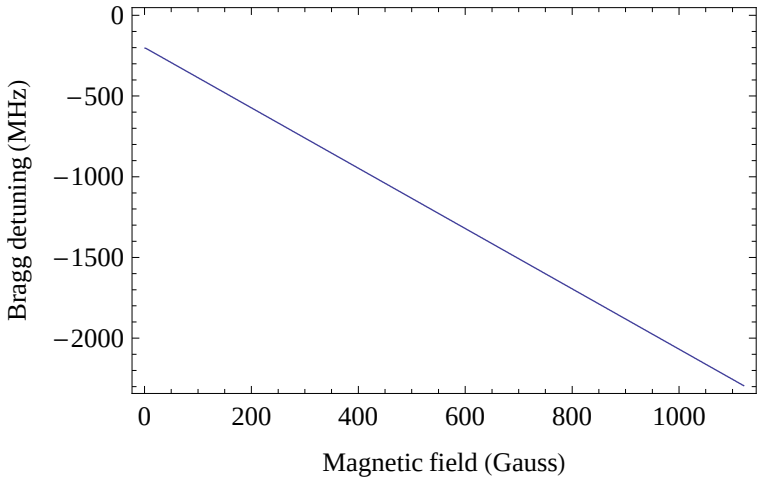

Figure 3.5: Frequency detuning of the Bragg beams from $|2\rangle \rightarrow |J' = 3/2, m_{J'} = -1/2; m_I = -1, 0, 1\rangle$.

The transition used in our Bragg scattering experiments is selected by setting the Bragg laser polarization parallel to the external Feshbach magnetic fields. Note that, in our experiments, the Bragg frequency is always red shifted by 280 MHz with respect to the imaging beam (see sec. 4.4). However, since the Bragg transition is from the state $|2\rangle$, which is 80 MHz blue detuned from the state $|1\rangle$, the difference becomes only

[2]Mathematica code published in reference [80] is used

200 MHz. The Bragg detuning is then calculated as the frequency difference between the $|J' = 3/2, m_{J'} = -3/2; m_I = -1, 0, 1\rangle$ and $|J' = 3/2, m_{J'} = -1/2; m_I = -1, 0, 1\rangle$ excited states plus 200 MHz. This final Bragg detuning is plotted in Fig. 3.5 in terms of the external magnetic field. The Bragg beams are red-detuned from the $|J' = 3/2, m_{J'} = -1/2; m_I = -1, 0, 1\rangle$ state by a range $\Delta/2\pi$ =1.5 GHz to 2.0 GHz across the BEC-BCS crossover. Though these beams seem to be very closely (200 MHz) red-detuned from the $|J' = 3/2, m_{J'} = -3/2; m_I = -1, 0, 1\rangle$ state and very largely (2Δ) red-detuned from the $|J' = 3/2, m_{J'} = 1/2; m_I = -1, 0, 1\rangle$, they do not address these states. This is because only a π- polarized light can excite this transition, whereas the Bragg beams are linearly polarized in our experiment (see sec. 4.7).

3.6 Summary

In this chapter, ultracold collisions and interactions in quantum degenerate gases are revised. More importantly the way the interactions are controlled in experiments using a Feshbach resonance is explained. The focus is given mainly to s-wave scattering, although the binding energies of ^{6}Li p-wave Feshbach molecules have been measured [81] in our lab. The broad s-wave Feshbach resonance in ^{6}Li is well suited to study the BEC-BCS crossover physics. The energy levels of ^{6}Li are described showing the relevant transitions used for laser cooling and trapping experiments. Also from the transitions chosen for absorption imaging, it is clear that only atoms in the state $|1\rangle$ are imaged.

Chapter 4

Experimental set-up

4.1 Overview

The key experimental result of this thesis is the probing of strongly interacting degenerate gases using Bragg spectroscopy. The whole experimental set-up required to perform this task is quite complex and a major part of it has been described in detail in the first PhD thesis on this experiment by Jürgen Fuchs [66]. To avoid repetition, this chapter highlights only the important aspects of the experiment. The major experimental changes introduced in this thesis work involve incorporating different laser locking schemes, setting up a tapered amplifier for a six-beam magneto-optical trap (MOT), absorption imaging at high magnetic fields and the optical setup for Bragg spectroscopy.

4.2 Experiment in a nutshell

All the experiments are performed in an ultra-high vacuum (UHV) environment. Each experimental sequence starts by slowing down a beam of hot ^{6}Li atoms exiting an oven

using a σ^- Zeeman slower [79]. From this slowed atomic beam, 4% of the atoms are cooled and trapped in a MOT created by six perpendicularly intersecting near-resonant laser beams. This Doppler cooled MOT contains about 10^8 atoms at a temperature of 280 μK. A small fraction (1%) of the atoms is then transferred from the MOT to an optical dipole trap. A high magnetic field is then turned on to make use of the broad Feshbach resonance of ^{6}Li at 834 G. The transferred atomic sample in the dipole trap has a roughly equal spin mixture of the two lowest hyperfine ground states ($|1\rangle$ and $|2\rangle$) of ^{6}Li. To obtain the temperatures required for degeneracy, the atomic sample is further cooled by forced evaporation. Once a degenerate gas is formed, the dipole trap is switched off and the gas is allowed to expand for a certain time of flight (TOF) before taking an absorption image on a CCD camera at high magnetic fields.

In addition, Bragg spectroscopy of strongly interacting degenerate gases is performed. This is achieved by shining counter-propagating Bragg beams either on an expanded cloud or on a trapped cloud at different magnetic fields across the BEC-BCS crossover. TOF absorption images taken in the presence of magnetic fields after the Bragg pulse reveal the properties of the degenerate gases. The entire experimental sequence is fully computer controlled with a 50 s duty cycle.

4.3 Vacuum system

Our vacuum system consists of two separate pumping chambers (six-way crosses) connected through a valve, a Zeeman slower, a glass cell and a bellow as shown in Fig. 4.1. The total length of the vacuum system is about 1.6 meters. All the vacuum components are supported on an optical table by 1.5 inch diameter steel posts. A description of each section of the apparatus is given below followed by an explanation of the procedure employed to obtain UHV in this system.

Oven: This is a 9 cm long copper tube that is attached to the left pumping chamber through a 10 cm long collimation nozzle. Lithium exists as a solid at room temperature

with a melting point of 181°C. Therefore, in order to increase its vapour pressure, the oven is heated to 420°C. The oven is loaded with 1 g of 95% isotopically enriched ^{6}Li. The temperature of the oven and nozzle is kept constant by heating with a thermocoax cable that is wound around them. Two cement blocks placed around the oven ensure thermal insulation from the surroundings. The nozzle, having an inner diameter of 4.5 mm, collimates the atoms exiting the oven and also maintains a pressure difference between the oven and pumping region.

Left pumping chamber: This six-way cross chamber connects to a 50 l/s ion pump on one side and a turbo-molecular pump on the other side. The turbo pump is connected through an angle steel valve and a bellow (see Fig. 4.1a). In addition, a titanium sublimation (Ti-sub) pump is placed on the upper port, whereas the lower port is attached to an in-house made mechanical shutter used for blocking the atomic beam coming from the oven (see Fig. 4.1b). This chamber is attached to the Zeeman slower through an all-metal straight-through valve which is used for isolating the two pumping chambers.

Zeeman slower tube: The Zeeman slower acts as a low-conduction tube for differential pumping and maintains the vacuum pressure difference between the two pumping chambers. It is a 30 cm long tube with an increasing inner diameter from the left end to the right end. The first two sections are each 10 cm long with inner diameters of 4 mm and 6 mm, respectively. In the next two 5 cm long sections the inner diameter increases to 8 mm and 10 mm, respectively. This type of design matches the focussed Zeeman slowing laser beam to address most of the atomic beam which diverges from the nozzle.

Glass cell: The heart of our experimental set-up is a custom-made glass cell which is 32 cm long. One end of the glass cell is attached to the Zeeman slower, and the other end is attached to the right pumping chamber via an edge-welded bellow, which reduces any stress or strain on the glass cell. The central part of the glass cell is a 12 cm long quartz square cross section with outer dimensions 3×3 cm^2. This is the region

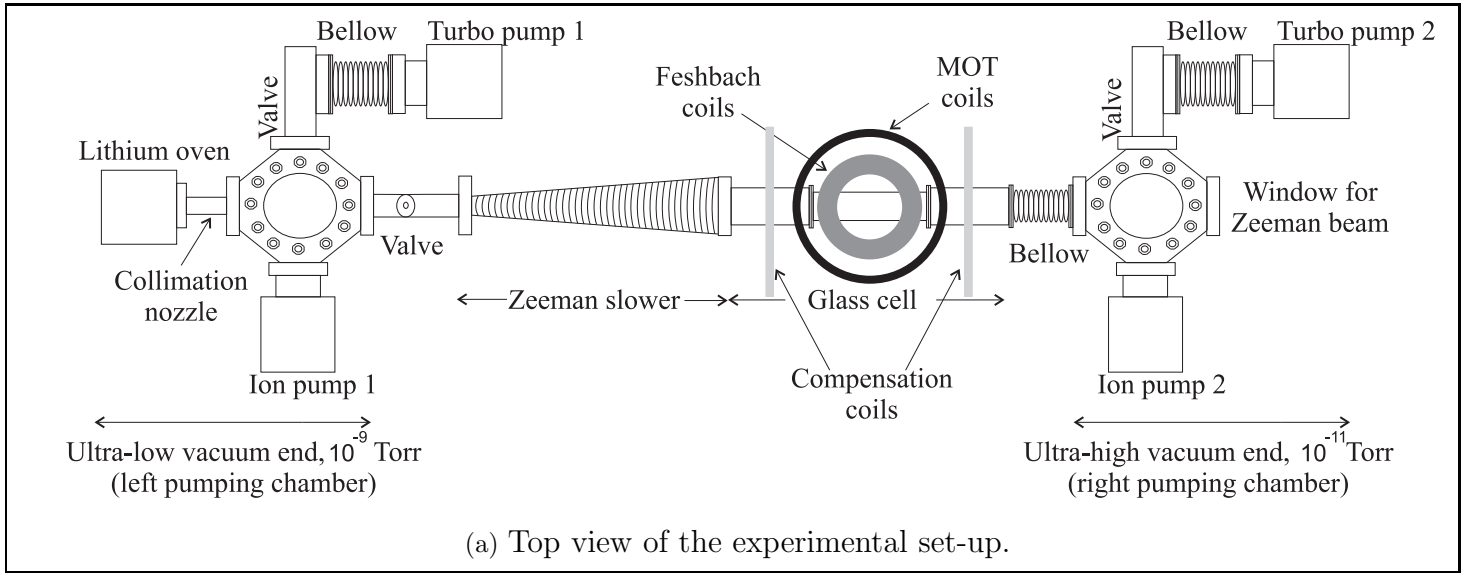

(a) Top view of the experimental set-up.

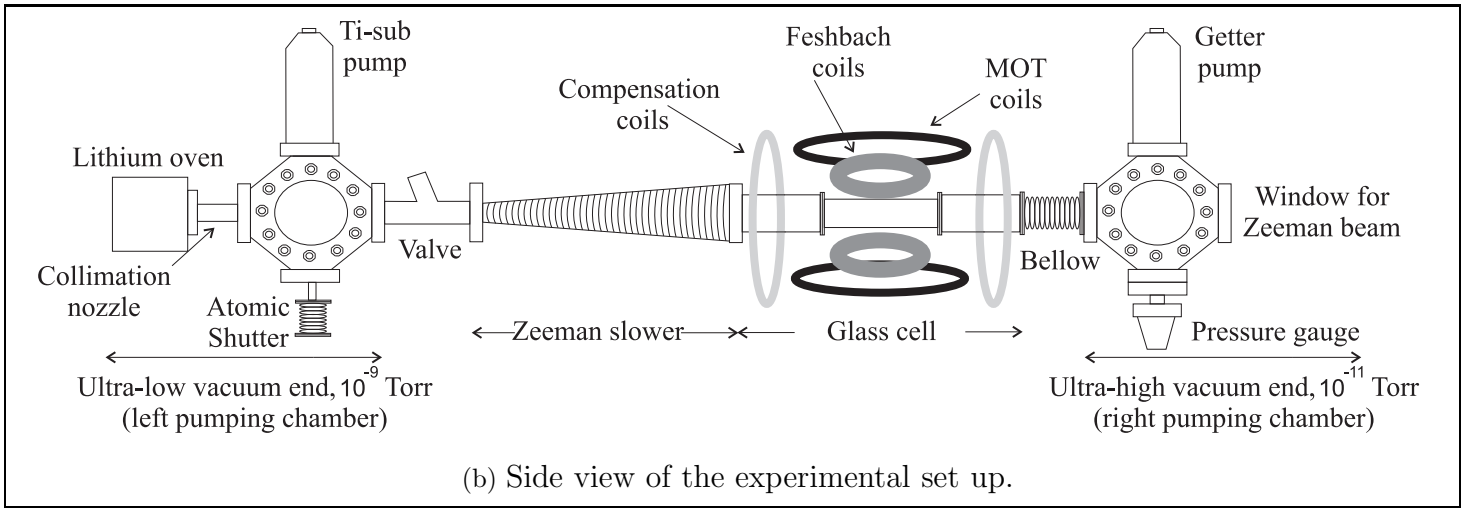

(b) Side view of the experimental set up.

Figure 4.1: Schematic view of the experimental set-up (not to scale).

where all the experiments take place. The outer surface of this part is anti-reflection coated for both 670 nm and 1030 nm laser light. On either side of this part, 10 cm long glass to metal transitions are fused which smoothly match the thermal expansion coefficients from quartz to steel.

Right pumping chamber: This six-way cross chamber also connects to a 50 l/s ion pump on one side and a turbo-molecular pump on the other side that is connected through an angle steel valve and a bellow (Fig. 4.1a). In addition, a non-evaporative getter pump is placed on the upper port whereas the lower port is attached to a cold-cathode pressure gauge to monitor the vacuum pressure at this end (Fig. 4.1b). The remaining port is sealed by a sapphire window for optical access of the Zeeman slower laser beam. The reason for using a sapphire viewport instead of glass is because lithium is highly corrosive to glass. In fact, this window is continuously heated to 80°C to minimize lithium deposition on it.

Achieving UHV: After assembling all the vacuum components as mentioned above, the turbo-molecular pumps are started first to pump out the system. Once the pressure inside the chambers reaches 10^{-6} Torr, it becomes harder to achieve further low pressure due to outgassing from the chamber walls. To overcome this, the entire vacuum system is baked (heated) to a high temperature (300°C) for six days to hasten outgassing and then cooled gradually to bring the pressure down to around 10^{-8} Torr. The glass cell is baked carefully by building a cage of aluminium bars around it and increasing the temperature in steps of only 5°C/hr to a maximum value of 150°C. By now, both the ion pumps start running and maintain the required pressure (10^{-9} Torr) in each chamber. An ion pump creates a region of high electric field between its electrodes. Any atoms wandering in this region are ionized and attracted towards the appropriate electrode.

To achieve a UHV pressure of less than 10^{-11} Torr, both the getter pump and titanium sublimation (Ti-sub) pumps are used. The Ti-sub pump coats the inner walls of the vacuum chambers with highly reactive titanium which absorbs non-inert gases.

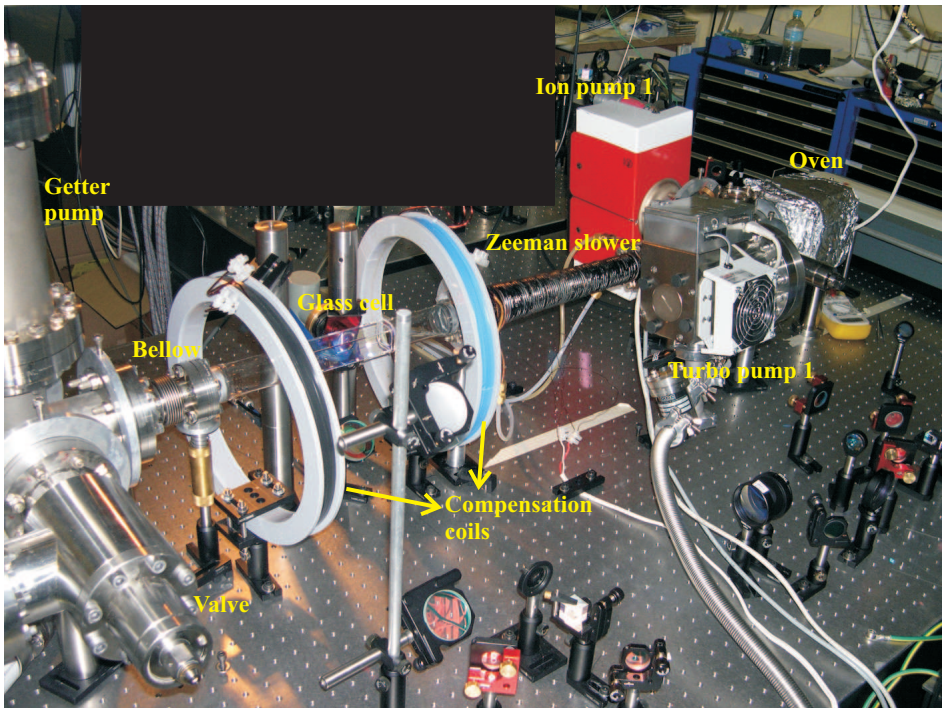

(a) Initial stage

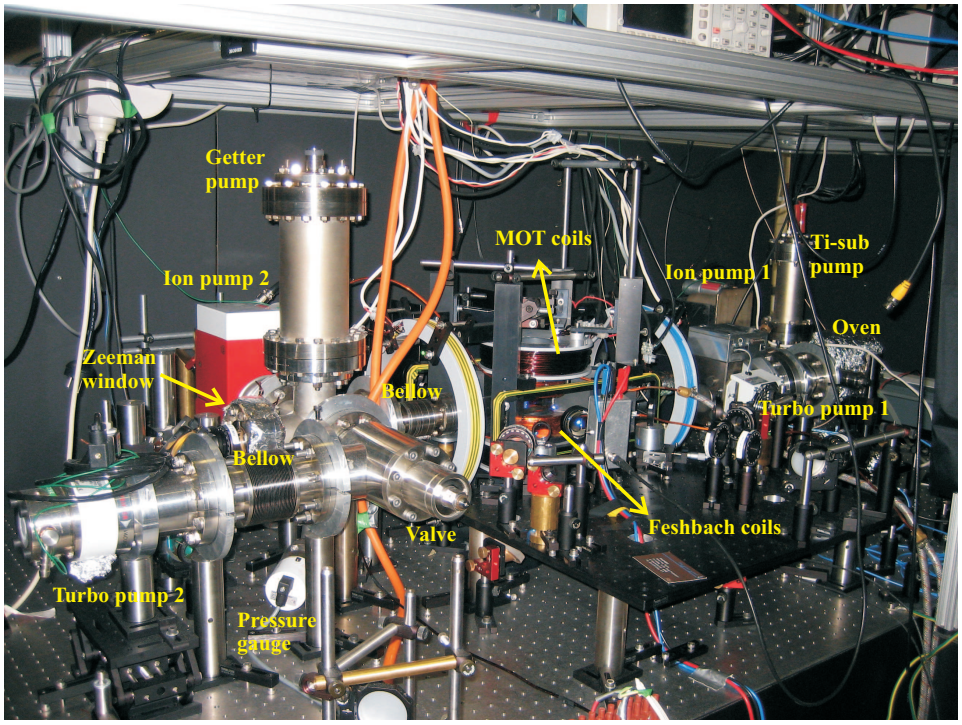

(b) Intermediate stage

Figure 4.2: Photographs of the experimental set-up.

This turns the chambers into an effective vacuum pump with a very high pumping speed until the layer becomes saturated. An ultimate equilibrium of vacuum pressures between the two chambers is obtained when the pumping rate equals the flux of atoms entering the glass cell. The pressure on the left pumping chamber is maintained at 10^{-9} Torr, as measured by the current in the ion pump, and on the right pumping chamber at 10^{-11} Torr as measured by the pressure gauge.

Figure 4.2 shows photographs of the experimental setup at an earlier stage and at an intermediate stage. In Fig. 4.2a, the glass cell, the Zeeman slower and the oven can be clearly seen, while in Fig. 4.2b, the MOT and Feshbach coils are seen along with the getter and Ti-sub pumps. The final stage of the experimental set-up (not shown) is similar to that in Fig. 4.2b except that the camera is placed on top of the Feshbach mounts for taking absorption images in the vertical direction.

4.4 Laser locking scheme

Figure 4.3 shows schematically the different laser frequencies employed in our experiment. Two independent external-cavity diode lasers (ECDL) and various acousto-optical modulators (AOMs) are used to produce all the required frequencies. Using saturation absorption spectroscopy, the frequency of an ECDL is locked and red-shifted by -250 MHz from the crossover of the two lowest hyperfine states of ^{6}Li. From this reference frequency, the trapping (repumping) beam is generated by blue-detuning the frequency by +110 MHz (+338 MHz) which is four line widths away from the F=3/2 (F=1/2) hyperfine state. Also, the Zeeman slower beam is obtained by red-detuning the frequency by -976 MHz from the F=3/2 hyperfine state.

A major improvement in our experimental setup is the implementation of offset-locking two ECDLs [65]. A second ECDL laser is combined with the first one, and the beat frequency signal is amplified before mixing with the frequency of a tunable voltage controlled oscillator (VCO) for offset-locking (see sec. 4.6). This locked frequency

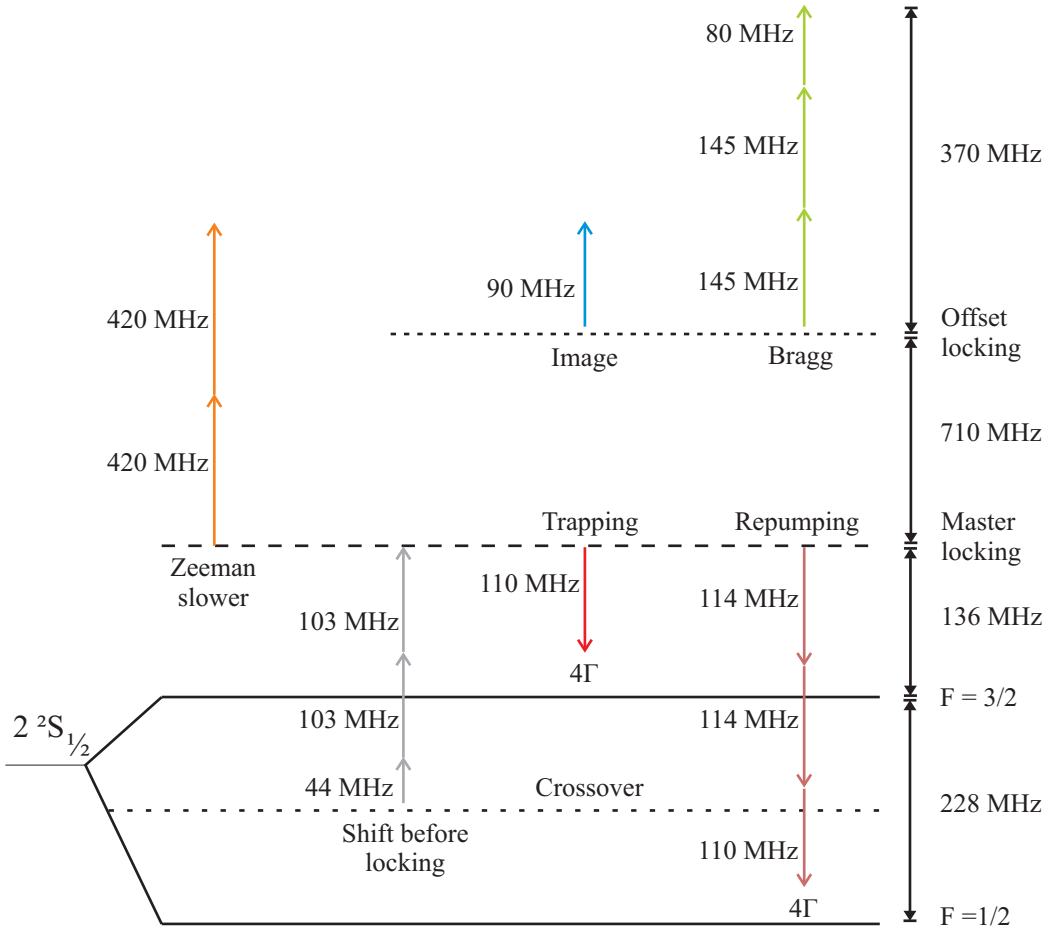

Figure 4.3: Laser locking scheme for generating various frequencies. The master laser is frequency red-shifted and locked at 250 MHz from the crossover peak. The Zeeman slower beam is red-detuned by 976 MHz from the F=3/2 state. The MOT (repump) beam is red-detuned by 4Γ from the F=3/2 (F=1/2) state. Another master laser is offset-locked with the main master laser and its frequency is red-shifted by 710 MHz. The frequency difference between the imaging and Bragg beams is always kept constant at 280 MHz. The vertical lines on the right give the range of frequencies involved (not to scale).

can be varied continuously by tuning the VCO voltage allowing absorption imaging at various high magnetic fields. For example, a VCO frequency of 710 MHz is needed to offset-lock the laser for imaging at 780 G. From this reference frequency, a near resonant laser frequency (from $|1\rangle$ to $|F' = 3/2, m_F = -3/2\rangle$) is obtained for imaging by red-shifting the frequency by -90 MHz. Also, two Bragg beams are generated by red-detuning the frequency by -370 MHz.

4.5 Optical set-up for a six-beam MOT

The inclusion of a tapered amplifier (BoosTA from *Toptica*, 670 nm, 0.5 W) into our optical system increased the available optical power and made it possible to realize a six-beam MOT. In order to incorporate this, the entire optical set-up has been modified. The laser frequency from the ECDL (*Toptica*, DL100), master laser-1, is first red-detuned by -206 MHz using an AOM in double-pass configuration (see Fig. 4.4). The laser beam is then passed into a spectroscopy cell which consists of a stainless steel tube with viewports at both ends. The central part of the spectroscopy cell is heated to 350°C to increase the lithium vapour pressure inside the cell and the viewports are heated to 120°C to avoid corrosion by lithium on the glass windows. The frequency of the laser is stabilized through saturation absorption spectroscopy where counter-propagating pump and probe beams are used. During the process, the frequency is further red-shifted by -44 MHz using an AOM and the saturated absorption signal obtained from the probe beam is focussed onto a photodiode. Using a lock-in amplifier, a derivative of this signal is obtained and the laser is locked to the crossover of the D2-transition of ^{6}Li.

The laser power from this master laser-1 is amplified by injection-locking a diode slave laser-1 in a master-slave configuration. Light from the slave laser is then split into three paths. The first path is used for offset-locking a second ECDL for creating

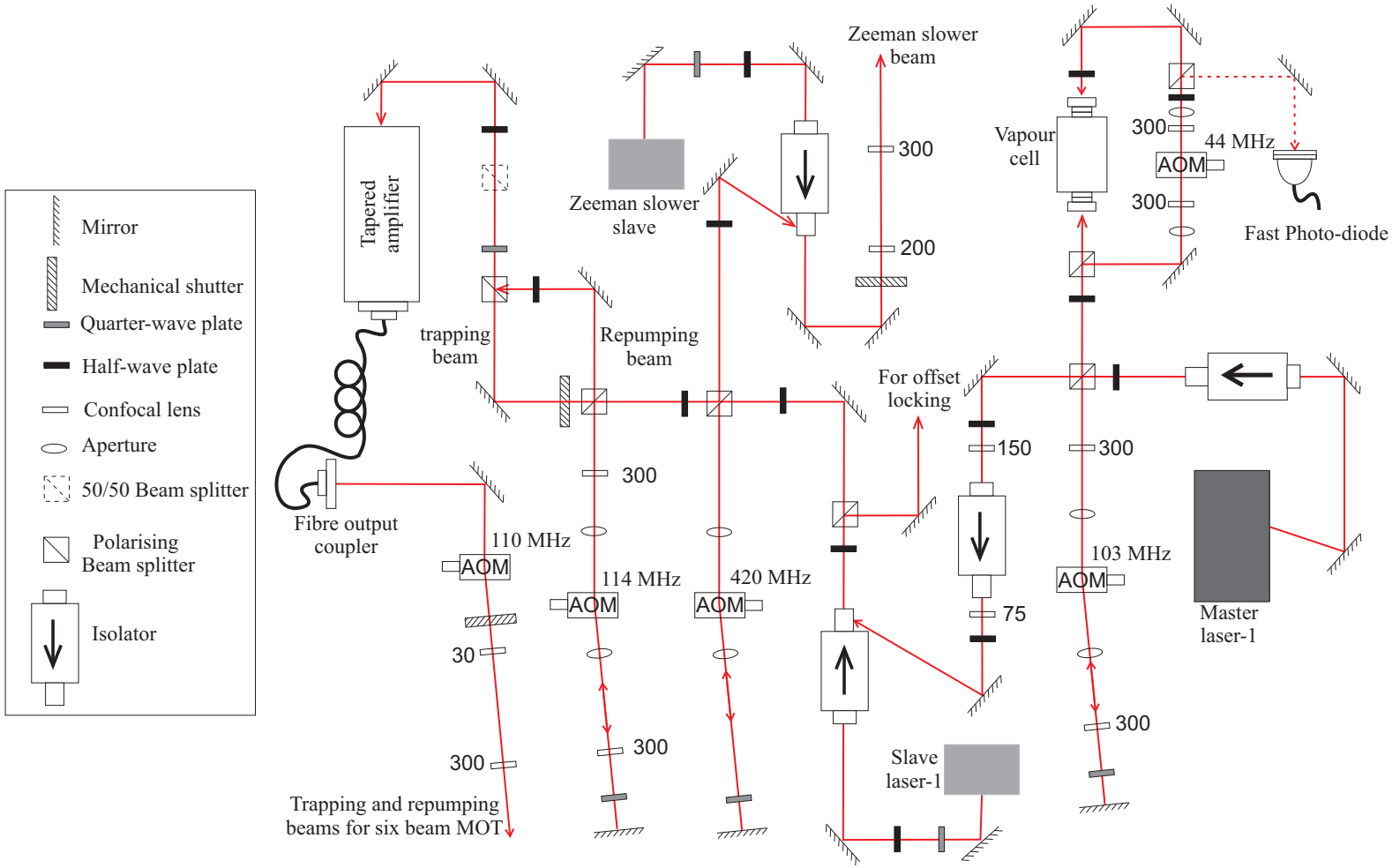

Figure 4.4: Optical set-up for creating the MOT and Zeeman slower beams. The numbers next to lens indicate its focal length in mm.

the imaging and Bragg beams. The second path is used to injection-lock another diode slave laser for generating the Zeeman slower beam after passing through a -420 MHz AOM (*Intraaction*) in double-pass configuration. In order to enhance the flux of slowed atoms for the MOT loading, the diode laser current is modulated at 120 MHz which adds sidebands to the central frequency. The Zeeman beam is focussed into a pin hole (300 μm) to remove the high spatial frequency components from the beam profile. It is then expanded to a diameter of 1 inch using a 200 mm and 300 mm lens arrangement. This beam is weakly focussed into the oven end using a large focal length (1000 mm) lens placed before the sapphire window.

The third beam is passed through a -114 MHz AOM in double-pass configuration to obtain the repumper beam. This beam is then combined with the trapping beam on a 50/50 beam splitter before being sent into the TA. The power in each beam is 2.5 mW at this point and the TA amplifies it by a factor of 30. The output from the TA is coupled to a single-mode optical fibre to obtain a clean Gaussian beam profile. This is focussed into a +110 MHz AOM in a single-pass configuration which brings the frequency of the combined trapping and repumping beams closer to four linewidths (4Γ) away from the atomic resonance. The diameter of this combined MOT beam is expanded to 25 mm from 2.5 mm using a 30/300 mm lens arrangement to achieve a large MOT trapping volume. This beam is later split in six ways ($\sim$13 mW in each) to construct a six-beam MOT.

4.6 Offset-locking scheme

In order to image at high magnetic fields, an offset-locking technique is implemented using two ECDLs [65]. The wavelength of the imaging master laser-2 is set around 670.977 nm (D2 line) with the help of a wavemeter. Laser light from the slave laser-1 is then allowed to beat with a beam from the master laser-2 and the beat signal is observed on a fast photo-diode. This beat signal is amplified (Fig. 4.5) and mixed with

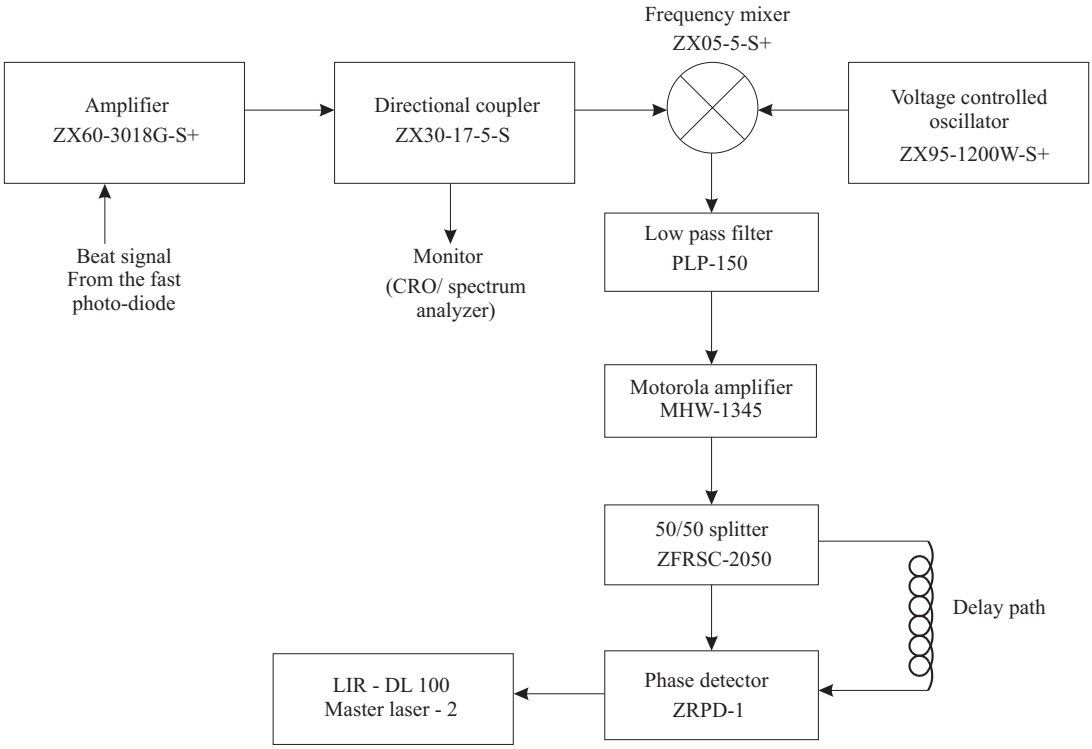

Figure 4.5: Block diagram for offset-locking electronics. Part numbers are from *MiniCircuits*

the frequency of a tunable VCO (600 - 1200 MHz), following which the low frequencies ($\leq$140 MHz) are filtered and further amplified before being split into two equal signals. One is passed through a long (5 m) cable to introduce a frequency dependent phase shift with respect to the other signal which is measured by a phase detector. This second beat signal is used as an error signal for locking master laser-2 (*Toptica*, DL100). The frequency of the laser can be precisely adjusted by tuning the voltage (frequency) of the VCO over a range of 600 MHz.

A slave diode laser-2 is injection-locked by the locked laser light from master laser-2 and then split into two paths (Fig. 4.6), one for absorption imaging and the other for generating Bragg beams. The imaging beam is first frequency-shifted ($-$90 MHz) by an AOM before being coupled into a single-mode polarization-maintaining fibre.

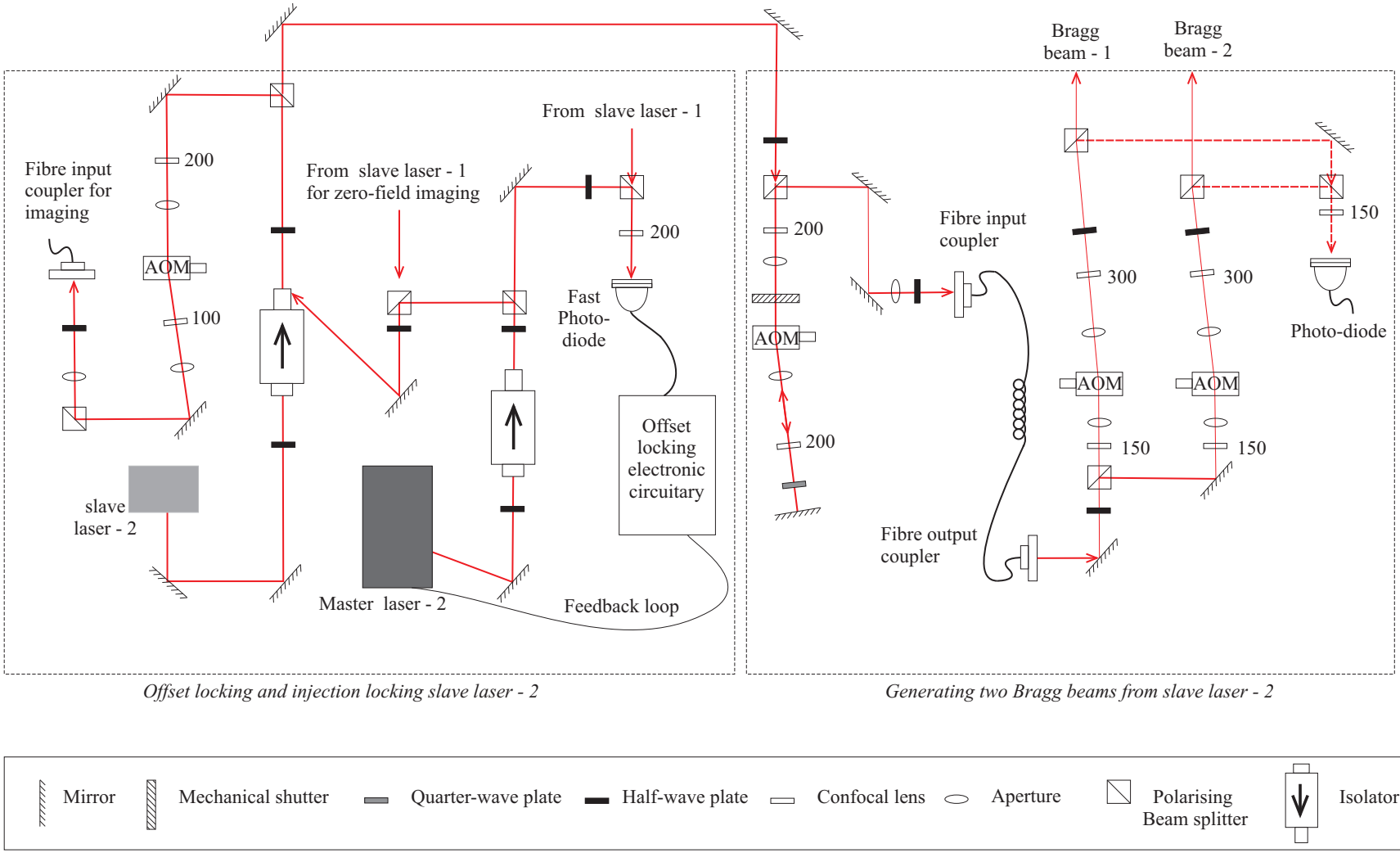

Figure 4.6: Optical set-up for offset-locking, injection-locking, and generating the imaging and Bragg laser frequencies.

4.7 Generating Bragg beams

The Bragg beam derived from the slave laser-2 is first frequency-shifted (-210 MHz) by an AOM in double-pass configuration before being coupled into a single-mode polarization-maintaining fibre. After the fibre the beam is separated into two and the frequency of each beam is shifted (-80 MHz) by two different single-pass AOMs as shown in Fig. 4.6. A small pick-off beam (dotted lines) is taken from each Bragg beam and combined on a fast photodiode to monitor their beat frequency.

The two Bragg AOMs are driven by two separate VCOs. Using a spectrum analyzer, it has been verified that for the Bragg frequencies applied in our experiments ($\delta/2\pi = 0 - 500$ kHz), no phase lock loop is needed for the AOMs to keep the beat frequency stable, as long as the supplied tuning voltage for the VCOs is stable and taken from a common DC power supply. For this purpose, the DC voltage for each VCO is obtained from a voltage regulator (LM-317) with an additional voltage applied to one VCO that is derived from the *LabView* control program. The *LabView* voltage is first stepped down by a factor of 20 before being added to one of the VCOs. This improves the stability and accuracy of the voltage from the *LabView* control and allows the Bragg frequency to be tuned precisely. The full width at half maximum (FWHM) of the observed beat signal is 0.2 kHz and its day-to-day stability is up to 2 kHz. By keeping the tuning voltage of one VCO constant, the beat (Bragg) frequency is varied in steps of 5 kHz by tuning the voltage of the other VCO.

The collimated Bragg beams are directed near-perpendicular to the weak axis of the single dipole trap. Two polarizing beam splitters are placed before the glass cell (see Fig. 4.9) to ensure that the Bragg beams have vertical polarization as they enter the glass cell. Using a spare (broken) glass cell, identical to the one in the experiment, it has been verified that the polarization of $\lambda = 671$ nm light varies by less than 5% upon transmission through the cell window. For maximum overlap, each beam is aligned in such a way that it retraces the path of the other beam.

4.8 Single dipole trap set-up

A 100 Watt CW Ytterbium fibre laser (*IPG-Photonics*, YLR-100) is used for creating the single dipole trap. Its central wavelength is 1075 nm with many longitudinal modes distributed within 3 nm. The laser light has linear polarization and a near Gaussian beam profile (M^2 $\leq$1.05). The beam diameter is first reduced from 5 mm to 1 mm using a step-down telescope with a 250 mm and -50 mm lens arrangement as shown in Fig. 4.7. After this, the laser beam is passed through a PID controlled AOM (-120 MHz) which is used to stabilize the intensity of the laser during the evaporative cooling stage by dumping the power in zeroth order. The negative first-order beam from the AOM is then expanded using a -100 mm lens and focussed to a 38 μm beam waist into the glass cell with the help of another 200 mm lens that is placed on a translational stage. The focussed beam is blocked by a beam dump after passing through the glass cell. Before dumping, a low intensity beam is picked off and focussed onto a photodiode to generate an error signal for the PID controller (*SRS*, SIM 960) with respect to a setpoint voltage from the *LabView* program. This determines the amount of radio-frequency (RF) power required for the AOM to stabilize the intensity of the laser light.

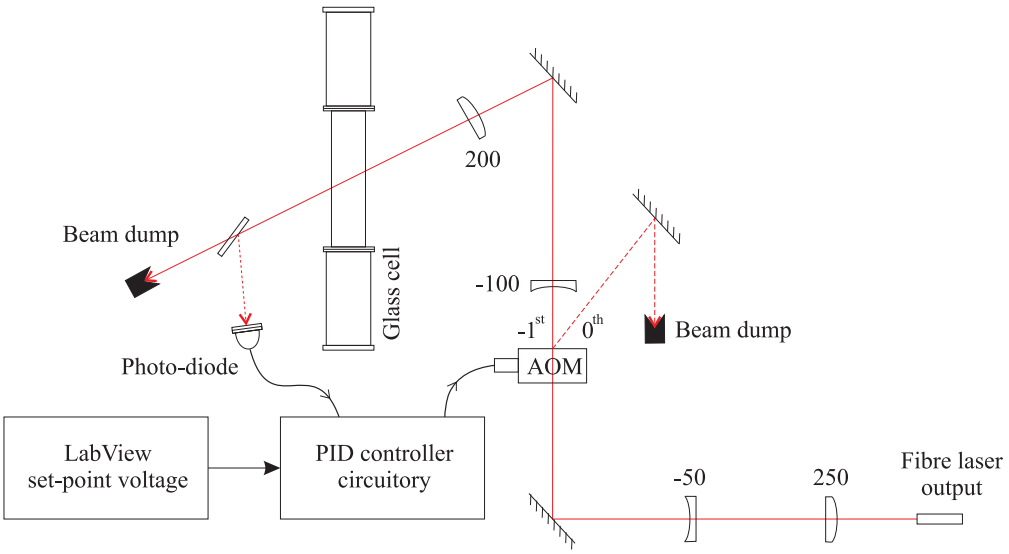

Figure 4.7: Optical set-up for implementing the single dipole trap.

4.9 Absorption imaging

All the scientific information about our experiments is obtained from absorption images. This information includes cloud position, width and density. The idea is to illuminate the atomic cloud with near-resonant laser light to cast a shadow onto a CCD camera placed behind it. To remove any inhomogeneities in the probe beam profile, a second absorption image is taken after 360 ms in the absence of the atomic cloud. Absorption imaging is a destructive technique where an atom absorbs resonant light thereby heating the atoms. For a second measurement the whole preparation process has to be repeated. If the intensity of the first image is $I(x, y)$ and that of second image is $I_o(x, y)$ then the atomic column density $n(x, y, z)$ is evaluated using the relation

$$\frac{I(x,y)}{I_o(x,y)} = e^{-\sigma \int n(x,y,z)\ dz} \tag{4.1}$$

where σ is the absorption cross section and the imaging beam propagates in the z-direction. For a two-level system the resonant cross section is given by $\sigma = 3\lambda^2/2\pi$. The image of the cloud is magnified by a factor of two in order to achieve an imaging resolution of 3 μm.

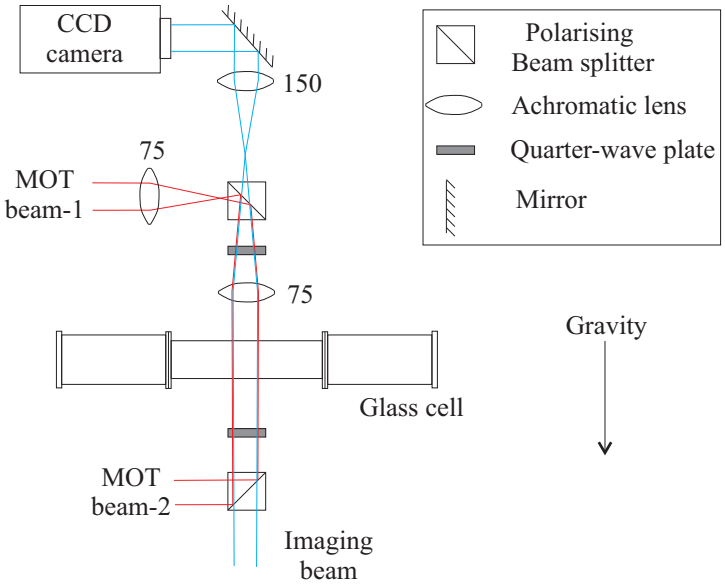

Figure 4.8: Optical set-up for implementing absorption imaging.

The imaging laser beam derived from slave laser-2 is brought close to the glass cell through an optical fibre. The beam from the fibre output coupler is collimated to a diameter of 200 mm using a 60 mm lens. It is then combined with one of the vertical MOT beams on a polarizing beam splitter before being sent through the glass cell along the direction of the Feshbach fields (see Fig. 4.8). The image of the atomic cloud is magnified by a factor of two using two 2-inch achromatic lenses with focal lengths of 75 mm and 150 mm, respectively. Another 75 mm convex lens is used to collimate a second MOT beam from the top of the glass cell as shown in Fig. 4.8.

4.10 Experimental sequence

In this section the steps followed during the experiment to create and study degenerate quantum gases are explained. Technical details such as ramp timings, frequencies and currents applied in the various coils are also given.

Slowed atomic beam:

A vapour pressure of 1.2×10^{-4} mbar is created in the oven containing 95% isotopically enriched ^{6}Li atoms by constantly heating it to 420°C. The average velocity of the atoms at this temperature is around 1500 m/s with a negligible collision rate due to their large mean free path. As they pass through the Zeeman slower coil, atoms with velocities below 650 m/s are selectively slowed to 50 m/s by means of a counter-propagating Zeeman laser beam which is red-detuned from the $|F{=}3/2\rangle$ state by -976 MHz. Additional sidebands are added to this frequency by modulating the current of Zeeman slave laser diode by 120 MHz which increased the flux of slowed atoms by a factor of two to 10^9 atoms/s. During the loading time (20 s), the current in the Zeeman slower coil is maintained at 2.94 A to create a slowly varying magnetic field of up to 620 G towards the glass cell end.

MOT loading:

From this slowed atomic beam, 4% of the atoms are cooled and trapped in a MOT created by six perpendicularly intersecting laser beams. The four horizontal beams are shown schematically in Fig. 4.9 with the two vertical beams perpendicular to the plane of the page. These beams are red-detuned by four linewidths from the atomic resonance (D2-transition) and have five times the saturation intensity. The MOT magnetic gradient of 20 G/cm is produced by a pair of current-carrying coils in an anti-Helmholtz configuration placed above and below the glass cell. At the end of this stage, the MOT contains more than 10^8 atoms at a temperature of 1 mK with a lifetime of 60 seconds.

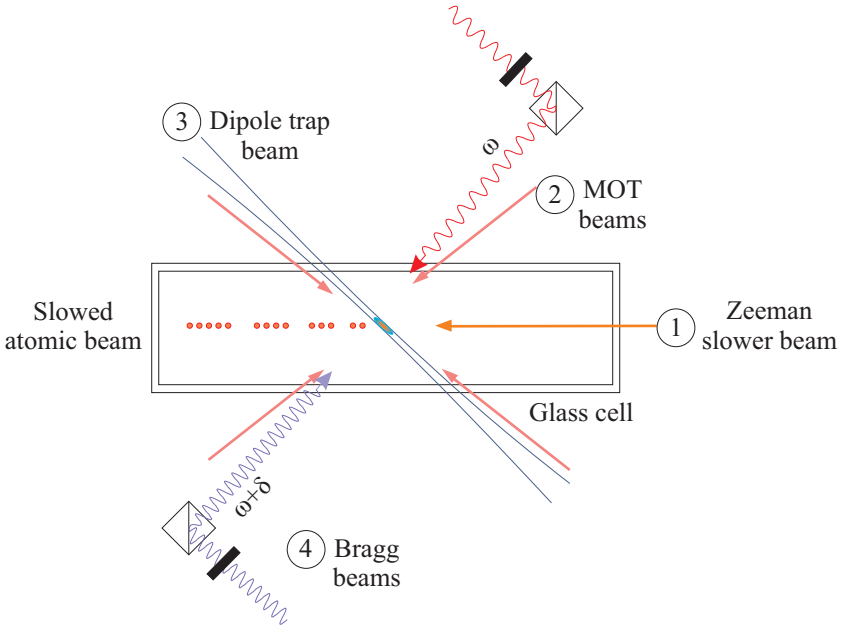

Figure 4.9: Schematic view of the experimental sequence in the science cell. Numbers indicate the steps followed during the experiment. First, Lithium atoms are slowed using a Zeeman slower, followed by cooling and trapping in a MOT. Later the atoms are transferred from the MOT to the dipole trap. Once a degenerate gas is formed after evaporative cooling in the dipole trap, the Bragg beams are shone on the gas before taking a time of flight absorption image. The MOT coils, Feshbach coils and imaging beam are not shown as they are perpendicular to the plane of the page.

Dipole trap loading:

For efficient loading of atoms into the optical dipole trap, the temperature of atoms in the MOT should be lower and the atomic density should be higher to obtain a high phase space density:

$$D = n\left(\frac{2\pi\hbar^2}{mk_BT}\right)^{\frac{3}{2}}, \tag{4.2}$$

where n is the density and T is its temperature. To achieve this, the frequency of both the trapping and repumping laser beams is detuned to half a line-width before loading into the dipole trap. In addition, the repumper intensity is reduced more rapidly than the trapping laser to achieve optical pumping into the $|F{=}1/2\rangle$ state. This reduces the temperature in the MOT to $\sim$280 μK which is twice the limiting Doppler temperature of 140 μK. At the same time, the magnetic field gradient is linearly increased from 20 G/cm to 50 G/cm in 20 ms to increase the density of the MOT. A small fraction (1%) of atoms is then transferred from the MOT into the dipole trap which is switched on 100 ms before the compression stage. After loading the dipole trap, the Feshbach magnetic field is then turned on for evaporative cooling. Feshbach fields of up to 1.5 kG can be achieved in our experiment using a pair of water cooled, low inductance (433 μH), high current-carrying (200 A) coils. They are placed very close (2 mm) to above and below the glass cell to obtain high fields in a Helmholtz configuration.

Evaporative cooling:

Owing to the large elastic collision rate ($\sim 10^4$ s^{-1}), the plain evaporation process starts immediately in the dipole trap with full laser power (90 W). Nevertheless, this process stagnates after 500 ms as fewer and fewer high energy atoms leave the trap. To obtain the temperatures required for degeneracy, the atomic sample is further cooled by forced evaporation. This is carried out in two steps. Initially, the trap depth is decreased by reducing the intensity of the dipole trap laser from 90 W to 12 W in 1.5 s simply by decreasing its current via an analog control voltage. During this time, the photo-diode which monitors laser intensity (see Fig. 4.7) from the pick-up beam

remains saturated. However, once the optical power drops below 12 W, the photodiode is no longer saturated and the signal is sent to a PID controller. The dipole trap intensity is further reduced by a factor of 100 over the next 4 s using a logarithmic ramp sent to the PID controller.

Bragg scattering:

Once a degenerate gas is formed in the dipole trap, the Feshbach magnetic field can be adiabatically ramped in 100 ms to a value where Bragg spectroscopy is to be performed. In the meantime, the trap depth is increased by a factor of two from the lowest evaporation value to confine the gas at the bottom of the trap. A short Bragg pulse can then be applied to study the properties of the gas. An absorption image is taken after a 3 ms TOF, once all the non-imaging lasers are switched off. From these image profiles, all the important physical information can be obtained by fitting various distribution functions to the gas.

4.11 Summary

This chapter briefly described the experimental set-up and procedures implemented in our lab to achieve highly degenerate quantum gases. Discussion of various topics is kept concise to focus more on Bragg scattering which is the main topic of the thesis. Additional details on saturation absorption spectroscopy, computer control, the Zeeman slower and other coils can be found in the PhD thesis of Jürgen Fuchs [66]. The major advantage with the new experimental set-up compared to the earlier one is the implementation of a six-beam MOT and the employment of offset-locking for high magnetic field imaging. As a consequence of these changes a large number of atoms $\sim 10^6$ are now trapped in a single dipole trap without requiring the use of a crossed dipole trap.

Chapter 5

Production of quantum degenerate gases

5.1 Introduction

In this chapter, the generation of ultracold degenerate gases in our experimental system is described. Since the theoretical and experimental process behind these techniques are well understood and documented [79], only a brief review is given for each topic. For a more detailed discussion the reader is referred to the classic papers on these subjects such as [13, 14, 15, 16]. Creating a MOT from a slowed atomic beam is the first step for producing degenerate gases. In our experiment, the atoms are trapped by all optical means after they are transferred from the MOT to a dipole trap. Following that, atoms in the dipole trap are cooled by forced evaporation, in the presence of a Feshbach magnetic fields, to form either a molecular BEC or a degenerate Fermi gas.

5.2 Magneto-optical trap

Atoms can be cooled optically by the application of a radiative force using near-resonant optical fields and trapped in the presence of a spatially varying magnetic field. When an atom absorbs a photon with momentum $\hbar\vec{k}$, where $\vec{k}$ is the wave vector of the photon, it is first excited followed by spontaneous emission of a photon with the same frequency to relax back to its initial state. Due to the isotropic distribution and large number of scattered photons, the atom experiences a net resulting force of

$$\vec{F}_{\mathrm{sp}} = \hbar\vec{k}\Gamma_{\mathrm{S}}, \tag{5.1}$$

in the direction of the laser beam, where the scattering rate Γ_{S} describes the rate at which photons are absorbed and spontaneously emitted. Its value depends on the initial velocity $\vec{v}$ of the atoms, the laser intensity I and the frequency detuning from the atomic resonance ω_0:

$$\delta' = \delta - \vec{k}\cdot\vec{v}, \tag{5.2}$$

where $\delta = \omega - \omega_0$. The scattering rate is given by [79]

$$\Gamma_{\mathrm{S}} = \frac{1}{2}\Gamma\frac{I/I_{\mathrm{s}}}{1 + I/I_{\mathrm{s}} + (2\delta'/\Gamma)^2}, \tag{5.3}$$

where Γ is the natural linewidth and I_{s} is the saturation intensity. The values for the closed transition in ^{6}Li are $I_{\mathrm{s}} = 2.5$ mW/cm^2 and $\Gamma = 2\pi \cdot 5.9$ MHz [82, 80].

Counter-propagating circularly polarized ($\sigma^{\pm}$) laser beams can be used in all three directions to slow down the atoms. However, for spatial confinement, a magnetic field gradient is also required. This is created by a pair of current-carrying coils arranged in an anti-Helmholtz configuration. The detuning of the laser is then changes to

$$\delta_{\pm} = \delta - \vec{k}\cdot\vec{v} \mp (g_e m_{F'} - g_g m_F)\mu_B B/\hbar, \tag{5.4}$$

where g_e and g_g are the Landé g-factors of the excited and ground state, respectively. In the presence of the MOT magnetic field, the degeneracy of the ^{6}Li hyperfine states is lifted. The net force due to the two counter-propagating circularly polarized beams in one dimension is given by

$$\vec{F}_{\rm total} = \vec{F}_+ + \vec{F}_- = \frac{\hbar\vec{k}\Gamma}{2}\frac{I/I_{\rm s}}{1+I/I_{\rm s}+[2(\delta_+/\Gamma)]^2} - \frac{\hbar\vec{k}\Gamma}{2}\frac{I/I_{\rm s}}{1+I/I_{\rm s}+[2(\delta_-/\Gamma)]^2}.$$

At low intensity and large detuning, the above equation is simplified to obtain

$$\vec{F} = -\beta\vec{v} - \kappa\vec{r}, \tag{5.5}$$

where the damping constant β and the spring constant κ are given by

$$\beta = \frac{8\hbar k^2 \delta I/I_{\rm s}}{\Gamma(1+I/I_{\rm s}+(2\delta/\Gamma)^2)^2}, \tag{5.6}$$

$$\kappa = \frac{(g_e m_{F'} - g_g m_F)\mu_{\rm B} A}{\hbar k}\beta. \tag{5.7}$$

For red detuning ($\delta < 0$), the constant β is positive. Therefore, the first term in eq. 5.5 is a damping force, whereas the second term confines the atoms spatially towards the centre of the trap (magnetic minimum). The same results apply in three dimensions for a six-beam MOT.

For ^{6}Li, the frequency of the trapping beams is tuned to the red of the $|F = 3/2; m_F = \pm 3/2\rangle \leftrightarrow |F' = 5/2; m_{F'} = \pm 5/2\rangle$ cycling transition. This is also the same transition used for the Zeeman slower laser to create a slowed atomic beam in combination with Zeeman coils. Because the detuning of the Zeeman slower beam is very large ($\simeq$1 GHz) compared to that of the trapping beam (4Γ), it passes through the MOT with no measurable effect during the MOT loading period. In addition, to avoid spontaneous decay of atoms into the $|F = 1/2\rangle$ state, a repumper beam which is red-detuned to the $|F = 1/2; m_F = \pm 1/2\rangle \leftrightarrow |F' = 3/2; m_{F'} = \pm 3/2\rangle$ transition is combined with the trapping beam before constructing a six-beam MOT.

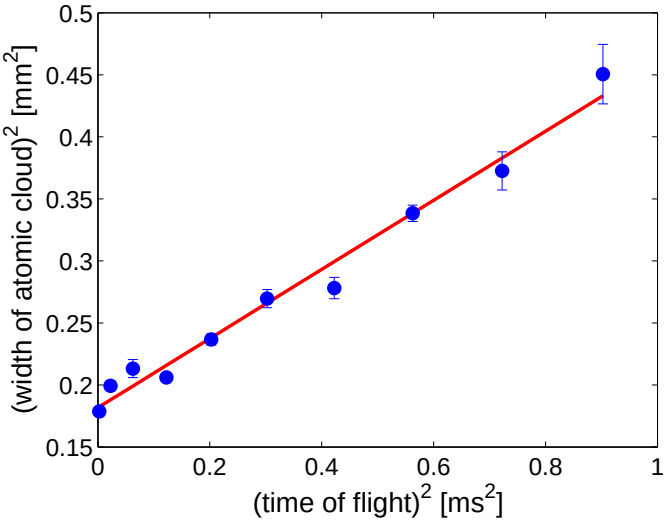

Figure 5.1: Temperature measurement of the MOT with 10^8 atoms. The radial width squared is plotted versus the time of flight squared. Error bars are from the statistical average.

In our experiments, the loading and trapping of atoms in the MOT is achieved as explained in section. 4.10. Absorption images of atoms released from the MOT are taken at zero magnetic field after various times of flight t between 100 μs and 1 ms. The width of the released atom cloud $\sigma(t)$ increases according to the relation

$$\sigma(t) = \sqrt{\sigma_0^2 + \frac{k_B T}{m} t^2}, \tag{5.8}$$

where σ_0 is the initial MOT width. Figure 5.1 shows the radial width squared of the MOT versus the time of flight squared. From a straight line fit to this data, the temperature in the MOT is evaluated to be 280(15) μK.

5.3 Single dipole trap

The interaction of neutral atoms with an optical field is exploited in implementing optical dipole traps. The electric component $\mathbf{E}$ in the optical field induces a dipole moment $\mathbf{p} = \alpha\mathbf{E}$ in an atom, where α is the atomic polarizability. This induced dipole

moment then interacts with the oscillating electric field **E** of the laser giving rise to the dipole potential $U_{dip} = -\frac{1}{2}\langle \mathbf{pE} \rangle$. Note that α is a complex quantity whose real part gives rise to a dipole force (conservative potential) and the imaginary part gives rise to a scattering force (radiation pressure). For effective trapping of atoms, the scattering component should be negligible compared to the dipole force. An expression for both the dipole potential and the scattering rate (Γ_{scat}) can be obtained from the atomic polarizability as derived in various references [79, 83] for a two-level system:

$$U_{dip}(\mathbf{r}) = -\frac{3\pi c^2}{2\omega_0^3}\Big(\frac{\Gamma}{\omega_0 - \omega} + \frac{\Gamma}{\omega_0 + \omega}\Big) I(\mathbf{r}) \tag{5.9}$$

$$\Gamma_{scat}(\mathbf{r}) = -\frac{3\pi c^2}{2\hbar\omega_0^3}\Big(\frac{\omega}{\omega_0}\Big)^3\Big(\frac{\Gamma}{\omega_0 - \omega} + \frac{\Gamma}{\omega_0 + \omega}\Big)^2 I(\mathbf{r}). \tag{5.10}$$

where c is the speed of light, ω_0 the atomic transition frequency, ω the driving laser field frequency, Γ the natural linewidth and $I(\mathbf{r})$ the position-dependent laser field intensity. From the above relations, it is clear that for a large detuning $\Delta = \omega_0 - \omega$, the scattering rate is minimized which varies as $1/\Delta^2$ while the conservative dipole potential only varies as $1/\Delta$.

Experimentally, a single dipole trap is achieved by focussing a far-detuned Gaussian laser beam to a narrow waist. The intensity distribution for a Gaussian beam with power P is

$$I(r, z) = \frac{2P}{\pi w^2(z)} \exp\Big(-2\frac{r^2}{w^2(z)}\Big) \tag{5.11}$$

where $w(z)$ is the beam waist along the beam direction (z) which is given by

$$w(z) = \mathrm{w}_0\sqrt{1 + \Big(\frac{z}{z_R}\Big)^2} \tag{5.12}$$

where $z_R = \pi \mathrm{w}_0^2/\lambda$ is the Rayleigh length of the focussed beam and λ is the wavelength of the laser. The waist w_0 is defined as the $1/e^2$ minimum radius. This parameter was measured in our optical set-up using the *IPG* fibre laser outside the glass cell and a razor blade fixed on a moving translation stage. The beam is blocked perpendicularly by the razor blade to record laser powers corresponding to 13.6% and 84.4% of the

peak power on the power meter placed behind it. The difference between the two razor positions directly gives the beam waist. The measurements are shown in Fig. 5.2. By fitting eq. 5.12 to the data a minimum beam waist of 38(1) μm is obtained.

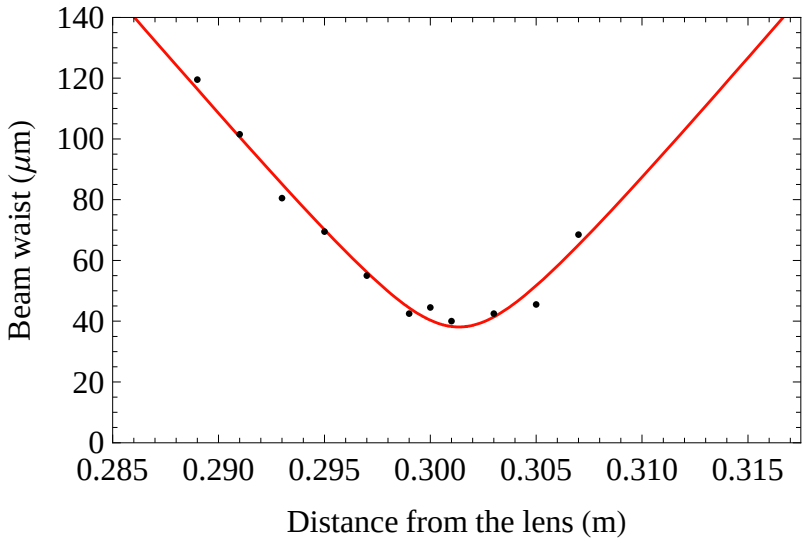

Figure 5.2: Beam waist measurement of the focussed Gaussian laser beam used for the dipole trap

5.3.1 Trapping frequencies

To trap neutral atoms in their ground state a red-detuned laser is used so that atoms accumulate in the high intensity region of the laser beam. A dipole trap can be formed by a single focussed laser beam which has tight confinement along the radial direction and weak confinement along the axial direction. The atoms in such a trap appear as an elongated, cigar-shaped cloud. To determine the trapping frequencies along both directions, the trap potential near the bottom of the trap is approximated to that of a harmonic oscillator. This is a valid assumption when the temperature of the atoms is smaller than the trap depth which is mostly true in our experiments. After Taylor expanding eq. 5.9, we get

$$U_{dip}(\mathbf{r}) \simeq -U_0\Big[1 - 2\Big(\frac{r}{w_0}\Big)^2 - \Big(\frac{z}{z_R}\Big)^2\Big] \tag{5.13}$$

which is compared to a harmonic oscillator potential to obtain expressions for the radial and axial trapping frequencies:

$$\omega_r = \sqrt{\frac{4U_0}{mw_0^2}} \qquad \text{and} \qquad \omega_z = \sqrt{\frac{2U_0}{mz_R^2}}, \tag{5.14}$$

where U_0 is the maximum trap depth at the centre of the trap, i.e., when $r = z = 0$. Note that both the atoms and molecules experience the same trapping frequencies. This is because the polarizability of molecules is twice that of atoms which compensates for their doubled mass.

Measurements:

For the parameters used in our experiments $\lambda_0 = 671$ nm, $\lambda = 1075$ nm and $\Gamma/2\pi = 5.9$ MHz, the trap depth is calculated to be 3 mK at a power of $P = 90$ W and the trap frequencies are given by

$$\omega_r = 2\pi\ 1600\ \sqrt{P/\mathrm{W}}\ \mathrm{Hz} \tag{5.15}$$

$$\omega_z = 2\pi\ 10\ \sqrt{P/\mathrm{W}}\ \mathrm{Hz} \tag{5.16}$$

During the evaporation process, in the presence of the Feshbach magnetic field, the axial confinement in a single dipole trap becomes weak at low laser power. However, the magnetic field curvature from the Feshbach coils provides additional confinement along the axial direction of the trap. This curvature in the horizontal plane is measured to be $0.024(3)\times B$ cm^{-2}. Therefore, the effective axial trap frequency can be written as [66]

$$\omega_z = \sqrt{814(180)\, B/\mathrm{kG} + 13.6(4)\, P/\mathrm{mW}}\ \mathrm{Hz}. \tag{5.17}$$

At a fixed low laser power, this axial frequency only varies with the square root of the Feshbach magnetic field applied in our experiments (700 G to 1000 G).

The axial frequency is measured by observing the oscillations of the cloud along the weak trap axis. Initially, the atomic sample is evaporatively cooled at unitarity to the

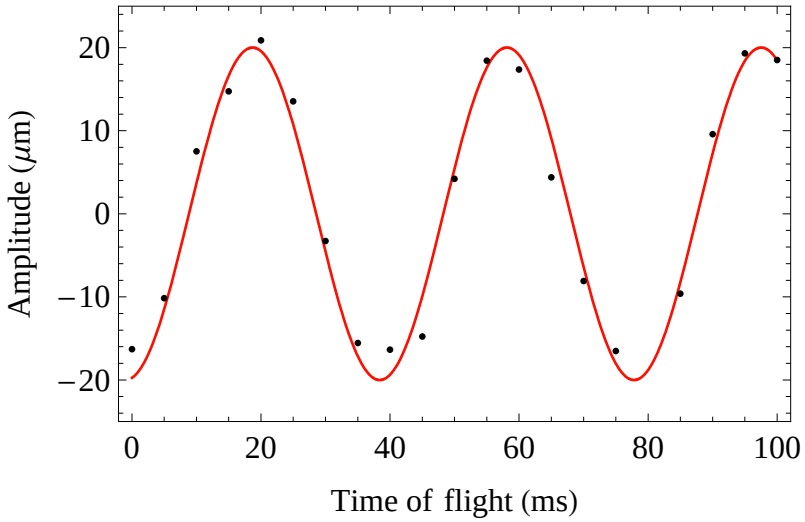

Figure 5.3: Oscillations of the atomic cloud along the axial direction of the dipole trap.

lowest trap depth possible. Then the cloud is shifted from its initial position using an auxiliary magnetic field gradient and then absorption images are taken after various hold times. Figure 5.3 shows the measured axial position of the oscillating cloud with respect to time. A sinusoidal fit to the data yields an axial frequency of 25(1) Hz which is close to the calculated value of 26 Hz due to the residual magnetic field curvature at unitarity.

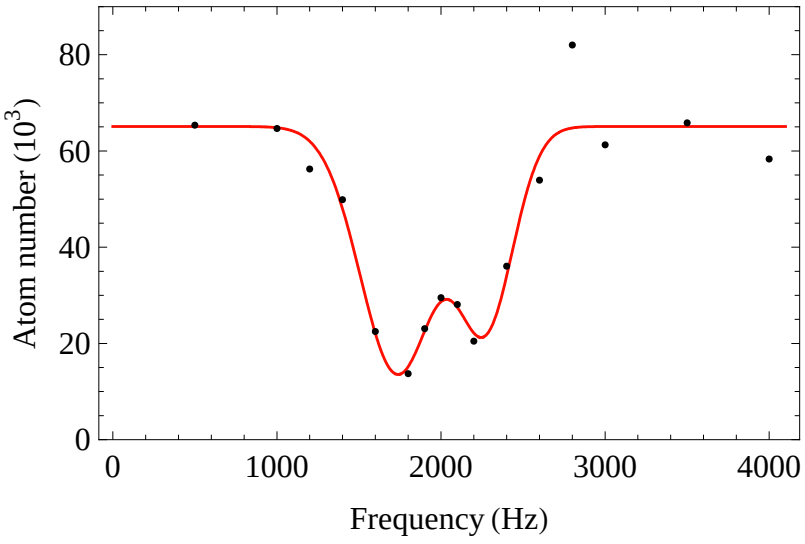

Figure 5.4: Parametric heating in the dipole trap. When the modulation frequency is twice the radial frequency, atoms are heated and lost from the trap.

Unlike the axial frequency, the radial trap frequency does not depend on the magnetic field gradient. Even at the lowest trap depth (50 mW), the radial frequency is greater than the magnetic trap frequency by a factor of 10. Experimentally, ω_r cannot be measured easily by shifting the cloud position. In order to measure the radial frequency, the trap is heated parametrically [80] and the loss of atoms from the trap is measured as function of the modulating frequency. The observed frequency for maximum trap loss is twice the actual frequency due to the harmonic confinement. Initially, the atomic sample is evaporatively cooled to a final laser power of 0.5 W and then recompressed by doubling the power to confine the atoms deeply at the bottom of the dipole trap. At this power the intensity is modulated by 3% for 1 s followed by absorption imaging after 3 ms TOF. Figure 5.4 shows the measured atom numbers versus the applied frequency. Two distinct minima are observed, at 1.73 kHz and 2.27 kHz, instead of one. This might be due to astigmatism introduced in the beam while passing through the glass wall. From eq. 5.15, for a trap at 0.5 W power, the radial frequency is calculated to be 1.1 kHz which is close to twice the observed value.

5.4 Evaporative cooling

Trapping frequency measurements are essential for knowing the phase-space density of the cloud from the relation

$$D = N \left(\frac{\hbar \bar{\omega}}{k_{\mathrm{B}} T} \right)^3, \tag{5.18}$$

where $\bar{\omega} = \left(\omega_z \omega_r^2\right)^{1/3}$ is the geometric mean of the trapping frequencies, N is the total number of atoms and T is the temperature of the cloud. For a MOT containing $\sim 10^8$ atoms at a temperature of 280 μK and for a loading efficiency of 1% into the dipole trap, the initial phase-space density is calculated to be 0.6×10^{-3}. In order to achieve degeneracy (D=1), the temperature needs to be reduced further through forced evaporation.

Evaporative cooling is a process in which the highly energy particles leave the dipole

trap so that the remaining particles rethermalise and reduce the average temperature of the sample. The transferred atomic sample in the trap has a roughly equal spin mixture of the two lowest hyperfine ground states ($|1\rangle$ and $|2\rangle$) of ^{6}Li. Although the elastic collisions between atoms with identical spins are suppressed due to the Pauli exclusion principle, the presence of two different spin states ensures that these collisions are allowed for evaporative cooling. For efficient evaporation, fast rethermalisation is required which depends on the elastic scattering rate given by [84]

$$\gamma = n\sigma\overline{v} = \frac{4\pi N m \sigma \nu^3}{k_{\rm B} T}, \tag{5.19}$$

where n is the atomic density of each state, $\overline{v}$ is the mean velocity of the atoms, N is the number of atoms in each state, $\nu = \overline{\omega}/2\pi$ is the mean trapping frequency and σ is the elastic s-wave scattering cross section of the colliding atoms in the two different hyperfine states. The scattering cross section depends on the scattering length a through the relation $\sigma = 4\pi a^2$. However, at unitarity (834 G), the scattering cross section becomes independent of the scattering length and is given by $\sigma \simeq 4\pi/k^2$, where $k = m\overline{v}/2\hbar$ is the scattering wave number, which depends only on the momentum. At the end of plain evaporation, the temperature of the cloud in the dipole trap is typically around 100 μK giving an initial collision rate as high as $\sim 1.5 \times 10^4$ s^{-1}.

To quantify the forced evaporation in time-dependent optical traps, O'Hara *et. al.* [84] derived scaling laws for particle number, phase-space density, and elastic collision rate in terms of their initial values. This model assumes that the ratio of the trap potential to the temperature is always kept constant, i.e., $\eta = U/k_B T = 10$. From these relations, given below,

$$\frac{N}{N_{\rm i}} = \left(\frac{U}{U_{\rm i}}\right)^{0.19} \tag{5.20}$$

$$\frac{D}{D_{\rm i}} = \left(\frac{U}{U_{\rm i}}\right)^{-1.3} \tag{5.21}$$

$$\frac{\gamma}{\gamma_{\rm i}} = \left(\frac{U}{U_{\rm i}}\right)^{0.69}. \tag{5.22}$$

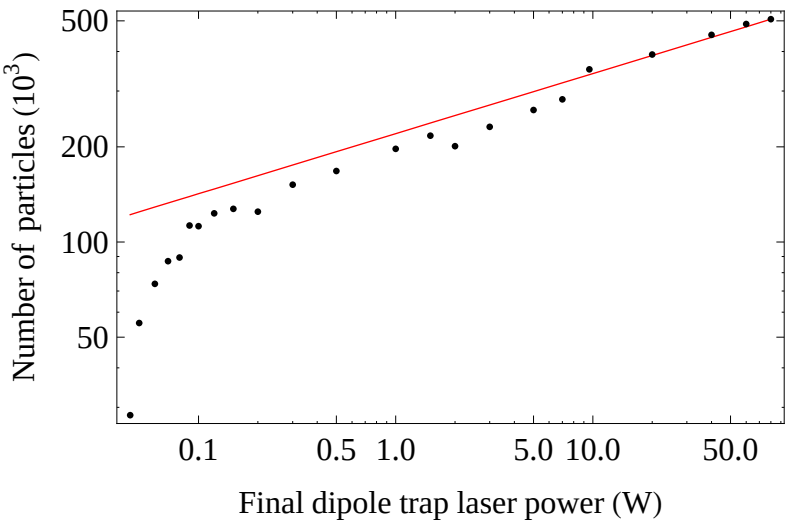

Figure 5.5: Evaporative cooling in the crossed dipole trap. The data, which is similar to that of a single dipole trap, shows efficient cooling of particles according to the scaling laws.

it can be easily calculated that to achieve a phase-space density of 1 from an initial value of 0.6×10^{-3}, the trap depth should be reduced by a factor of 200. At the end of this, the collision rate is decreased by a factor of 40 with a 65% loss in the number of particles. Because these equations are obtained without including the inelastic losses or background atom collisions and other imperfections due to the trap, the numbers above represent the best case scenario.

Figure 5.5 shows the data for evaporative cooling in our dipole trap. This data is taken from an earlier experimental set-up in a crossed dipole trap. A similar number of atoms is obtained nowadays using a single beam dipole trap and the evaporation process is similar in both the traps. The atomic sample is first evaporatively cooled at 770 G before ramping to 694 G in 100 ms for absorption imaging. It shows a decrease in atom number in the state $|1\rangle$ as the final laser power in the trap is reduced. The solid line represents the calculated scaling law prediction for a cut-off parameter of $\eta = 10$. The experimental data agrees well with the scaling law prediction until the lowest trap depth (100 mW) achievable with our laser. This shows that the evaporation is efficient even when the trap depth is reduced by a factor of 800.

5.5 Molecular BEC

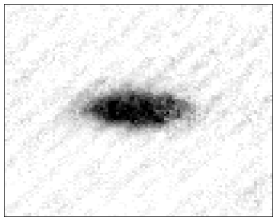

(a) 57 mW

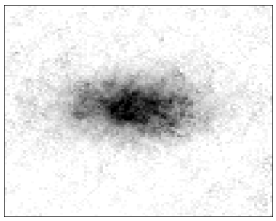

(b) 115 mW

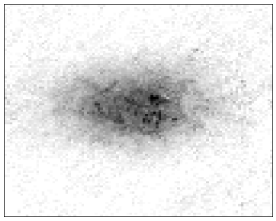

(c) 172 mW

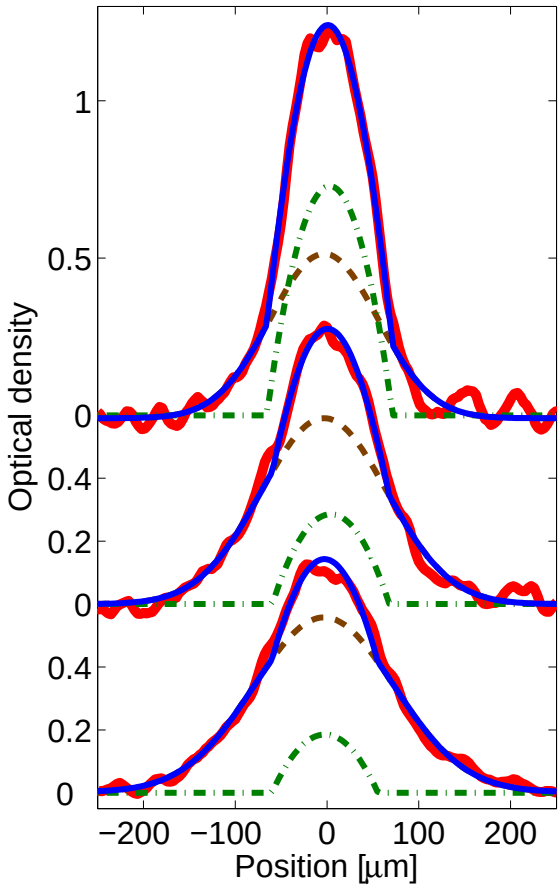

(d) Bimodal distributions of the images a, b and c

Figure 5.6: Formation of a molecular BEC: Absorption images taken at various final trap depths are shown in (a)-(c). The dashed, dash-dotted, solid (blue) lines in (d) are fits to a Gaussian, Thomas-Fermi and combined profiles, respectively.

When the evaporation is performed on the BEC side of the Feshbach resonance, stable molecules are formed via three-body recombination when the temperature of the atoms becomes lower than the binding energy of the molecules. At this stage, both atoms and molecules exist in thermodynamic equilibrium and the measured temperature no longer represents the true value due to the two-components in the cloud. Further evaporation to lower temperatures favours the formation of molecules. Because these molecules are composite bosons, whose inelastic loss rate is low, they can undergo efficient evaporative cooling to reach Bose-Einstein condensation at a

sufficiently high phase-space density.

Figure 5.6 shows the formation of a molecular BEC monitored by absorption images. All images are taken at 694 G after evaporation at 770 G to a final trap depth of (a) 57 mW, (b) 115 mW and (c) 172 mW. In Fig. 5.6d integrated cross sections of these images along the weakest trapping direction are shown. The dashed, dash-dotted and solid (blue) lines are fits to a Gaussian, Thomas-Fermi and combined profiles, respectively. An increase of 10% to 50% in condensate fraction is shown in these profiles. However, nowadays at a final trap depth of 50 mW, $\sim 150\,000$ molecules are observed and a condensate fraction of up to 90% is obtained.

5.6 Degenerate Fermi gas

When evaporative cooling is performed on the BCS side of the Feshbach resonance, its efficiency is suppressed due to Pauli blocking. In other words, because the evaporation process depends on scattering to available low-lying energy states, the Pauli exclusion principle forbids collisions into occupied states, which stagnates the evaporation process. However, it has been shown [85] that at temperatures $T \ll T_F$, the rethermalisation rate is faster than evaporation. In the case of a weakly interacting Fermi gas, a BCS-like state is favoured involving Cooper pairs.

In our experiments, a degenerate Fermi gas is typically produced by taking advantage of the fact that the crossover from the BEC to BCS side is isentropic [23]. The atomic sample is first evaporatively cooled at unitarity and then the magnetic field is adiabatically ramped to the desired value on the BCS side . Figure 5.7 shows a one-dimensional profile of the observed Fermi gas, after 4 ms time of flight, obtained by integrating the absorption image along the weak trapping axis. At this lowest trap depth (60 mW) the trapping frequencies are ω_{axial}=150 Hz and ω_{radial}=1.63 kHz. Because fermions follow a Fermi-Dirac distribution, the data fits very well to this profile. For comparison a Maxwell-Boltzmann (classical gas) distribution is plotted for

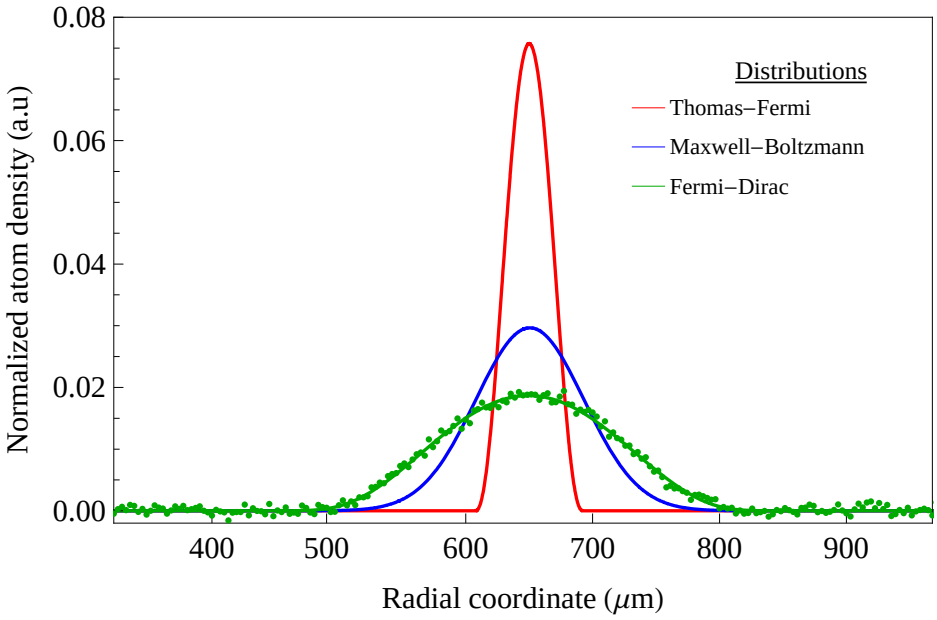

Figure 5.7: 1D Poly-logarithmic (Fermi-Dirac) fit to the data (TOF = 4 ms). For comparison a Maxwell-Boltzmann (classical gas) distribution is plotted for a gas at the same temperature (T/T_{F}=0.06). A Thomas-Fermi (bosons) distribution is also shown for the same Fermi radius.

a gas at the same temperature (T/T_{F}=0.06). A Thomas-Fermi (bosons) distribution is also shown for the same Fermi radius. The peak of the Fermi-Dirac fit has a flat top whereas it is sharp for the classical gas. This is due to the emergence of Fermi pressure at trap centre where the density is high.

5.7 Summary

This chapter described the procedure followed in our experiments to achieve highly degenerate quantum gases. The way how the atoms are trapped and cooled using dissipative and conservative forces due to the laser field is briefly discussed. Additionally, technical details about measuring the dipole trap frequencies and the mechanism behind evaporative cooling is explained. Producing degenerate quantum gases is the starting point for performing Bragg spectroscopy across the BEC-BCS crossover. The results of the Bragg spectroscopy experiments are discussed in Chapters 7 and 8 after presenting a theoretical background in Chapter-6.

Chapter 6

Bragg scattering - Theory

6.1 Introduction

In this chapter the theoretical background for the Bragg scattering experiments is presented. The first objective is to introduce pair correlation functions and to show how they are related to the static structure factor via a Fourier transform. The second objective is to obtain a relation between the static structure factor and the measured Bragg scattering signal, which is the centre-of-mass (COM) displacement of the cloud. Although these two relations are frequently referred to in many papers [54, 55], their explicit derivation is not found in the literature. A brief introduction to the static structure factors (sec. 6.3) and correlation functions (sec. 6.4) is given here. Also, a method for probing the pair correlations in a strongly interacting fermionic system via a Bragg scattering experiment is discussed in the last section (sec. 6.5). First, the principles of Bragg scattering are schematically explained in the following section.

6.2 Bragg scattering

In an inelastic scattering experiment, such as Bragg scattering, the response of a many-body system to a weak probe provides information about the internal properties of the system [53, 54, 55]. This response function typically reveals the correlations between particles in the system. For example, to study elementary excitations of liquid ^{4}He, slow-moving neutrons were used as a probe and the response of the system was measured as a function of the scattering angle of the neutrons [56, 57, 58]. On the other hand, Bragg scattering of X-rays from a solid state crystal provides information about the structure of the crystal lattice [86].

In atom optics, a coherent source of matter waves can be manipulated in the same way as optical waves. In contrast to the Bragg scattering of X-rays from a crystal lattice, the roles of the light and matter are reversed and a matter wave can be diffracted from a periodic optical potential. One key example is Bragg scattering of a BEC from a moving optical lattice [87]. Here, the dependence on the scattering angle becomes a dependence on the relative velocity between the lattice and atoms.

6.2.1 Principle

Bragg scattering is a coherent process in which momentum is transferred to a particle via paired stimulated absorption and emission of photons. Consider two counter-propagating laser beams with frequencies $\omega+\delta$ and ω, far detuned Δ from the resonant atomic frequency, interacting with a particle. The particle is first excited from the ground state to a virtual excited state by absorbing a high frequency photon $\omega + \delta$, followed by stimulated emission of a low frequency photon ω (see Fig. 6.1). Due to momentum conservation, the net momentum difference between these two photons causes the particle to scatter with a velocity $v_{recoil} = \frac{q}{m}$, where the two-photon recoil momentum $q = 2\hbar k$, $k = 2\pi/\lambda$ is the wavevector of the laser of wavelength λ and m is the mass of the scattered particle. Conservation of energy leads to the Bragg resonance

condition when the energy associated with this recoil momentum ($E = q^2/2m$) is equal to the energy associated with the Bragg frequency ($E = \hbar\delta$) of the laser beams, thus

$$\delta = \frac{2\hbar k^2}{m}. \tag{6.1}$$

The detuning Δ of the laser from the atomic resonance should be small enough to give a reasonable excitation probability but large enough to avoid directly populating the excited state.

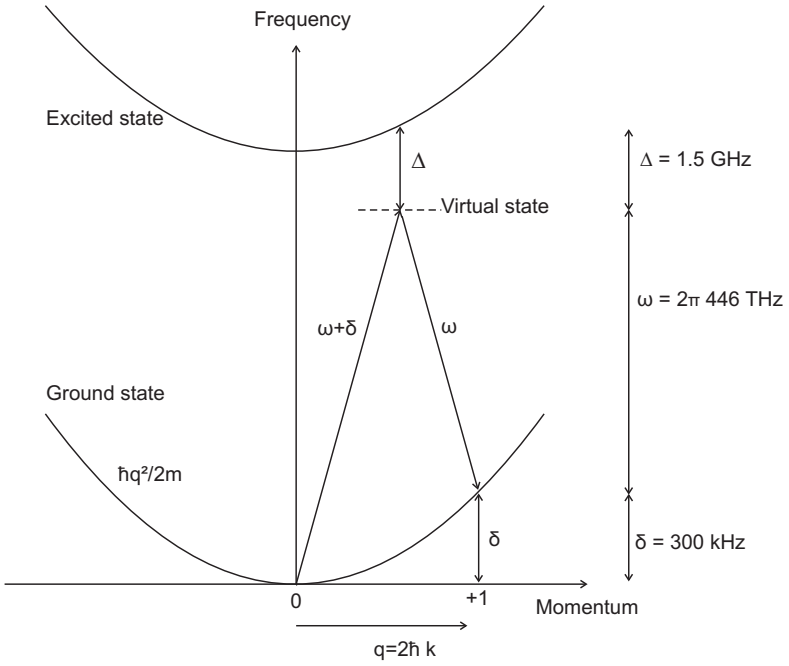

Figure 6.1: Energy level diagram for Bragg spectroscopy (not to scale). The vertical line on the right gives the approximate range of frequencies involved in the case of ^{6}Li atom for our experimental conditions.

Phonon regime: When the recoil velocity $v_{rec} = q/m$ due to the Bragg pulse is smaller than the speed of sound c_s in the gas, only low lying elementary excitations are excited. These excitations give a phonon-like spectrum being linearly proportional to q as given below

$$\hbar\delta \simeq \hbar q c_s, \tag{6.2}$$

where the relation between the interaction energy and the speed of sound is given as

$\mu = mc_s^2$. This modifies the low energy region of Fig. 6.1 to linear.

Free particle regime: When the recoil velocity $v_{rec} = q/m$ due to the Bragg pulse is larger than the speed of sound c_s in the gas, the excitations resemble a free particle spectrum as given below

$$\hbar\delta \simeq \frac{\hbar^2 q^2}{2m}. \tag{6.3}$$

The spectrum in this regime is parabolic, and in the case of an atomic BEC there is an additional offset of μ due to the mean field shift [88]. For large q values ($q > k_{\mathrm{F}}$, where k_{F} is the Fermi wave-vector), the excitation spectrum of fermions also approaches that of the free particle excitations [30].

Our experimental conditions: The atomic resonance wavelength for a ^{6}Li atom is $\lambda = 671$ nm; therefore the recoil velocity $v_{rec} = 19.8$ cm/s. The velocity of sound across the BEC-BCS crossover was first measured by J. Joseph *et al.* [89] in terms of the Fermi velocity v_{F}

$$v_{\mathrm{F}}^2 = \frac{2}{m_a}\hbar\left(\omega_x\omega_y\omega_z\right)^{\frac{1}{3}}(6N)^{\frac{1}{3}}, \tag{6.4}$$

where m_a is the mass of the ^{6}Li atom, ω_i are the trapping frequencies in the various directions and N is the total number of atoms in one spin state. Substituting our experimental values for the trapping frequencies, $\omega_x = \omega_y = 2\pi\times$ 320 Hz and $\omega_z = 2\pi\times$ 24 Hz, and the atomic number N =130,000, the Fermi energy is calculated to be $E_{\mathrm{F}}/k_{\mathrm{B}} = 600$ nK. For the experimental magnetic field range 750 G to 1000 G, the $1/k_{\mathrm{F}}a$ value varies from +1.4 on the BEC side to -1 on the BCS side. For this range, the measured c_s varies from $0.25v_{\mathrm{F}}$ to $0.45v_{\mathrm{F}}$ according to reference [89]. Therefore, the calculated value for $v_{\mathrm{F}} = 0.3$ cm/s gives a sound velocity $c_s = 0.10$ cm/s on the BEC side and $c_s = 0.16$ cm/s on the BCS side.

Thus, for our experimental conditions, the recoil velocity is always much greater than the speed of sound ($v_{rec} >> c_s$) across the BEC-BCS crossover confirming that all our experiments are performed well into the free particle regime.

6.3 The structure factors

As explained in the previous section, for Bragg scattering in ultracold gases, the strength of the scattering depends on the frequency difference δ between the beams and the momentum q transferred by the beams [87, 88]. For short interaction times (pulse duration), the response of the cloud to the Bragg pulse indirectly [90] measures the dynamic structure factor $S(q, \delta)$ which characterizes the dynamics of the many-body quantum system. The static structure factor $S(q)$ is obtained from the integral of $S(q, \delta)$ over all frequencies and gives the effective line strength of the scattering for a given momentum q. These quantities have been measured in an atomic BECs and have proven valuable in understanding the density correlations [61] and the elementary excitations [60] of the condensate. In the following subsections, these structure factors are defined and their relation to the density correlation functions are presented.

6.3.1 The dynamic and static structure factors

Following reference [91], an expression for the dynamic and static structure factors in terms of the density operators is presented. Consider an incoming external probe particle interacting with a system of N-particles. In first quantized form, the interaction Hamiltonian is written as the sum of all the interactions U between the probe and the particles of the system.

$$\hat{H}_{int} = \sum_{i=1}^{N} U(R - \hat{r}_i), \tag{6.5}$$

where R is the probe position and r_i is the particle position. It is more convenient to write $\hat{H}_{int}$ in the frame-work of second quantization by Fourier analyzing the above equation

$$\hat{H}_{int} = \frac{1}{V} \sum_{K} U(K) e^{-iK.R} \hat{\rho}(K), \tag{6.6}$$

where V is the volume of the system, $\hat{\rho}(K)$ is the Fourier transform of the one-body density $\hat{\rho}_I$ and $U(K)$ is the Fourier transform of the interaction potential $U(R - r)$ as

given by [1]

$$\begin{aligned}\hat{\rho}(K) &= \int dr e^{iK.r}\hat{\rho}_I(r) \\ U(K) &= \int dr U(R-r)e^{iK.(R-r)}.\end{aligned}$$

Consider a Bragg scattering experiment, where photons with momentum $p_i = \hbar k_1$ and energy ε_i scatter from a sample and emerge with momentum $p_f = \hbar k_2$ and energy ε_f. During this scattering process, the N-particle system changes from an initial state ϕ_i with energy E_i to a final state ϕ_f with energy E_f. In order to evaluate the transition rate for this process, the interaction matrix element is expressed as

$$\begin{aligned}\langle k_2, \phi_f|\hat{H}_{int}|k_1, \phi_i\rangle &= \langle k_2, \phi_f|\frac{1}{V}\sum_K U(K)e^{-iK.R}\hat{\rho}(K)|k_1, \phi_i\rangle \\ &= \sum_K U(K)\langle\phi_f|\hat{\rho}(K)|\phi_i\rangle\delta(K + k_2 - k_1) \\ &= U(q)\langle\phi_f|\hat{\rho}(q)|\phi_i\rangle,\end{aligned}$$

where $q = k_1 - k_2$ is the momentum imparted to the system by the probe and $U(q)$ is the amplitude of the interaction potential. The transition rate between the initial and final state is obtained using Fermi's golden rule within the Born approximation

$$W_{i\to f} = \frac{2\pi}{\hbar}|U(q)|^2|\langle\phi_f|\hat{\rho}(q)|\phi_i\rangle|^2\delta(\hbar\delta - E_f + E_i), \tag{6.7}$$

where $\hbar\delta = \varepsilon_i - \varepsilon_f$ is the energy lost by the scattered photons. To account for the fact that the final state $|\phi_f\rangle$ may belong to a continuous spectrum, a sum is taken over all allowed final states [92]. Thus, the transition rate from the initial state $|\phi_i\rangle$ to the final state of the continuum is given by

[1] Here and in the following integrals dr represents the volume element, i.e., d^3r, unless otherwise specified.

$$
\begin{aligned}
W_{i\to f} &= \frac{2\pi}{\hbar}|U(q)|^2 \sum_f |\langle\phi_f|\hat{\rho}(q)|\phi_i\rangle|^2 \delta(\hbar\delta - E_f + E_i) \\
&= \frac{2\pi}{\hbar}|U(q)|^2 S(q,\delta), \qquad (6.8)
\end{aligned}
$$

where in the last line the dynamic structure factor (DSF) $S(q,\delta)$ has been introduced. As can be seen, the DSF quantifies how the energy eigenstates of the many-body system are coupled by fluctuations of the momentum density:

$$
S(q,\delta) = \sum_f |\langle\phi_f|\hat{\rho}(q)|\phi_i\rangle|^2 \delta(\hbar\delta - E_f + E_i). \qquad (6.9)
$$

The static structure factor (SSF) $S(q)$ is defined as the total scattered intensity for a given momentum transfer q. Using this definition, it is shown below that $S(q)$ represents the density-density fluctuations of the initial state in momentum space

$$
\begin{aligned}
NS(q) &= \int d\delta \; S(q,\delta) \qquad (6.10) \\
&= \sum_f |\langle\phi_f|\hat{\rho}(q)|\phi_i\rangle|^2 \\
&= \sum_f \langle\phi_i|\hat{\rho}^\dagger(q)|\phi_f\rangle\langle\phi_f|\hat{\rho}(q)|\phi_i\rangle \\
&= \langle\phi_i|\hat{\rho}^\dagger(q)\hat{\rho}(q)|\phi_i\rangle, \qquad (6.11)
\end{aligned}
$$

where the identity operator is resolved in deriving the last equality.

In summary, $S(q,\delta)$ gives a measure of the spectrum of the elementary excitations, being directly proportional to the square of the excitation matrix element, and $S(q)$ gives information about the momentum density-density correlations in the initial state.

6.3.2 Impulse approximation

The derivations presented so far apply to a system at zero temperature. In order to include finite temperature effects, a statistical description of the states should be taken into account. Then the dynamic structure factor becomes [53]

$$S(q,\delta) = \frac{1}{\mathfrak{Z}} \sum_{f\ i} e^{-\beta E_f} |\langle \phi_f | \hat{\rho}(q) | \phi_i \rangle|^2 \delta(\hbar\delta - E_f + E_i), \tag{6.12}$$

where $|\phi_n\rangle$ and E_n are the eigenstates and eigenvalues of the total Hamiltonian of the system respectively, $\mathfrak{Z} = \sum_n e^{-\beta E_n}$ is the partition function and $\beta = 1/k_{\mathrm{B}}T$. For an ideal gas, the above equation can be written in terms of the particle distribution functions (n_p) at temperature T [93], so that

$$S(q,\delta) = \sum_p n_p[1 \pm n_{p+q}]\ \delta\left(\hbar\delta - \frac{(p+q)^2}{2m} + \frac{p^2}{2m}\right), \tag{6.13}$$

where p and $p+q$ are the initial and final momentum of the particle, respectively. The plus sign holds for bosons and the negative sign holds for fermions. Thus, in the case of bosons, the scattering process is enhanced while it is suppressed for fermions due to the Pauli exclusion principle. For a large momentum transfer, the n_{p+q} term becomes negligible as there is negligible occupation of the final state and the summation can be replaced by an integral:

$$S_{\mathrm{IA}}(q,\delta) = \int dp\ n(p)\delta\left(\hbar\delta - \frac{(p+q)^2}{2m} + \frac{p^2}{2m}\right), \tag{6.14}$$

where $n(p)$ is the momentum distribution of the system. This is known as the impulse approximation (IA) [54], which shows that the measurement of the dynamic structure factor can also provide information about the initial momentum distribution of the system [94]. In fact, this approximation can be used to determine the zero temperature behaviour of an ideal Bose gas and an ideal Fermi gas to compare with the experimentally measured dynamic structure factor (see sec. 8.4).

6.4 Dependence of structure factors on the correlation functions

In order to derive a relation between the structure factor and the correlation function, the properties of the density fluctuations and the correlation functions are stated first. The derivation follows the discussion presented by C. Cohen-Tannoudji *et al.* in ref. [91] and by Fetter and Walecka in ref. [93].

6.4.1 Brief review of the correlation functions

A uniform system of N-particles can be described in second quantized notation, where the field operators are defined as

$$\begin{aligned} \hat{\psi}(r) &= \sum_i \psi_i(r)\hat{a}_i \\ \hat{\psi}^\dagger(r) &= \sum_i \psi_i^*(r)\hat{a}_i^\dagger. \end{aligned}$$

Here, $\hat{a}_i^\dagger$ and $\hat{a}_i$ are the creation and annihilation operators and $\psi_i(r) = \langle r|\psi\rangle$ is the projection of the i^{th} single state particle onto $|r\rangle$. For bosons, the field operators commute

$$[\hat{\psi}(r), \hat{\psi}^\dagger(r')] = \delta(r - r') \tag{6.15}$$

$$[\hat{\psi}(r), \hat{\psi}(r')] = 0, \tag{6.16}$$

while for fermions the field operators anti-commute

$$\{\hat{\psi}(r), \hat{\psi}^\dagger(r')\} = \delta(r - r') \tag{6.17}$$

$$\{\hat{\psi}(r), \hat{\psi}(r')\} = 0. \tag{6.18}$$

In the $|r\rangle$ basis, the one-body $\hat{\rho}_I$ and two-body $\hat{\rho}_{II}$ density operators are defined as

$$\begin{aligned}\hat{\rho}_I(r) &= \hat{\psi}^\dagger(r)\hat{\psi}(r) \\ \hat{\rho}_{II}(r,r') &= \hat{\psi}^\dagger(r)\hat{\psi}^\dagger(r')\hat{\psi}(r')\hat{\psi}(r).\end{aligned}$$

The correlation functions are defined as the expectation values of products of the field operators. For example, the first-order correlation function is given as

$$G^{(1)}(r,r) = \langle\hat{\psi}^\dagger(r)\hat{\psi}(r)\rangle = \langle\hat{\rho}_I(r)\rangle = n \tag{6.19}$$

which gives the probability of finding a particle at a position r, where $n = N/V$ is the density of the system [91]. Similarly, the second-order correlation function is defined as

$$G^{(2)}(r,r') = \langle\hat{\psi}^\dagger(r)\hat{\psi}^\dagger(r')\hat{\psi}(r')\hat{\psi}(r)\rangle = \langle\hat{\rho}_{II}(r,r')\rangle \tag{6.20}$$

which gives the probability of finding a particle at position r given another particle at r'. $G^{(2)}(r,r')$ can be written in terms of the normalized second-order correlation function:

$$\begin{aligned}g^{(2)}(r,r') &= \frac{G^{(2)}(r,r')}{G^{(1)}(r,r)G^{(1)}(r',r')} \\ &= \frac{G^{(2)}(r,r')}{\langle\hat{\psi}^\dagger(r)\hat{\psi}(r)\rangle\langle\hat{\psi}^\dagger(r')\hat{\psi}(r')\rangle} \\ &= \frac{G^{(2)}(r,r')}{n^2},\end{aligned}$$

or

$$\begin{aligned}G^{(2)}(r,r') &= \langle\phi_i|\hat{\psi}^\dagger(r)\hat{\psi}^\dagger(r')\hat{\psi}(r')\hat{\psi}(r)|\phi_i\rangle \\ &= g^{(2)}(r,r')n^2.\end{aligned} \tag{6.21}$$

6.4.2 Structure factors in terms of the correlation functions

In the case of inelastic scattering, where the energy transferred to the system is positive, $\hat{\rho}(q)$ in eq. 6.11 can be described in terms of the fluctuations of the particle density $\delta\hat{\rho}(q)$ about its average value ρ_o [93], i.e.,

$$\begin{aligned} \delta\hat{\rho}(q) &= \hat{\rho}(q) - \hat{\rho_o}(q) && (6.22) \\ &= \hat{\rho}(q) - \langle\phi_i|\hat{\rho}(q)|\phi_i\rangle. && (6.23) \end{aligned}$$

Therefore, from the definition of the SSF, eq. 6.11 can be written as

$$NS(q) = \langle\phi_i|\delta\hat{\rho}^\dagger(q)\delta\hat{\rho}(q)|\phi_i\rangle. \tag{6.24}$$

Dropping the q dependence for the time being, consider the following product

$$\begin{aligned} \delta\hat{\rho}^\dagger\ \delta\hat{\rho} &= \left(\hat{\rho}^\dagger - \hat{\rho_o}^\dagger\right)\left(\hat{\rho} - \hat{\rho_o}\right) \\ &= \left(\hat{\rho}^\dagger - \langle\phi_i|\hat{\rho}^\dagger|\phi_i\rangle\right)\left(\hat{\rho} - \langle\phi_i|\hat{\rho}|\phi_i\rangle\right) \\ &= \hat{\rho}^\dagger\hat{\rho} - \hat{\rho}^\dagger\langle\phi_i|\hat{\rho}|\phi_i\rangle - \langle\phi_i|\hat{\rho}^\dagger|\phi_i\rangle\hat{\rho} + \langle\phi_i|\hat{\rho}^\dagger|\phi_i\rangle\langle\phi_i|\hat{\rho}|\phi_i\rangle. \end{aligned}$$

Therefore, the expectation value for the product $\delta\hat{\rho}^\dagger\ \delta\hat{\rho}$ follows

$$\begin{aligned} \langle\phi_i|\delta\hat{\rho}^\dagger\ \delta\hat{\rho}|\phi_i\rangle &= \langle\phi_i|\hat{\rho}^\dagger\hat{\rho}|\phi_i\rangle - \langle\phi_i|\hat{\rho}^\dagger|\phi_i\rangle\langle\phi_i|\hat{\rho}|\phi_i\rangle - \langle\phi_i|\hat{\rho}^\dagger|\phi_i\rangle\langle\phi_i|\hat{\rho}|\phi_i\rangle \\ &\quad + \langle\phi_i|\hat{\rho}^\dagger|\phi_i\rangle\langle\phi_i|\hat{\rho}|\phi_i\rangle\langle\phi_i|\phi_i\rangle. \end{aligned}$$

Using the completeness condition $\langle\phi_i|\phi_i\rangle = 1$ in the last term

$$\begin{aligned} \langle\phi_i|\delta\hat{\rho}^\dagger\ \delta\hat{\rho}|\phi_i\rangle &= \langle\phi_i|\hat{\rho}^\dagger\hat{\rho}|\phi_i\rangle - \langle\phi_i|\hat{\rho}^\dagger|\phi_i\rangle\langle\phi_i|\hat{\rho}|\phi_i\rangle \\ &= \langle\phi_i|\hat{\rho}^\dagger\hat{\rho}|\phi_i\rangle - |\langle\phi_i|\hat{\rho}|\phi_i\rangle|^2. && (6.25) \end{aligned}$$

Thus, using eq. 6.25 in eq. 6.24, the equation for the SSF becomes

$$NS(q) = \langle\phi_i|\hat{\rho}^\dagger(q)\hat{\rho}(q)|\phi_i\rangle - |\langle\phi_i|\hat{\rho}(q)|\phi_i\rangle|^2. \tag{6.26}$$

Recalling that $\hat{\rho}(q)$ is the Fourier transform of the one-body spatial density operator

$$\begin{aligned}\hat{\rho}(q) &= \int dr e^{iq.r}\hat{\rho_I}(r) \\ &= \int dr e^{iq.r}\hat{\psi}^\dagger(r)\hat{\psi}(r)\end{aligned}$$

the first term in eq. 6.26 can be written as

$$\begin{aligned}\langle\phi_i|\hat{\rho}^\dagger(q)\hat{\rho}(q)|\phi_i\rangle &= \langle\phi_i|\left(\int dr' e^{-iq.r'}\hat{\rho_I}^\dagger(r')\int dr e^{iq.r}\hat{\rho_I}(r)\right)|\phi_i\rangle \\ &= \int e^{-iq.r'}\langle\phi_i|\hat{\psi}^\dagger(r')\hat{\psi}(r')\hat{\psi}^\dagger(r)\hat{\psi}(r)|\phi_i\rangle e^{iq.r}dr'dr.\end{aligned}$$

Using the first commutation (anti-commutation) relation eq. 6.15 (eq. 6.17) for bosons (fermions) between the field operators,

$$\begin{aligned}\langle\phi_i|\hat{\rho}^\dagger(q)\hat{\rho}(q)|\phi_i\rangle &= \int e^{-iq.r'}\langle\phi_i|\hat{\psi}^\dagger(r')\left[\delta(r-r') \pm \hat{\psi}^\dagger(r)\hat{\psi}(r')\right]\hat{\psi}(r)|\phi_i\rangle e^{iq.r}dr'dr \\ &= \int e^{-iq.r'}\langle\phi_i|\hat{\psi}^\dagger(r')\delta(r-r')\hat{\psi}(r)|\phi_i\rangle e^{iq.r}dr'dr \\ &\pm \int e^{-iq.r'}\langle\phi_i|\hat{\psi}^\dagger(r')\hat{\psi}^\dagger(r)\hat{\psi}(r')\hat{\psi}(r)|\phi_i\rangle e^{iq.r}dr'dr,\end{aligned}$$

where the positive sign holds for bosons and the negative sign for fermions. Resolving the delta function and using the second commutation (anti-commutation) relation eq. 6.16 (eq. 6.18) for bosons (fermions) between the field operators

$$\begin{aligned}
\langle\phi_i|\hat{\rho}^\dagger(q)\hat{\rho}(q)|\phi_i\rangle &= V\langle\phi_i|\hat{\psi}^\dagger(r)\hat{\psi}(r)|\phi_i\rangle \\
&\quad \pm \int e^{-iq.r'}\langle\phi_i|\left(\pm\hat{\psi}^\dagger(r)\hat{\psi}^\dagger(r')\right)\hat{\psi}(r')\hat{\psi}(r)|\phi_i\rangle e^{iq.r}dr'dr \\
&= n\,V + \int e^{-iq.r'}\langle\phi_i|\hat{\psi}^\dagger(r)\hat{\psi}^\dagger(r')\hat{\psi}(r')\hat{\psi}(r)|\phi_i\rangle e^{iq.r}dr'dr \\
&= N + n^2\int e^{-iq.r'}g^{(2)}(r,r')e^{iq.r}dr'dr, \qquad (6.27)
\end{aligned}$$

where the normalization condition $\langle\phi_i|\hat{\psi}^\dagger(r)\hat{\psi}(r)|\phi_i\rangle = n$ for the field operators and the definition (eq. 6.21) of the normalized second-order correlation function $g^{(2)}(r,r')$ is used. Thus, the final result is the same for both bosons and fermions. Now, the second term in eq. 6.26 can be written as

$$\begin{aligned}
|\langle\phi_i|\hat{\rho}(q)|\phi_i\rangle|^2 &= \langle\phi_i|\hat{\rho}^\dagger(q)|\phi_i\rangle\langle\phi_i|\hat{\rho}(q)|\phi_i\rangle \\
&= \langle\phi_i|\left(\int dr'e^{-iq.r'}\hat{\rho_I}^\dagger(r')\right)|\phi_i\rangle\langle\phi_i|\left(\int dre^{iq.r}\hat{\rho}_I(r)\right)|\phi_i\rangle \\
&= \int e^{-iq.r'}\langle\phi_i|\hat{\psi}^\dagger(r')\hat{\psi}(r')|\phi_i\rangle\langle\phi_i|\hat{\psi}^\dagger(r)\hat{\psi}(r)|\phi_i\rangle e^{iq.r}dr'dr \\
&= n^2\int e^{-iq.r'}e^{iq.r}dr'dr. \qquad (6.28)
\end{aligned}$$

Finally, using equations 6.27 and 6.28, eq.6.26 can be written as

$$\begin{aligned}
NS(q) &= N + n^2\int e^{-iq.r'}\left[g^{(2)}(r,r')-1\right]e^{iq.r}dr'dr \\
S(q) &= 1 + \frac{N}{V^2}\int e^{-iq.r'}\left[g^{(2)}(r,r')-1\right]e^{iq.r}dr'dr.
\end{aligned}$$

In the case of a uniform gas, the two-body correlation function depends only on the relative distance between the particles. Thus, $g^{(2)}(r, r') \equiv g^{(2)}(|r - r'|) = g(z)$, where $g(z)$ is the conditional probability to find two atoms separated by a distance z, and the SSF becomes

$$\begin{aligned} S(q) &= 1 + \frac{N}{V^2} V \int e^{iq.z} \left[g(z) - 1\right] dz \\ S(q) &= 1 + n \int e^{iq.z} \left[g(z) - 1\right] dz. \end{aligned} \tag{6.29}$$

This shows the explicit dependence of the static structure factor $S(q)$ on the two-body correlation function $g(z)$.

6.4.3 The two-body pair correlation function

We now consider a two-component Fermi gas with an equal number $N/2$ of atoms in the two spin hyperfine states (spin up $\sigma = \uparrow$ and spin down $\sigma = \downarrow$). The spin-resolved pair correlation function is defined as

$$g^{(2)}_{\sigma\sigma'}(r, r') = \frac{\langle \hat{\psi}^\dagger_\sigma(r) \hat{\psi}^\dagger_{\sigma'}(r') \hat{\psi}_{\sigma'}(r') \hat{\psi}_\sigma(r) \rangle}{n_\sigma(r) n_{\sigma'}(r')}, \tag{6.30}$$

which gives the probability of simultaneously finding a fermion at a position r with spin σ and another at r' with spin σ'. For a uniform gas, as mentioned above, $g^{(2)}_{\sigma\sigma'}(r, r') = g^{(2)}_{\sigma\sigma'}(z)$ and the two-body pair correlation function can be written as an average of the contributions from the same spins and the opposite spins as shown below

$$g(z) = \frac{[g_{\uparrow\uparrow}(z) + g_{\uparrow\downarrow}(z)]}{2}.$$

Note that we have assumed that the gas consists of an equal number of atoms in the two spin states, so $g_{\uparrow\uparrow} = g_{\downarrow\downarrow}$ and $g_{\uparrow\downarrow} = g_{\downarrow\uparrow}$. Now one can write the static structure

factors explicitly depending on the pair correlation functions [51] as

$$\begin{aligned} S_{\uparrow\uparrow}(q) &= 1 + \frac{n}{2}\int dz[g_{\uparrow\uparrow}(z) - 1]e^{iq.z} \\ S_{\uparrow\downarrow}(q) &= \frac{n}{2}\int dz[g_{\uparrow\downarrow}(z) - 1]e^{iq.z} \end{aligned}$$

and the total static structure factor can be written as

$$S(q) = S_{\uparrow\uparrow}(q) + S_{\uparrow\downarrow}(q).$$

Small q limit: In the limit of small momentum transfer ($q < k_F$), the static structure factor $S(q)$ depends linearly on q due to long-range correlations [53]. Therefore, as a consequence of the Pauli exclusion principle $S(q \to 0) \to 0$, implying the suppression of low energy excitations.

Large q limit: In the limit of large momentum transfer ($q > k_F$), the auto-correlations among identical spin particles dominate [51] leading to $S_{\uparrow\uparrow}(q) \to 1$. Therefore, the final SSF becomes

$$S(q) = 1 + S_{\uparrow\downarrow}(q). \tag{6.31}$$

In the case of a non-interacting Fermi gas on the BCS side, where there is no correlation between the particles of opposite spin, $S_{\uparrow\downarrow}(q) = 0$, such that $S(q) = 1$. However, in the case of a strongly interacting Fermi gas at unitarity, $S_{\uparrow\downarrow}(q)$ is non-zero but less than one. However, on the BEC side, for distances z comparable to the size a_{M} of the molecules, there is a strong correlation between atoms with opposite spin within the same molecule $S_{\uparrow\downarrow}(q) = 1$, such that $S(q) = 2$. Thus, to probe these two-body pair correlations, the Bragg experiments mentioned in this thesis are performed in the high q limit where $q \backsimeq 5k_F$.

6.5 Measuring the static structure factor

In our Bragg scattering experiments, two counter-propagating laser beams with frequency difference δ are shone onto a degenerate gas for a time τ_B and the response of the gas is measured. The momentum P_z imparted to the gas is quantified by the centre-of-mass (COM) displacement $X(q,\delta)$ of the entire gas cloud along the direction of the Bragg pulse (see sec. 7.2). From this measurement, the static structure factor can be deduced as explained below.

The periodic potential created by the two counter-propagating Bragg beams travelling along the z-direction is given as

$$\begin{aligned} V_{Bragg} &= f(t)\hbar\Omega_R \cos(qz - \delta t), \qquad \text{where} \\ f(t) &= 1 \qquad \text{for } \mid t \mid < \frac{\tau_B}{2} \\ &= 0 \qquad \text{otherwise.} \end{aligned} \tag{6.32}$$

Here Ω_R is the two-photon Rabi frequency. The interaction Hamiltonian due to this potential can be written as

$$\hat{H}_{int} = \frac{\hbar\Omega_R}{2}\left(\hat{\rho}^\dagger(q)e^{-i\delta t} + \hat{\rho}^\dagger(-q)e^{i\delta t}\right), \tag{6.33}$$

where $\hat{\rho}^\dagger(-q) = \sum_{j=1}^{N} e^{iq.r_j}$ is the density creation operator. The total Hamiltonian of a trapped interacting system of N-particles with the above periodic perturbation is given by

$$\hat{H}_{tot} = \sum_{i=1}^{N}\frac{p_i^2}{2m} + \sum_{i=1}^{N} V_{ext}(r_i) + g\sum_{i<j}\delta(r_i - r_j) + \hat{H}_{int}, \tag{6.34}$$

where $g = 4\pi\hbar^2 a/m$ defines the strength of the interaction between the particles, m is the mass of the scattered particle and V_{ext} is the harmonic confinement produced by the trap potential. Brunello *et al.* [55] have shown that for a such a system the rate of momentum transfer to the gas is related to the dynamic structure factor according to

the relation

$$\frac{dP_z(t)}{dt} = -m\omega_z^2 Z + \frac{\hbar q \Omega_R^2}{2} \int d\delta' \, [\, S(q,\delta') - S(-q,-\delta') \,] \, \frac{\sin[\, (\delta - \delta')t \,]}{(\delta - \delta')}. \qquad (6.35)$$

Since we are interested in the dynamics only on a timescale much shorter than the inverse trap frequencies, the first term can be ignored, while the second term in the integral, $S(-q,-\delta')$, can be ignored under our experimental conditions $q > k_{\rm F}$ due to the principle of detailed balancing [53], which states that the initial population in the states we are scattering into is negligible,

$$\begin{aligned} S(-q,-\delta') &= e^{-\beta\hbar\delta} \, S(q,\delta') \\ &= e^{-\frac{\hbar\delta}{k_{\rm B}T}} \, S(q,\delta') \\ &= e^{-\frac{\hbar^2 q^2}{2mk_{\rm B}T}} \, S(q,\delta'). \end{aligned}$$

For finite temperatures $k_{\rm B}T > E_{\rm F}$, where $E_{\rm F} = \frac{\hbar^2 k_{\rm F}^2}{2m}$ is the Fermi energy. Therefore, when $q > k_{\rm F}$ the exponential factor in the last equality becomes very small, making $S(-q,-\delta')$ negligible in comparison to $S(q,\delta')$ in eq. 6.35. Thus we have the approximation

$$\frac{dP_z(t)}{dt} = \frac{\hbar q \Omega_R^2}{2} \int d\delta' \, S(q,\delta') \frac{\sin[\, (\delta - \delta')t \,]}{(\delta - \delta')}. \qquad (6.36)$$

Integrating the above equation over the duration of the Bragg pulse τ_B gives

$$\frac{P_z(t)}{m} = \frac{dX(q,\delta)}{dt} = \frac{\hbar q \Omega_R^2}{2m} \int d\delta' S(q,\delta') \frac{1 - \cos[(\, \delta - \delta')\tau_B \,]}{(\delta - \delta')^2}. \qquad (6.37)$$

This equation gives the COM velocity $V_{\rm COM}$ immediately following the Bragg pulse, where $X(q,\delta)$ is the COM displacement along the direction of the Bragg pulse. If the trap is switched off immediately after the Bragg pulse, the cloud moves with this velocity for the time of flight $\tau_{\rm tof}$; therefore $X(q,\delta) = V_{\rm COM}\tau_{\rm tof}$. Integrating this equation over δ gives

$$\int X(q,\delta) d\delta = \frac{\hbar q \Omega_R^2 \tau_{\rm tof}}{2m} \int \int d\delta' S(q,\delta') \frac{1 - \cos[\, (\delta - \delta')\tau_B \,]}{(\delta - \delta')^2} d\delta. \qquad (6.38)$$

Using contour integration, one can show

$$\int_{-\infty}^{\infty} \frac{1-\cos[\ (\delta-\delta')\tau_B\ ]}{(\delta-\delta')^2} d\delta = \pi\tau_B.$$

Therefore, eq. 6.38 can be written as

$$\begin{aligned} \int X(q,\delta)d\delta &= \frac{\hbar q\Omega_R^2\tau_{\rm tof}}{2m}\pi\tau_B \int d\delta' S(q,\delta') \\ \int X(q,\delta)d\delta &= \frac{\hbar q\Omega_R^2\tau_{\rm tof}}{2m}\pi\tau_B N S(q), \end{aligned}$$

where the definition for the true static structure factor (SSF) is used from eq. 6.10. Thus, the SSF can be directly measured from the COM displacement:

$$\begin{aligned} S(q) &= \frac{2m}{\hbar q\Omega_R^2\tau_{\rm tof}\pi\tau_B N}\int X(q,\delta)d\delta \\ S(q) &= \frac{2m}{\hbar q\Omega_R^2\tau_{\rm tof}\pi\tau_B N} S_{expt}(q). \end{aligned} \tag{6.39}$$

This is similar to equation (5) presented in reference [60] except that the normalization constant is different, because in [60] $S_{expt}(q)$ is defined as the measured momentum transfer divided by $\hbar qN$. Using the relation obtained between $S(q)$ and the pair density correlation functions (eq. 6.31), we obtain $S_{expt}(q) \propto [1 + S_{\uparrow\downarrow}(q)]$. This is the most important result which relates the measured COM displacement of the cloud to the static structure factor and hence to the pair correlation function.

6.6 Summary

From this chapter, it is evident that Bragg scattering experiments provide a unique way to probe pair correlations in a strongly interacting fermionic system. The principles of Bragg spectroscopy are explained through free particle excitations. In the limit of large

momentum transfer $q > k_F$, the important role played by pair correlations is highlighted through their link to the static structure factor $S(q)$ (eq. 6.31). It has been shown that this factor can be measured through Bragg spectroscopy by quantifying the momentum imparted to the cloud in terms of the COM displacement (eq. 6.39). When particles in different spin states are highly correlated, as is the case for bound molecules (BEC side), $S_{\uparrow\downarrow}(q) = 1$ and the normalized $S(q) = 2$. When these correlations vanish $S_{\uparrow\downarrow}(q) = 0$, the $S(q) = 1$ as in the case of non-interacting fermions (BCS side). In the unitarity regime, quantum Monte-Carlo simulations predict [51] strong correlations between the interacting fermions, suggesting $1 < S(q) < 2$. With this theoretical motivation, Bragg spectroscopy is performed across the BEC-BCS crossover to quantify the two-body pair correlations for the first time. The results and analysis of the experiments are presented in Chapters 7 and 8.

Chapter 7

Bragg scattering - collisionless regime

7.1 Introduction

In this chapter, the collionless behaviour of atoms and molecules/pairs are studied across the BEC-BCS crossover. The main objective is to measure two-photon Rabi frequencies (sec. 7.4) of both atoms and molecules and to obtain Bragg spectra (sec. 7.5) across the crossover in the low density limit. Since the Bragg resonance condition (eq. 6.1) is mass dependent, the presence of atoms or molecules/pairs shows up as a peak in the response spectrum at their corresponding resonant frequencies. The Bragg resonant frequencies for ^{6}Li atoms and molecules are $\delta_{atom}/2\pi = 294.7$ kHz and $\delta_{mol}/2\pi = 147.4$ kHz, respectively. Due to the large scattering length in these gases, elastic collisions can distort the particle distributions making it difficult to analyse the Bragg signal. For this reason, the COM displacement of the cloud along the direction of the Bragg pulse is used to quantify the spectral features (sec. 7.2), instead of counting the number of scattered particles. For the same reason, the relative fraction of the constituent particles (atoms or molecules) in the gas is obtained from absorption

images of the Rabi oscillation sequences (see sec. 7.4.1).

7.2 Analysis of the Bragg signal

The starting point for our experiments is a gas of ^{6}Li in an equal spin mixture of the $|1\rangle$ and $|2\rangle$ states evaporatively cooled in a single beam optical dipole trap. First a highly degenerate cloud is produced containing 1.3×10^5 atoms in each spin state at a magnetic field of 835 G. Then the trap depth is increased by a factor of two to avoid any atom loss during the adiabatic ramp (in 100 ms) to the desired magnetic field (B) where they are held for 200 ms to let the transient magnetic field vanish. Bragg scattering and imaging take place at this final magnetic field.

In most of the Bragg scattering experiments performed by other groups [87, 88, 61, 60, 63], the ratio of the scattered fraction of particles with respect to the remaining unscattered cloud is normally taken as a standard Bragg signal. In these experiments, the elastic collisions between the scattered and unscattered particles are negligible. Therefore, it is possible to count the atoms which appear in a spatially separated scattered cloud after a sufficiently long time of flight. However, in our experiments, the strong interactions (large scattering length near unitarity) cause elastic collisions which distort the particle distributions making it difficult to analyse the Bragg signal. Therefore, to quantify the momentum imparted to the cloud by the Bragg pulse, the centre-of-mass (COM) displacement of the distribution is measured.

The elastic collisions can be reduced by expanding the gas before applying the Bragg pulse, so that a clear scattered cloud is observed. This method of Bragg scattering is referred as the *collisionless regime* throughout this thesis.

Alternatively, if the Bragg pulse is applied to a trapped gas, the interactions can affect the Bragg spectra and this method is referred as the *interacting regime*.

In either case, the COM displacement spectrum is evaluated in the following way :

1. For every absorption image taken after a Bragg pulse, at a particular Bragg frequency, the COM position of the particle distribution is evaluated using the relation $\frac{\sum m_i r_i}{\sum m_i}$ where m_i is taken as the pixel intensity and r_i is the pixel position.

2. Similarly, the COM position of the cloud imaged in the absence of a Bragg pulse (molecular BEC or a degenerate Fermi gas) is calculated for the same time of flight. This value is then subtracted from the one obtained in step 1 to get the COM displacement of the scattered cloud along the direction of the Bragg pulse.

3. Such COM displacements are evaluated from all the absorption images, taken for the range of Bragg frequencies, and joined together to create a Bragg spectrum.

4. Two Gaussian curves are fitted to the spectra to distinguish the scattered molecules and atoms.

7.3 Collisionless behaviour

To probe the composition of particles (atoms/pairs) in a non-interacting gas, Bragg scattering is performed on an expanded gas. Once the dipole trap is switched off, the mean field energy of the interacting gas is converted into kinetic energy and the cloud expands. After expansion, the cloud consists of free particles with a wide range of velocities. Since Bragg scattering is highly momentum sensitive and the momentum width of the scattering transition is narrower than that of the expanded cloud, only particles within a certain Bragg momentum range are scattered [87]. Because atoms scatter with twice the velocity $v_{recoil} = \frac{q}{m}$ of molecules, owing to their mass difference, they travel twice the distance of molecules for the same time of flight. This is another way, apart from their resonant frequencies, that Bragg scattering can distinguish atoms from molecules.

To demonstrate collisionless Bragg scattering, a degenerate gas is made as described in sec. 4.10. The dipole trap is then switched off and the cloud expands for 4 ms

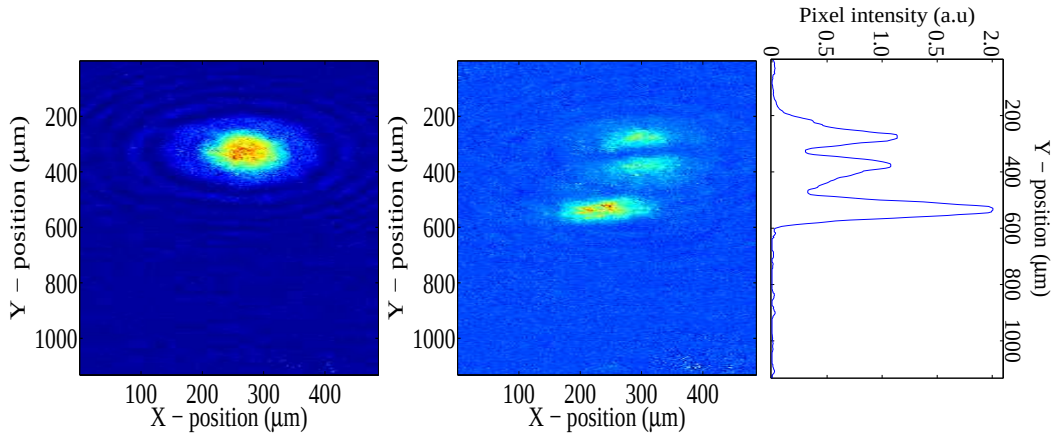

(a) without Bragg pulse (b) with 30 μs pulse (c) Integrated (b) along the X-direction

Figure 7.1: Bragg scattering of molecules at 730 G.

before applying the Bragg pulse. Following the pulse, a further 2 ms of expansion is allowed before taking an absorption image. Figure 7.1b shows the scattering of molecules at 730 G (BEC side) from a molecular condensate after applying a 30 μs Bragg pulse at a Bragg frequency of 132 kHz. For comparison, Fig. 7.1a shows a pure molecular condensate imaged after the same time of flight without applying a Bragg pulse. Similarly, Fig. 7.2b shows the scattering of atoms at 860 G (BCS side) from a

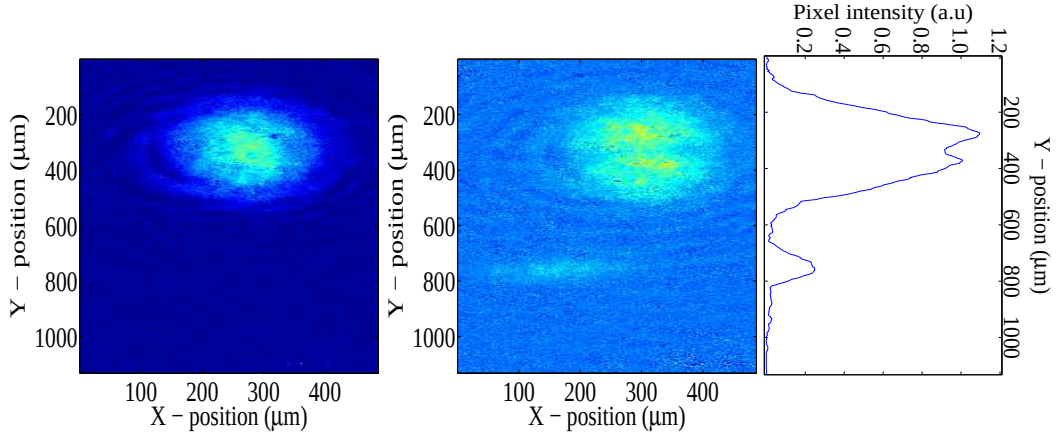

(a) without Bragg pulse (b) with 50 μs pulse (c) Integrated (b) along the X-direction

Figure 7.2: Bragg scattering of atoms at 860 G.

degenerate Fermi gas after applying a 50 μs Bragg pulse at a Bragg frequency of 285 kHz, and Fig. 7.2a shows the same conditions without a Bragg pulse.

Note that the observed resonant frequencies for molecules and atoms are lower than the calculated values $\delta_{mol}/2\pi = 147.4\,\text{kHz}$ and $\delta_{atom}/2\pi = 294.7\,\text{kHz}$, respectively. This is because, during the TOF expansion of the cloud, the particles are accelerated in the stray Feshbach magnetic fields, which increases their velocities causing a Doppler shift in the observed Bragg frequencies. The scattered intensity of the molecules (fig. 7.1c) is observed to be higher than that of atoms (fig. 7.2c) due to the presence of a large population of zero momentum molecules in the condensate. On the BCS side of the resonance, fermions occupy many more quantum states; so fewer atoms lie in the momentum window of the Bragg pulse. Also, the width of the parent (central) cloud is larger for the DFG than for a molecular BEC due to the larger momentum distribution of fermions. Finally, due to the near perpendicular alignment of the Bragg beams (see Fig. 4.9) with respect to the axis of the dipole trap, the scattered particles appear at an angle with respect to the parent cloud.

7.4 Two-photon Rabi oscillations

Bragg scattering can be viewed as a Raman transition between two momentum states of the same magnetic sublevel. This can be treated as a simple two-level system, interacting with a periodic time-dependent optical field. It can be easily shown [95] that for such a system the particle will oscillate between these two momentum states with a frequency Ω_R, the two-photon Rabi frequency. This can be written in terms of the intensity (I_1 and I_2) of each Bragg beam, the detuning (Δ) from the resonant transition, the line width (Γ) of the transition and the saturation intensity (I_{sat}) [83]:

$$\Omega_R = \frac{\Gamma^2}{4\,\Delta}\frac{\sqrt{I_1 I_2}}{I_{sat}} \tag{7.1}$$

The intensity of the beam is given by $I = \frac{2P}{\pi w_o^2}$, where P is the power in the beam and w_o is the beam waist. The probability of finding a particle in the excited state after a time t is given by

$$P(t) = \sin^2(\frac{\Omega_R t}{2}). \tag{7.2}$$

When $t = \frac{\pi}{2\Omega_R}$, the number of particles in each momentum state becomes equal, *i.e.,* $P(t) = \frac{1}{2}$ and a pulse of such width is termed a $\frac{\pi}{2}$ pulse. When $t = \frac{\pi}{\Omega_R}$, all the particles are scattered to the higher momentum state, *i.e.,* $P(t) = 1$ and the pulse is termed a π pulse. Experimentally, Ω_R is obtained by fitting the following function to the scattered fraction (SF) of particles measured as a function of the pulse width t

$$\text{SF} = \frac{A}{2}\left(1 - e^{-\frac{t}{\tau}}\cos(\Omega_R t)\right), \tag{7.3}$$

where $e^{-\frac{t}{\tau}}$ is a damping term and A is the amplitude.

Bragg temporal regime: To ensure that the system truly undergoes Bragg scattering, the Bragg pulse duration should be large enough to scatter to the first-order momentum state but small enough to avoid scattering into higher order momentum states and also to minimize spontaneous emission events, *i.e.,* [96]

$$\frac{1}{4}\left(\frac{2\pi}{\omega_r}\right) \ll \tau_B \ll \frac{4\pi\Delta}{\Gamma\Omega_R}, \tag{7.4}$$

where τ_B is the duration of the Bragg pulse, ω_r is the single-photon recoil frequency and Γ is the natural linewidth of the transition. The single photon recoil energy E_r is related to ω_r by the relation

$$E_r = \hbar\omega_r = \frac{\hbar^2 k^2}{2m}, \tag{7.5}$$

which gives $\omega_r = 2\pi{\cdot}74$ kHz for atoms and $\omega_r = 2\pi{\cdot}37$ kHz for molecules. Substituting the values for our experimental parameters for ^{6}Li, the Bragg pulse duration is constrained by 3.4 μs $\ll \tau_B \ll$ 135 ms for atoms and 6.8 μs $\ll \tau_B \ll$ 135 ms for molecules. For the experiments mentioned in this thesis, the pulse duration is chosen such that $\tau_B = 40$ μs for probing the interacting regime (chapter. 8) and up to $\tau_B =$

0.4 ms for probing the collisionless regime (sec. 7.5), which are both well within the Bragg regimes.

7.4.1 Oscillation sequences

Two-photon Rabi frequencies (Ω_R) of molecules (at $\delta_{mol}/2\pi = 135$ kHz) and atoms (at $\delta_{atom}/2\pi = 280$ kHz) in the collisionless regime were measured using a fixed Bragg intensity ($I = 8.2$ mW/cm^2) and varying the pulse duration from 10 μs to 100 μs in steps of 10 μs. In order to illustrate the pattern of the scattered particles from an expanded gas, the absorption images taken for different conditions were joined together as explained below:

1. Each absorption image taken with a particular Bragg pulse is integrated along the X-direction (perpendicular to the direction of the Bragg pulse) to obtain a 1D-line profile as shown in Fig. 7.1c (molecules) and Fig. 7.2c (atoms).

2. Such line profiles of all the absorption images taken for various Bragg pulse durations are joined together to create a sequence of absorption images.

3. From this *Rabi oscillation sequence* (Fig. 7.3d) of molecules taken at 710 G it can be seen that the molecules are scattered from the central region of the parent cloud.

4. Similarly, Fig. 7.3h shows the oscillation sequence of atoms at 850 G created by joining the horizontally integrated single images like Fig. 7.3e, Fig. 7.3f and Fig. 7.3g.

5. From such *Rabi oscillation sequences*, a thin slice of the image is taken horizontally around the scattered region of the particles, along the direction of the pulse durations, to obtain the signal for Rabi oscillations.

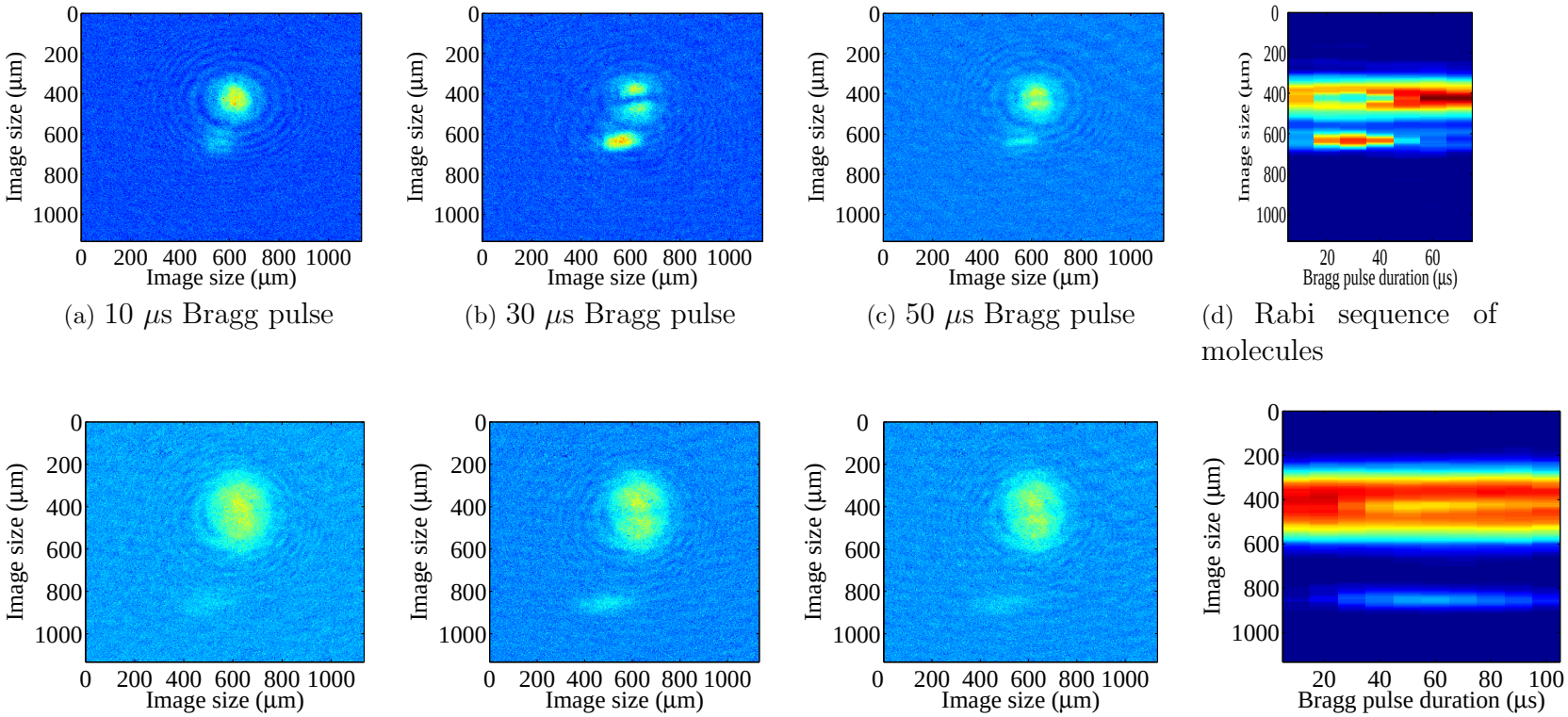

(a) 10 μs Bragg pulse (b) 30 μs Bragg pulse (c) 50 μs Bragg pulse (d) Rabi sequence of molecules

(e) 20 μs Bragg pulse (f) 50 μs Bragg pulse (g) 100 μs Bragg pulse (h) Rabi sequence of atoms

Figure 7.3: Making Rabi oscillation sequences from single absorption images taken at different conditions. Fig. (a-d) show the scattering of molecules at 730 G and Figure.(e-h) show the scattering of atoms at 860 G.

7.4.2 Rabi Frequencies for atoms and molecules

Figure 7.4a shows the observed two-photon Rabi oscillations of molecules taken at 745 G with various powers, 50 μW, 100 μW and 185 μW. $\Omega_R = 2\pi\nu_R$ is obtained from this data by fitting a decaying sinusoidal curve (eq. 7.3) and Fig. 7.4b shows the

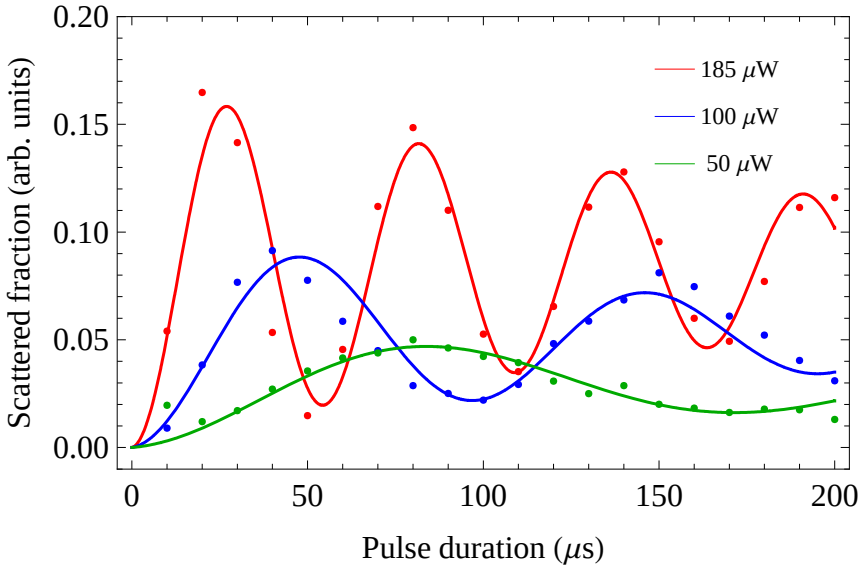

(a) The data is fitted with eq. 7.3 to obtain ν_R at different powers.

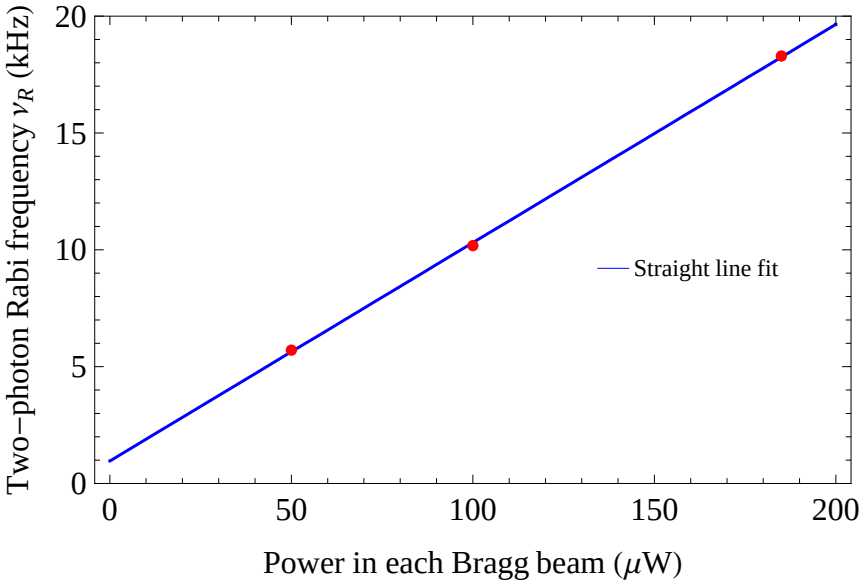

(b) ν_R obtained from (a) is plotted versus power.

Figure 7.4: Two-photon Rabi frequencies for molecules taken at 745 G.

evaluated ν_R at different powers with constant detuning ($\Delta/2\pi = 1592$ MHz). Taking the values $\Gamma/2\pi = 5.9$ MHz and $I_{sat} = 2.54$ mW/cm^2 for the ^{6}Li $D2$-line, a beam waist of $w_o = 0.55$ mm is obtained from the slope of the straight line fit to the data points, using eq. 7.1.

The line profiles of the scattered fraction of molecules and atoms are generated

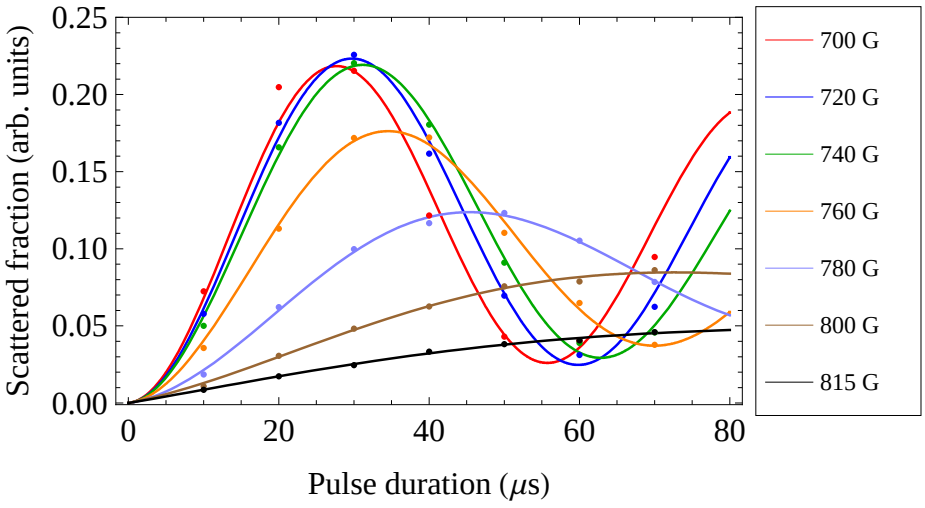

(a) Two-photon Rabi oscillations of molecules.

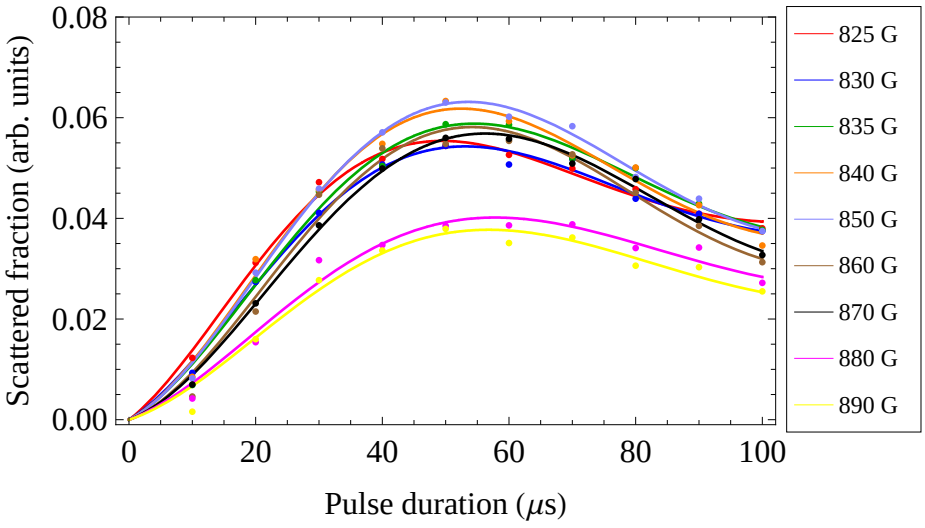

(b) Two-photon Rabi oscillations of atoms.

Figure 7.5: Two-photon Rabi oscillations of molecules and atoms at various magnetic fields.

from the *Rabi oscillation sequences* taken at various magnetic fields as mentioned in section. 7.4.1. The line profiles obtained in this way across the BEC-BCS crossover are fitted with eq. 7.3 to obtain their two-photon Rabi frequencies. Figure 7.5 shows this data along with non-linear best fit curves. The molecular Rabi frequencies are observed to decrease slowly with increase in the magnetic field, whereas the atom signals are seen to oscillate almost with the same Rabi frequency.

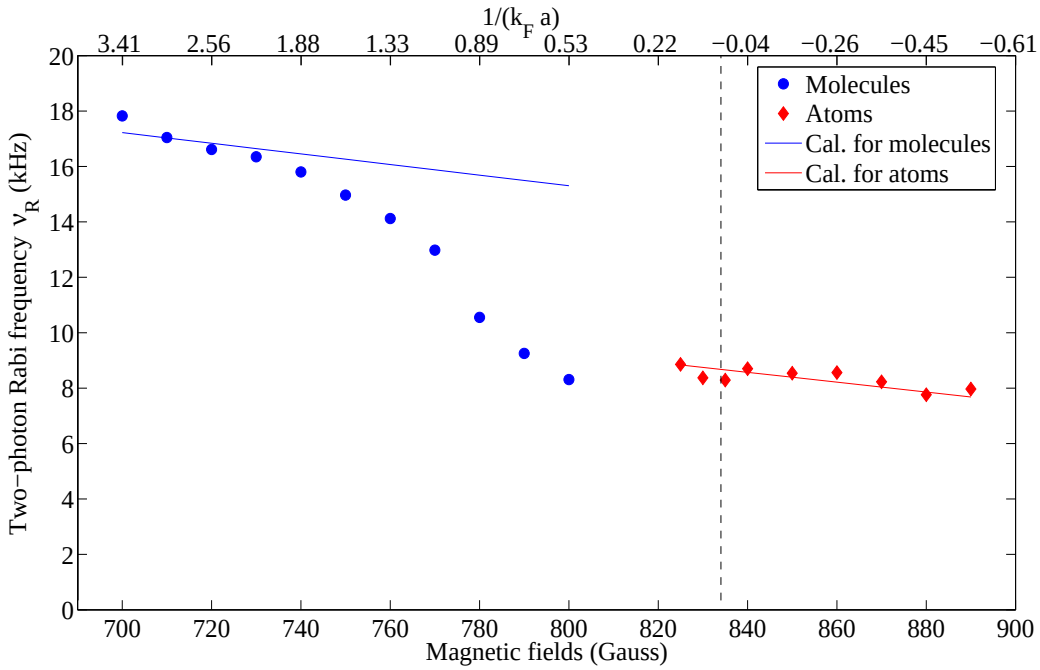

Figure 7.6: Two-photon Rabi frequencies of molecules and atoms across the BEC-BCS crossover. The vertical dotted line indicates the position of unitarity.

Figure 7.6 shows the evaluated two-photon Rabi frequencies along the BEC-BCS crossover with the calculated ν_R for both molecules and atoms. The measured two-photon Rabi frequency is close to that of the calculated value for both molecules (far on BEC side) and atoms (on BCS side), which is a manifestation of their free particle behaviour. Also, it is observed that molecules oscillate with twice the Rabi frequency of atoms as they have twice the polarisability [83]. It is interesting to note that on the BEC side of the Feshbach resonance, molecules show a deviation from the free particle behaviour. This could be due to the increased size of the molecular wavefunction near

the Feshbach resonance. Figure 7.7 shows the calculated value of the atomic scattering length a versus magnetic field. Since the values are close to the actual size of the molecules, it can be seen that they becomes comparable to the wavelength (λ=671 nm) of the Bragg beams and their oscillations can no longer be treated under the semi-classical electric dipole approximation. However, on the BCS side, atoms scatter as free particles as their size is always very small compared to the wavelength of the light.

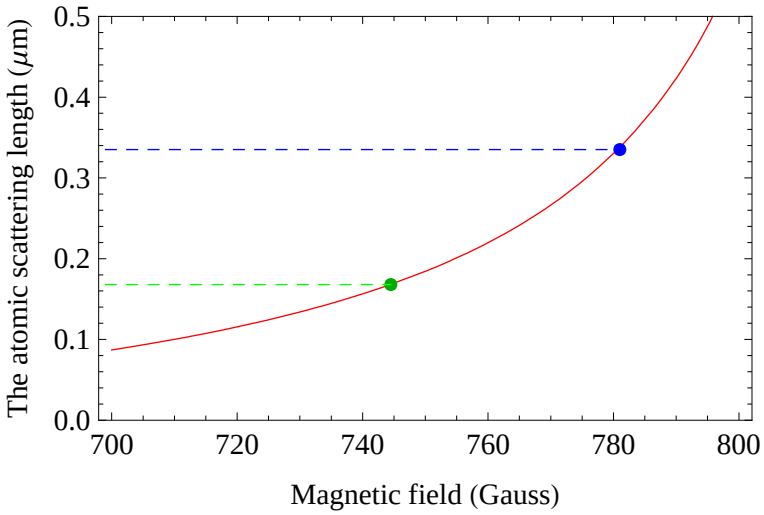

Figure 7.7: Size of the molecules a versus magnetic fields. The green (blue) point shows where the size of the molecule becomes 1/4 (1/2) of the wavelength λ=671 nm of the laser light.

7.5 Bragg spectra across the BEC-BCS crossover

Bragg scattering of molecules/pairs and atoms is performed at different magnetic fields across the BEC-BCS crossover by varying the Bragg frequency from 80 kHz to 380 kHz in steps of 10 kHz, while keeping the intensity (I = 8.2 mW/cm^2) and the pulse duration constant. To illustrate the pattern of the scattered particles from an expanded gas, all the absorption images taken under different conditions are joined together as explained below:

1. Each absorption image taken at a particular Bragg frequency is integrated along the X-direction (perpendicular to the direction of the Bragg pulse) to obtain a 1D-line profile (similar to fig. 7.1c and fig. 7.2c).

2. Such line profiles of all the absorption images taken for various Bragg frequencies are joined together to create a sequence of absorption images.

3. In such a sequence (Fig. 7.8a), the high density central clouds are shown by red and yellowish green colours. The particles (light green) are observed to scatter downwards along the direction of the Bragg pulse.

Figure 7.8a shows the Bragg spectrum constructed in this way at a magnetic field of 810 G with a 60 μs Bragg pulse. The particles are observed to scatter in two different regions of the spectrum. The first region is due to the scattering of molecules around the Bragg resonant frequency of 147 kHz, whereas the second region is due to the scattering of atoms around 294 kHz. In both cases, the location of the scattered cloud follows a diagonal line in Fig. 7.8a (shown by the dotted line). This is due to the fact that as the Bragg frequency is varied particles with different momentum become resonant with the Bragg pulse. In our experiment, as the frequency is increased, the region from where molecules/atoms are scattered shifts from the top to the bottom of the central cloud. This can be noticed by the presence of a diagonal gap in the central cloud whose location follows a similar diagonal path. The spacing between the scattered atoms and the parent cloud (shown by vertical lines) is observed to be twice that of the molecules. Although the atoms and molecules receive the same momentum kick ($\hbar q$) from the Bragg pulse, due to the mass difference atoms travel twice as far as molecules.

Once the Bragg spectrum is obtained, the COM displacement is evaluated as explained in sec. 7.2 and shown in fig. 7.8b. The data is fitted with a sum of two Gaussian curves to guide the eye. In this spectrum, the first (second) peak corresponds to the scattering of molecules (atoms).

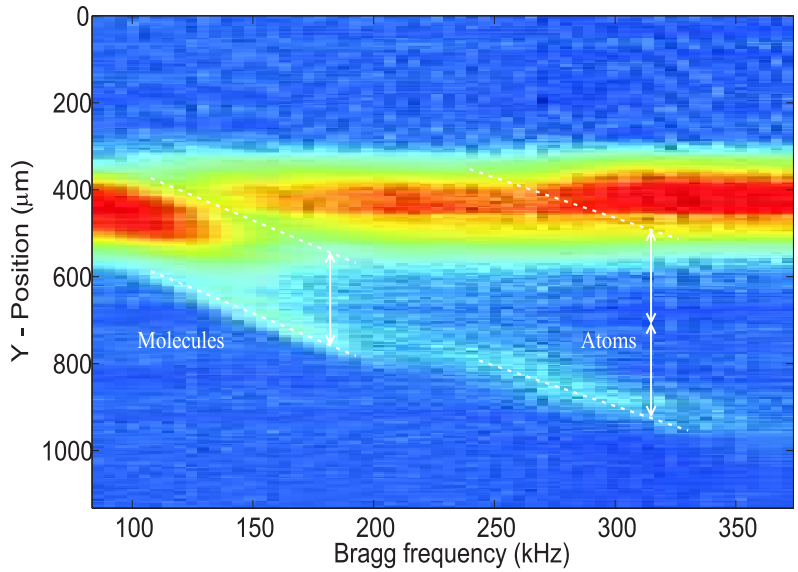

(a) Free particle Bragg spectrum at 810 G with 60 μs Bragg pulse.

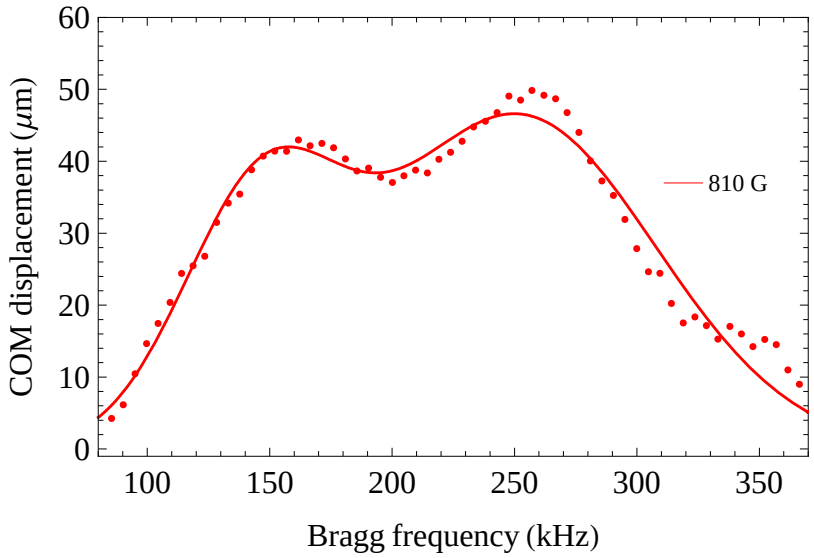

(b) Spectrum of COM displacement obtained from the line profiles at 810 G.

Figure 7.8: Free particle Bragg spectrum at 810 G. In (b) the sum of two Gaussian peaks is shown (solid line) as a fit to guide the eye.

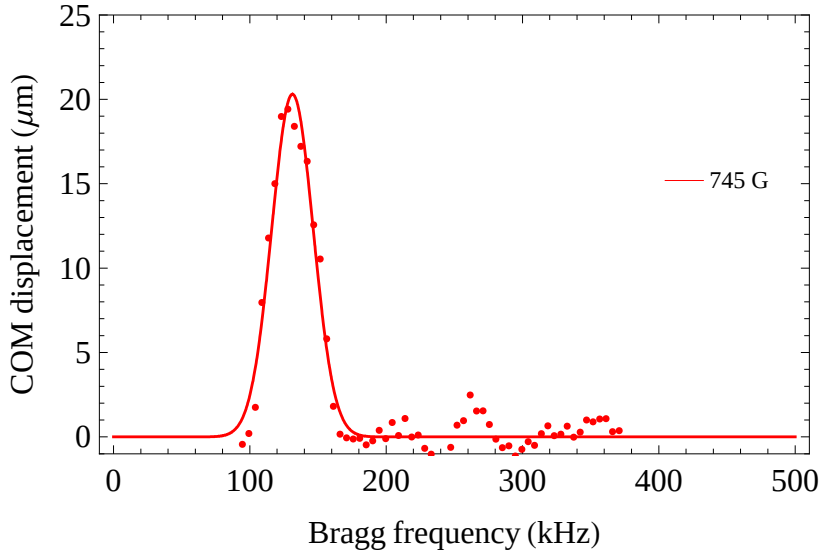

(a) Free particle Bragg spectrum of molecules at 745 G.

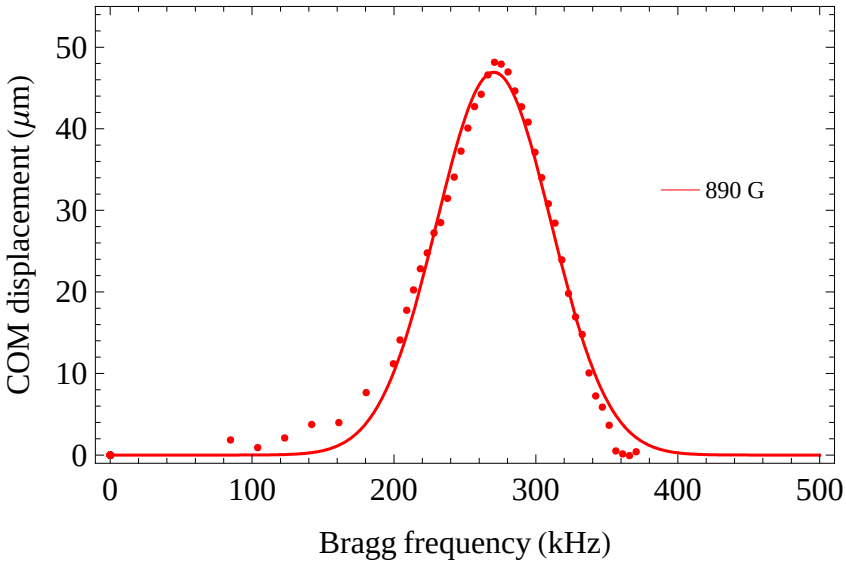

(b) Free particle Bragg spectrum of atoms at 890 G.

Figure 7.9: Free particle Bragg spectra. A Gaussian peak is shown (solid line) as a fit to guide the eye.

Bragg spectra taken far away from the Feshbach resonance show scattering of purely molecules (see Fig. 7.9a) on the BEC side (745 G) and purely atoms (see Fig. 7.9b) on the BCS side (890 G). These spectra were taken under different conditions to achieve a clear Bragg scattering signal with less collisional scattering. At 745 G a short (80 μs) and lower intensity ($I = 2.2$ mW/cm^2) Bragg pulse is used to obtain a π-pulse, whereas at 890 G a shorter (40 μs) pulse is used, keeping the intensity at $I = 8.2$ mW/cm^2. From these spectra, it can be seen that on the BEC side, due to the presence of a large condensate fraction, the width of the momentum distribution is narrow, whereas for atoms on the BCS side, the momentum distribution is broader due to the Fermi pressure.

To quantify all of these data, the scattered fraction of particles is evaluated from the *Rabi oscillation sequences* at various magnetic fields, by counting the total scattered particles after one-half of a Rabi cycle. In this way, the results are normalized and do not depend on the Bragg pulse duration. The obtained scattered fraction

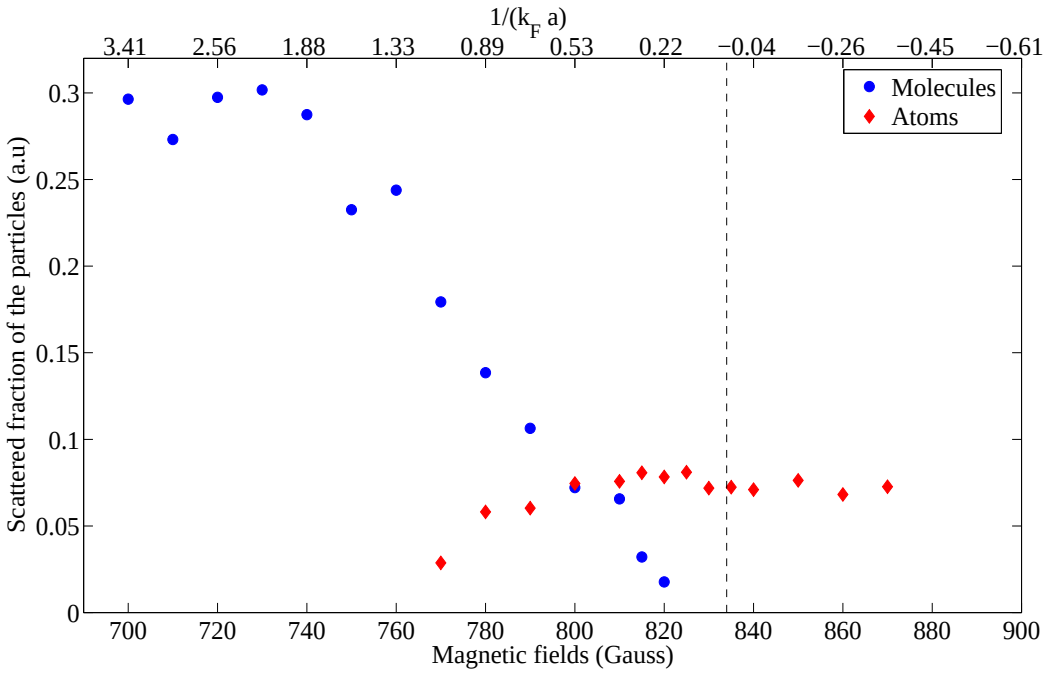

Figure 7.10: Relative fraction of scattered pairs and atoms across the BEC-BCS crossover. The vertical dotted line indicates the position of the Feshbach resonance.

of molecules/pairs and atoms across the BEC-BCS crossover is shown in Fig. 7.10. Below 750 G, the molecules are seen to scatter with a constant amplitude. However, their response is observed to decrease from the BEC to the BCS side of the Feshbach resonance. No free pairs are seen to be scattered at magnetic fields above the Feshbach resonance. On the other hand, the thermal atoms are observed to scatter from 760 G, and above 820 G they scatter with a constant amplitude.

7.6 Summary

The collisionless behaviour of atoms and molecules/pairs is studied across the BEC-BCS crossover by measuring two-photon Rabi oscillations. The deviation of the measured two-photon Rabi frequencies for molecules from the calculated (free particle) values, near the BEC side of the Feshbach resonance, suggests an increase in the pair size. The Bragg spectra are analysed in terms of the COM displacement of the cloud along the direction of the Bragg pulse. Atoms and molecules are observed to scatter around their respective Bragg resonant frequencies. The width of the momentum distribution is observed to be narrow on the BEC side, due to the large condensate fraction, and broad on the BCS side, due to the Fermi pressure. For short pulse durations ($<$100 μs), the ratio of the constituent particles is obtained from the Rabi oscillation spectra, which also show scattering of pairs near the BEC side of the Feshbach resonance. In order to verify the presence of these pairs with certainty, Bragg scattering is performed on a trapped cloud, where the density is higher and hence the interactions are stronger. Results from this experiment are presented in the next chapter (Chapter. 8).

Chapter 8

Bragg scattering - Interacting regime

8.1 Introduction

This chapter presents the key experimental results obtained in this thesis. The results were published recently in [97]. Bragg spectroscopy is applied to a strongly interacting Fermi gas across the BEC-BCS crossover regime. From the observed Bragg spectra in this regime, pair correlations between spin-up and spin-down fermions are quantified and their density dependence is revealed. Unlike the collisionless regime (Chapter. 7), Bragg scattering of a trapped gas can reveal the effects of strong interactions, and for the same reason the analysis of the Bragg signal becomes more difficult. Once again, the spectra are constructed by measuring the COM displacement of the cloud as discussed previously in section 7.2. The Bragg response function (spectrum) is calculated for both ideal bosons and fermions, under the impulse approximation at zero temperature, and compared with the observed data. Following this, the static structure factors are measured by integrating the Bragg spectra and normalizing with respect to the bound molecule limit (sec. 8.4). All of the results presented here are obtained for the

lowest trap temperatures achievable in our set-up. An empirical temperature of the strongly interacting Fermi gas is obtained by integrating the absorption image along the weak trapping axis and fitting a 1D-density profile of non-interacting fermions, after including appropriate scaling factors (see sec. 2.5).

8.2 Behaviour of interacting particles

Due to the presence of large particle densities, the trapped gas regime becomes an ideal set-up to study two-body correlations across the BEC-BCS crossover. However, in Bragg scattering experiments, elastic collisions between the scattered and unscattered particles can distort the resulting atomic distribution (see Fig. 8.1b), making it difficult to analyse the data. Usually it is not possible to easily discern a spatially separated scattered cloud that can be used as the standard signal of Bragg scattering. Therefore, to quantify the momentum imparted to the cloud due to the Bragg pulse, the centre of mass displacement of the atomic distribution is measured as described in section 7.2.

To probe the interacting regime, a sample of degenerate gas is produced by the

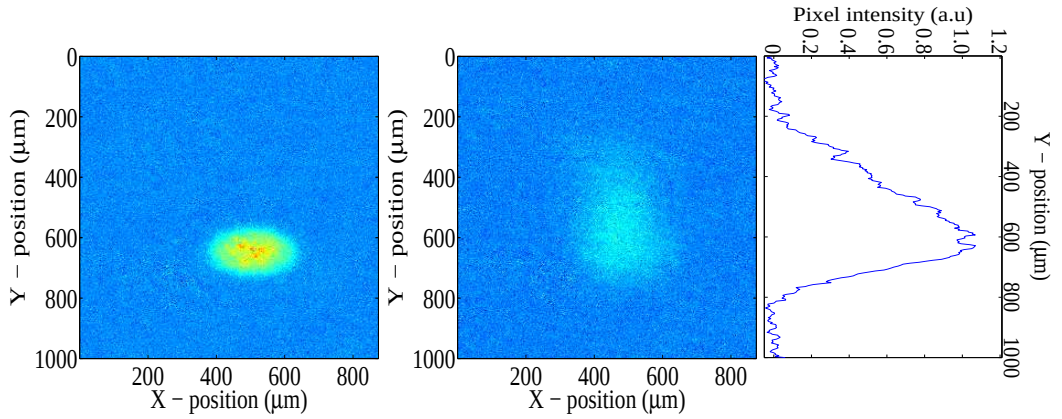

(a) without Bragg pulse (b) with 40 μs pulse (c) Integrated image (b) along the X-direction

Figure 8.1: Bragg scattering of molecules in a trapped gas at 780 G.

method described in sec. 4.10. After this, a Bragg pulse of 40 μs duration is applied to the trapped gas and the trap is then switched off immediately. An absorption image is taken after a 4 ms time of flight.

8.3 Bragg spectra across the BEC-BCS crossover

Bragg scattering of a trapped gas is performed at different magnetic fields across the BEC-BCS crossover by varying the Bragg frequency from 5 kHz to 480 kHz in steps of 10 kHz while keeping the intensity (I = 5 mW/cm^2) and the pulse duration (40 μs) constant. Figure. 8.1 shows molecular condensates with (Fig. 8.1b) and without (Fig. 8.1a) application of a Bragg pulse. In order to illustrate the pattern of the scattered particles from the trapped gas, all the absorption images taken at different conditions are joined together as explained below :

1. Each absorption image taken at a particular Bragg frequency is integrated along the X-direction (perpendicular to the direction of the Bragg pulse) to obtain a 1D-line profile as shown in Fig. 8.1c.

2. Such line profiles of all the absorption images obtained at the different Bragg frequencies are joined together to create a sequence of absorption images.

3. In such a sequence (Fig. 8.2a), the high density central clouds are shown by red and yellowish green colors. The particles are observed to scatter (upwards) along the direction of the Bragg pulse, distorting the central cloud around the resonant frequency ($\delta_m/2\pi$ =147 kHz in this case).

As explained in sec. 7.2, the COM displacement spectrum is obtained and shown in Fig. 8.2b. Similar spectra are evaluated for various magnetic fields across the BEC (Fig. 8.3a)-BCS (Fig. 8.3b) crossover. The dominant peak at 147 kHz in these spectra on the BEC side corresponds to the scattering of molecules. The height and sharpness

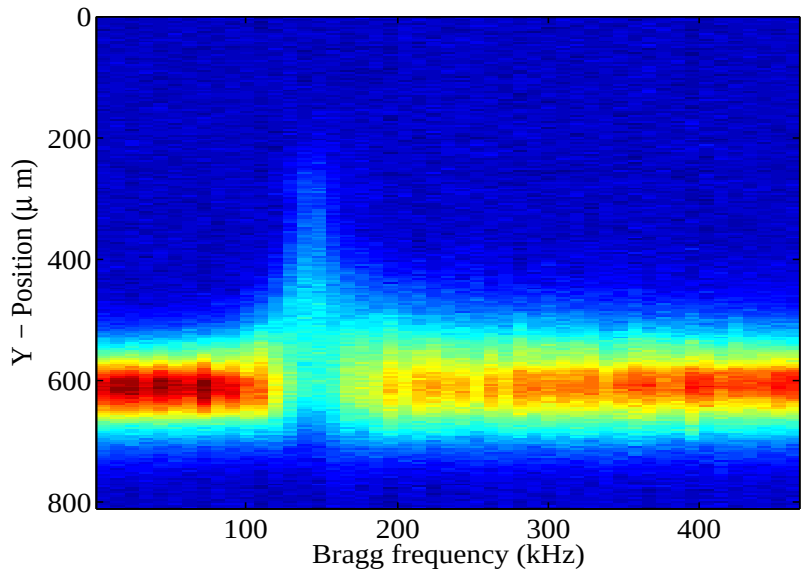

(a) Absorption images Bragg spectrum of trapped gas at 780 G.

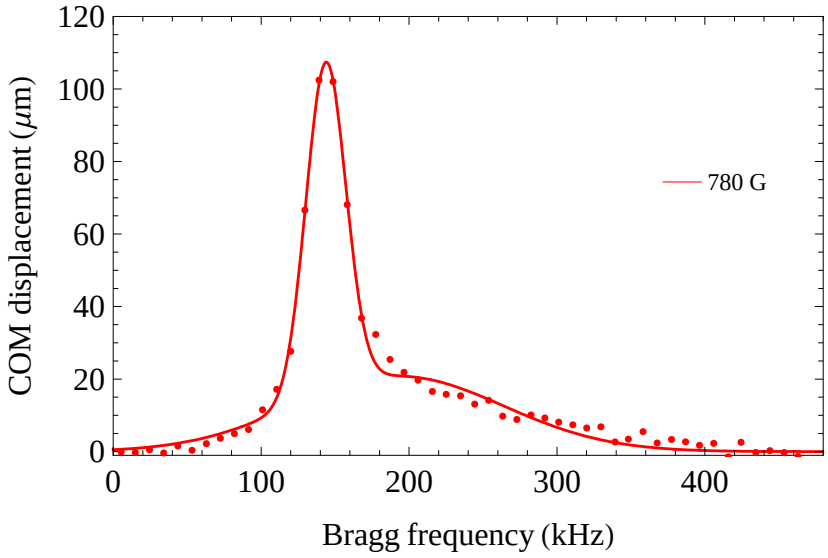

(b) Spectrum of the COM displacement obtained from the line profiles.

Figure 8.2: Bragg spectrum of a trapped gas at 780 G. The sum of two Gaussian peaks is shown in (b) (solid line) as a fit to guide the eye.

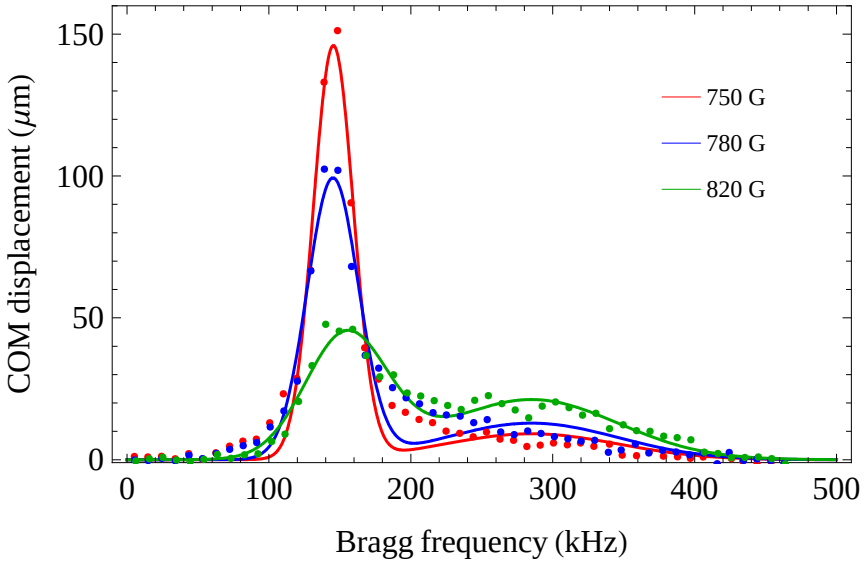

(a) Bragg spectra of trapped gas on the BEC side.

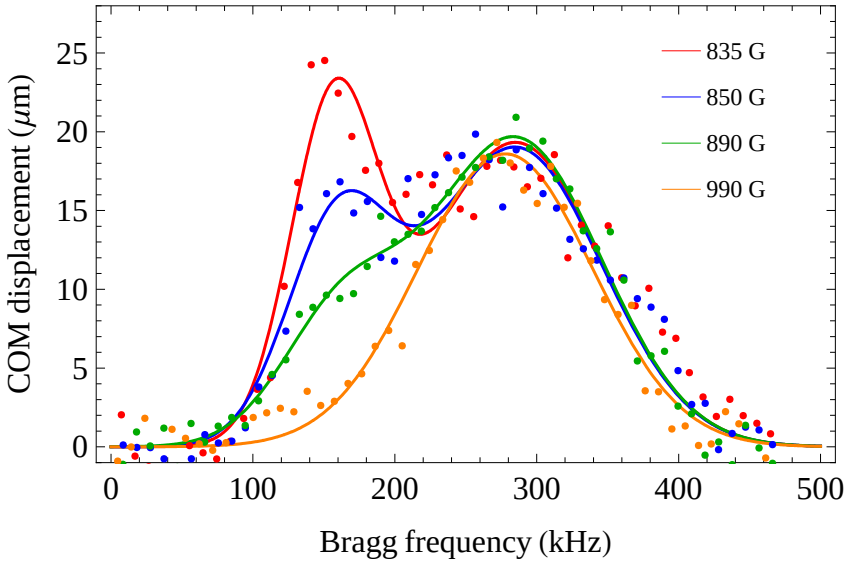

(b) Bragg spectra of trapped gas on the BCS side.

Figure 8.3: Bragg spectra across the BEC-BCS crossover. The sum of two Gaussian peaks is shown (solid line) as a fit to guide the eye, except for the 990 G data where a single Gaussian peak is used.

of this peak signifies a large condensate fraction. However, a small fraction of scattered free atoms contributes to an asymmetry in the spectra. At unitarity (835 G), the peak at the molecular resonant frequency is still significant (Fig. 8.3b), indicating the presence of a substantial fraction of correlated pairs (with the same mass as molecules) in a trapped interacting Fermi gas.

At higher magnetic fields on the BCS side, this pair signal is observed to gradually decrease as the length scale for pair correlations increases. On the other hand, the atomic excitations obtain a constant amplitude and the spectrum approaches that of an ideal Fermi gas.

To quantify these results, the data are fitted with the sum of two Gaussian curves

$$Fit = A_m e^{-\frac{(\delta-\delta_m)^2}{2\sigma_m^2}} + A_a e^{-\frac{(\delta-\delta_a)^2}{2\sigma_a^2}}, \tag{8.1}$$

one for molecules/pairs and the other for atoms, where δ is the Bragg frequency, A_a (A_m) is the amplitude of the scattered atoms (molecules/pairs) and σ_a (σ_m) is the width of the atomic (molecular/pair) peak. Fitting a Gaussian profile is only an approximation to help quantify the centre positions and root-mean-square widths of the two peaks. In order to quantify the behaviour of the molecular/pair peak widths and amplitudes, the atomic width and its resonant frequency are held constant at $\sigma_a/2\pi$=60 kHz and $\delta_a/2\pi$=285 kHz, respectively, in fitting eq. 8.1 to the data. These parameters are chosen from the Bragg spectra taken at 990 G for a weakly interacting Fermi gas.

Figure 8.4a shows the evaluated peak amplitudes for molecules (/pairs) and atoms from the fits. This plot is similar to the ratio plot (Fig. 7.10) obtained in the collionless regime where the densities were smaller than for these trapped gases. Here, the molecular peak amplitudes are higher on the BEC side (750 G and 780 G) and on the BCS side the atomic excitations approach a constant value corresponding to that of an ideal Fermi gas. In contrast to the low density case (collisionless regime) at

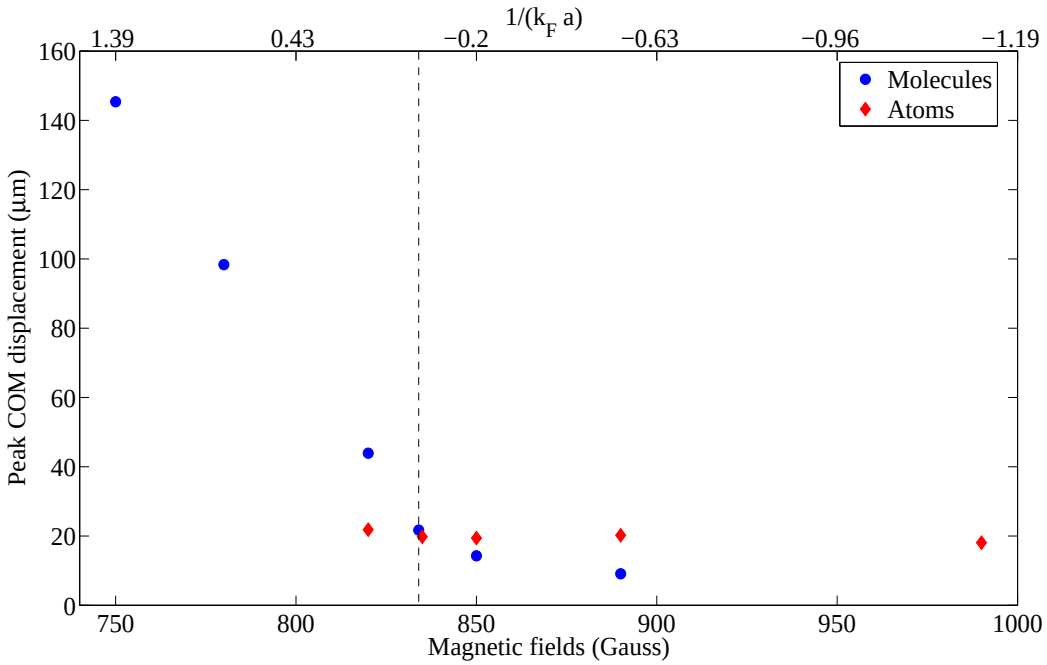

(a) Peak amplitudes of the scattered particles across the BEC-BCS crossover.

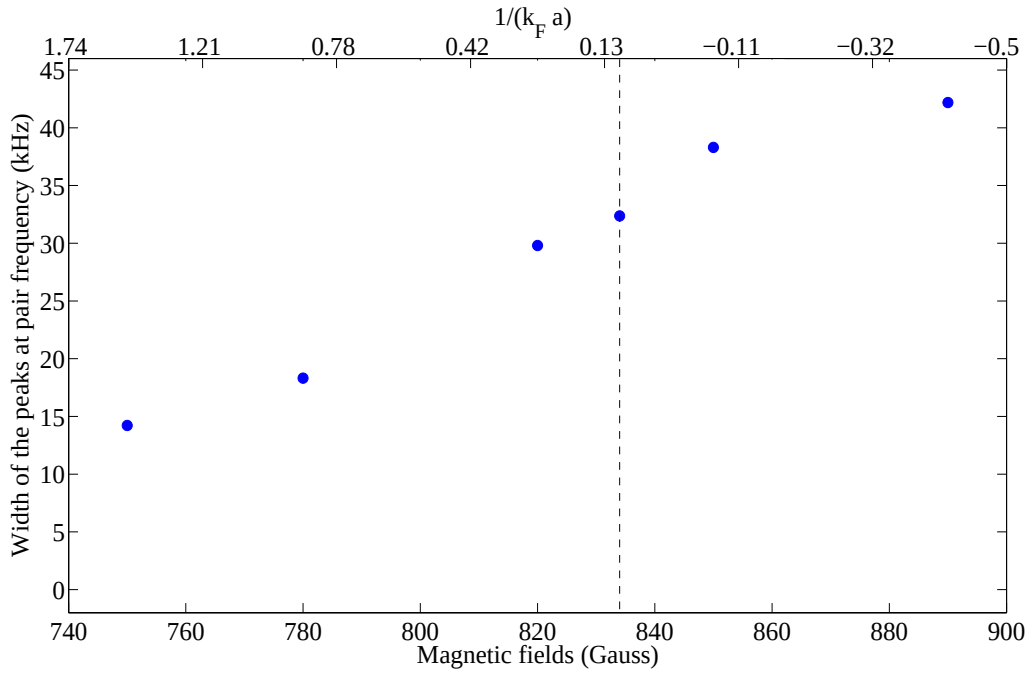

(b) Peak width of the scattered molecules/pairs across the BEC-BCS crossover.

Figure 8.4: Amplitudes and widths of the Bragg signals obtained from the fits, across the BEC-BCS crossover. The vertical dotted line indicates the position of unitarity.

unitarity, there is a non-zero amplitude for the peak at $\delta/2\pi = 147$ kHz, indicating the presence of a substantial fraction of correlated pairs. Figure 8.4b shows the evaluated peak widths for molecular/pair peaks across the BEC-BCS crossover. This plot reveals that the momentum distribution evolves smoothly from a narrow molecular condensate peak to a broader strongly interacting Fermi gas peak, due to the increase in spread of the particle energies.

8.4 Measuring the static structure factor

As explained in chapter. 6 (sec. 6.3.2 and sec. 6.5), the COM displacement spectra obtained (fig. 8.3) via Bragg spectroscopy of the trapped degenerate gas probe the dynamic structure factor (DSF). To show this, the Bragg response function (COM displacement) is calculated from eq. 6.37, for both an ideal Bose gas and an ideal Fermi gas at zero temperature, using eq. 6.14 under the impulse approximation (large q). This equation can be written as

$$S(q,\delta) = \frac{m}{q}\int dp_y dp_z n(p_x, p_y, p_z), \tag{8.2}$$

where the excitation with wavevector q is assumed to be oriented along the x-direction, $p_x = m(E - E_r)/q$ and E_r is the single photon recoil energy.

For the case of a zero temperature BEC, in the TF approximation, the momentum distribution is given by [54]

$$n_{\mathrm{TF}}(p) = N\frac{15}{16\lambda}\left(\frac{\sigma_x}{\hbar}\right)^3\left[\frac{J_2(\tilde{p})}{\tilde{p}^2}\right]^2, \tag{8.3}$$

where $\lambda = \omega_z/\omega_x$, $J_2(z)$ is the second order Bessel function, σ_x is the TF radius and $\tilde{p} = \sqrt{p_x^2 + p_y^2 + (p_z/\lambda)^2}\ \sigma_x/\hbar$ is a dimensionless momentum. For simplicity, when comparing with data, the dominant peak of the $J_2(z)$ is well approximated by a

Gaussian function and the value of the integral becomes

$$S_{\text{Bosons}}(q,\delta) = A\frac{m}{q}e^{-\frac{p_x^2(\delta)}{2\sigma^2}}, \tag{8.4}$$

where A is the amplitude and σ is the approximate width of the Bessel function.

For the case of an ideal Fermi gas at zero temperature, the momentum distribution is

$$n(p_x,p_y,p_z) = \frac{8}{\pi^2}\frac{N}{p_{\text{F}}^3}\text{Max}\left[\left(1-\frac{p_x^2+p_y^2+p_z^2}{p_{\text{F}}^2}\right)^{3/2},0\right], \tag{8.5}$$

where $p_{\text{F}} = \hbar k_F$ is the Fermi momentum. Substituting this expression for the integrand in eq. 8.2, the value of the integral becomes

$$S_{\text{Fermions}}(q,\delta) = \frac{16\left(p_{\text{F}}^2 - p_x^2(q,\delta)\right)^{\frac{5}{2}}}{5\pi p_{\text{F}}^6} \tag{8.6}$$

The Bragg spectrum of a bosonic molecular condensate at 750 G is compared to the Bragg response function for bosons using eq. 8.4 and the spectrum of a weakly interacting Fermi gas at 990 G is compared to the Bragg response function for fermions

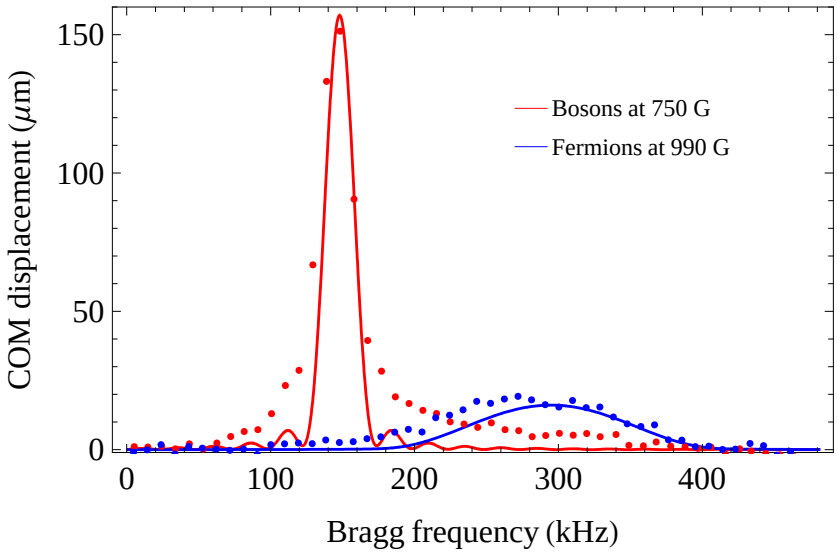

Figure 8.5: Comparison of the measured and calculated Bragg responses of bosons and fermions.

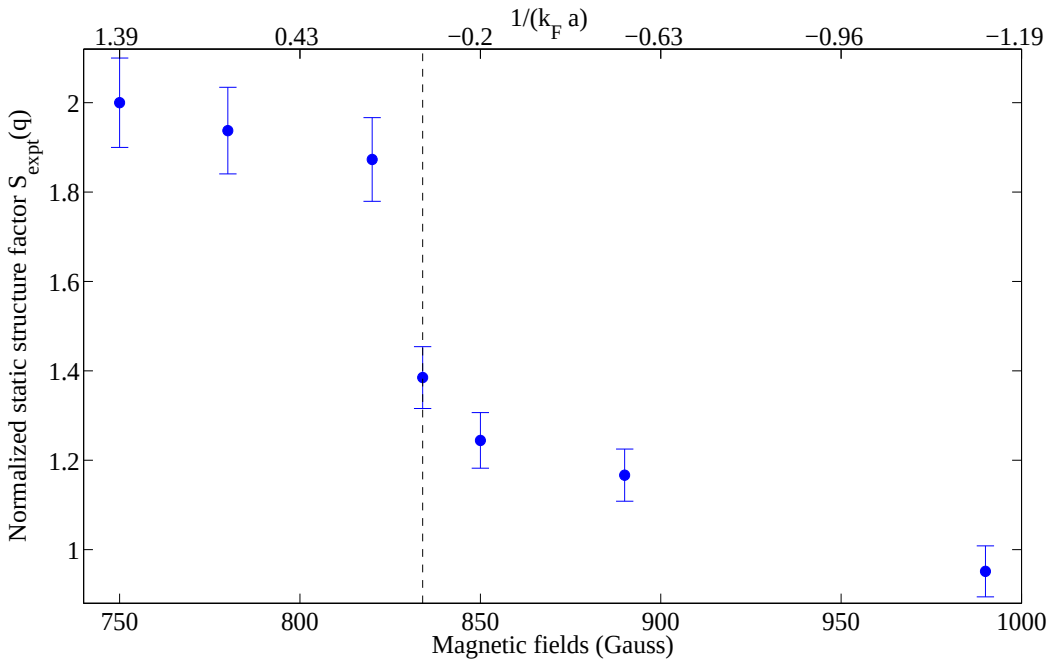

Figure 8.6: Evaluated experimental static structure factor across the BEC-BCS crossover. The vertical dotted line indicates the position of the Feshbach resonance.

using eq. 8.6, as shown in fig. 8.5. The relative heights of the calculated responses are set by the requirement that the area under the bosonic curve be equal to twice that of the fermionic curve [51]. Both the amplitudes and widths of the experimental data show good agreement with the limiting case theory when $|1/k_{\mathrm{F}}a| > 1$. The width of the molecular peak is limited experimentally by the Fourier width of the Bragg pulse (20 kHz) and the background signal is due to off-resonant scattering of free thermal atoms.

Thus, by definition, the static structure factor (SSF) can be evaluated by integrating the area under the spectra at different magnetic fields. These values are normalised in such a way that $S_{expt}(q = 5k_{\mathrm{F}}) = 2$ corresponding to the bound molecular BEC-limit at 750 G, which ensures $S_{expt}(q = 5k_{\mathrm{F}}) = 1$ corresponding to the BCS-limit at 990 G. The results are presented in fig. 8.6 and are qualitatively in good agreement with the theoretical simulations given in reference [51], where the SSF varies monotonically from 2 on the BEC side to 1 on the BCS side. Quantitatively, however, there is a difference

between the measured and calculated values of the SSF. For example, $S_{expt} = 2$ for an interaction parameter $1/k_{\mathrm{F}}a = 1.39$ whereas in the simulations $S = 2$ only for values $1/k_{\mathrm{F}}a > 4$[1]. This difference may be due to the fact that k_{F} in the experimental (trapped) case refers to the Fermi wavevector at the peak cloud density, and away from the trap centre the local Fermi wavevector decreases as $k_{\mathrm{F}} = (6\pi^2 n(r))^{1/3}$. Therefore, a density average of the interaction parameter would be higher than the quoted $1/k_{\mathrm{F}}a$; so it is expected that a trapped gas would approach ideal molecular behaviour more rapidly than a uniform gas with the same $1/k_{\mathrm{F}}a$. However, proper theoretical modelling of the trapped case would be very insightful. In summary, these measurements of $S(q)$ confirm the decay of two-body pair correlations $g^{(2)}_{\uparrow\downarrow}(z)$ from the BEC to BCS side of the Feshbach resonance with a finite value present at unitarity.

8.5 Density dependence of pair scattering

At unitarity and above the Feshbach resonance, on the BCS side, correlated pairs exist due to many-body effects in the strongly interacting gas [38]. These interactions in principle depend on the density of the system. When the density of the gas is decreased, the interactions (elastic collisions) and the pair correlations also decrease. To verify this, Bragg scattering is performed across the BEC-BCS crossover at various magnetic fields whilst varying the density of the interacting gas. This is achieved by varying the expansion time of the gas after releasing from the trap, before applying a Bragg pulse and keeping the same time of flight for imaging. The Bragg frequency is chosen to be resonant with pairs/molecules and kept constant at $\delta/2\pi$=145 kHz. The momentum imparted to the gas is measured again via the centre of mass displacement (COM) of the entire distribution of the gas. The density of the gas is calculated from the reference images that are taken for each time of flight (*i.e.,* without applying a

[1]Note that, if the experimental data is normalized on one side of the Feshbach resonance to the theoretical value, to overcome this difference, then the data would disagree on the other side

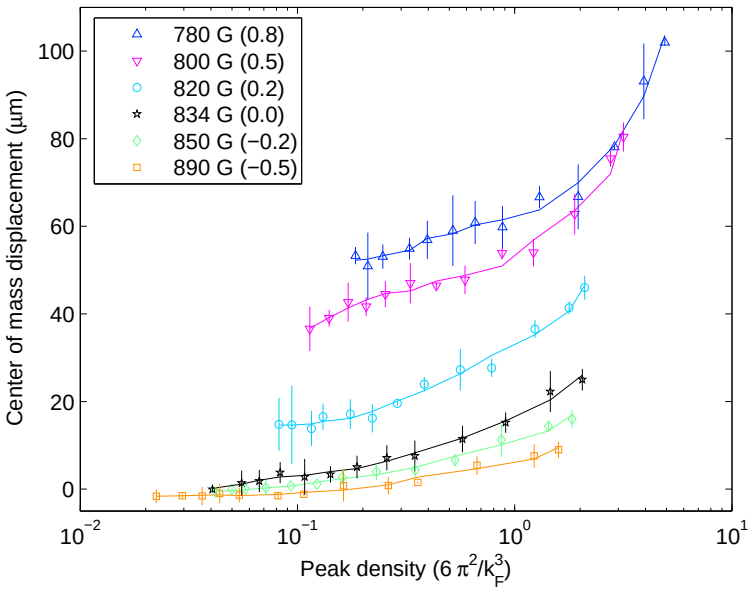

Figure 8.7: Density dependence of the molecules and correlated pairs across the BEC-BCS crossover. The interaction strength $1/k_F a$ is given in brackets.

Bragg pulse). In doing so, the appropriate scaling factors are taken into account to include the effect of the saddle magnetic potential produced by our Feshbach coils on the expanding gas (see sec. 2.5). The density is expressed in units of $6\pi^2/k_F^3$ and is always greater than unity because of the interactions.

Figure 8.7 shows the measured COM displacement dependence on the density of the interacting gas across the crossover. On the BEC side (780 G, 800 G and 820 G), at high density, tightly bound molecules are displaced to a large distance which is observed to gradually decrease towards an asymptotic value as the density is lowered. This is due to fewer and fewer molecules becoming resonant with the Bragg pulse as the mean field energy is converted into kinetic energy during expansion of the cloud. The fact that this signal is approaching a non-zero asymptotic value implies that the scattered particles are true bound molecules in the low density limit.

On the other hand, at unitarity (834 G) and near the BCS side (850 G and 890 G) of the Feshbach resonance, a pair scattering signal (COM displacement) is observed only at high densities and the signal is observed to gradually approach zero at low densities.

This behaviour highlights the importance of density dependent correlations among the pairs. Since no stable bound two particle states exist at these magnetic fields, it can be interpreted as scattering of correlated pairs which only exists in a strongly interacting many-body system at these temperatures. These observations establish a means to distinguish true bound molecules from many body pairs.

In a trapped two-component unitary Fermi gas, elastic collisions are limited by Pauli blocking at low temperatures. For $T/T_F \leq 0.15$ the collision rate can be estimated from $\gamma_{el} = \frac{41E_\mathrm{F}}{3\pi\hbar}\left(\frac{T}{T_\mathrm{F}}\right)^2$ [98]. For our parameters, at a temperature $T/T_\mathrm{F} = 0.06$, this value is evaluated as $\tau_{el} = \gamma_{el}^{-1} = 1$ ms. This is much longer than the Bragg pulse duration of 40 μs and supports the idea that pre-existing pairs are scattered rather than pairs which associate via collisions during the Bragg pulse. Elastic collisions may actually increase during expansion [99] but no increase in the scattered signal is observed in our data.

8.6 Thermometry of a strongly interacting gas

The measured pair correlations presented in section 8.4 need to be quantified in terms of the temperature. At unitarity, although the interactions among opposite spin fermions are strong, pairing does not start until below the characteristic temperature T^*. When the gas is further cooled to temperatures below the critical temperature T_C, the pairs start to condense and show the signature of superfluidity. Both T^* and T_C vary as a function of the interaction parameter $1/k_\mathrm{F}a$ along the BEC-BCS crossover as shown in Fig. 1.1. Therefore, it is important to quantify whether the measured density correlations are in this superfluid regime or not.

Measuring the temperature of a strongly interacting Fermi gas is not straightforward as there exists no universally agreed theory that explains the physics of the BEC-BCS crossover regime completely. Experimentally, the temperature of an

interacting Fermi gas with equal spin population[2] can be measured indirectly by two different methods [100]. In one method [23, 101], the interaction strength of a strongly interacting gas is isentropically ramped to a very weakly interacting value by sweeping the magnetic field adiabatically far away from the Feshbach resonance. The temperature is then deduced by fitting spatial profiles of a non-interacting Fermi gas to the measured density distribution (column density) from time of flight absorption images.

The other method [31] is used to obtain an empirical temperature $\tilde{T}$ by fitting the density profile of a non-interacting gas to the measured density distribution of a strongly interacting gas. This method is applicable only at unitarity where the equation of state ($\mu \propto n^{2/3}$) has the same form as for non-interacting fermions [30]. Once $\tilde{T}$ is obtained, it is calibrated to the true physical temperature T using a model dependent theoretical density profile. In the following section, this method is used to obtain the temperature at unitarity.

8.6.1 Obtaining temperature from density distributions

An absorption image gives a two-dimensional column density, *i.e.,* the density distribution integrated along the direction of the resonant laser beam (see fig. 8.8a). This image is then integrated along the axial direction to avoid the insensitivity of the two-dimensional fit routine to the trap anharmonicity in the axial direction [31]. This 1D-density distribution (fig. 8.8b) is then normalized before fitting a theoretical profile to obtain the empirical temperature.

Fitting procedure for a weakly interacting gas

The fitting function used for the 1D-density profile of a non-interacting Fermi gas

[2]For unequal spin populations, the temperature is obtained by fitting a non-interacting spatial profile to the tail of the measured density distribution. However, the deviation of the interacting gas from the non-interacting profile is very small ($< 2\%$) [72], making it a difficult choice.

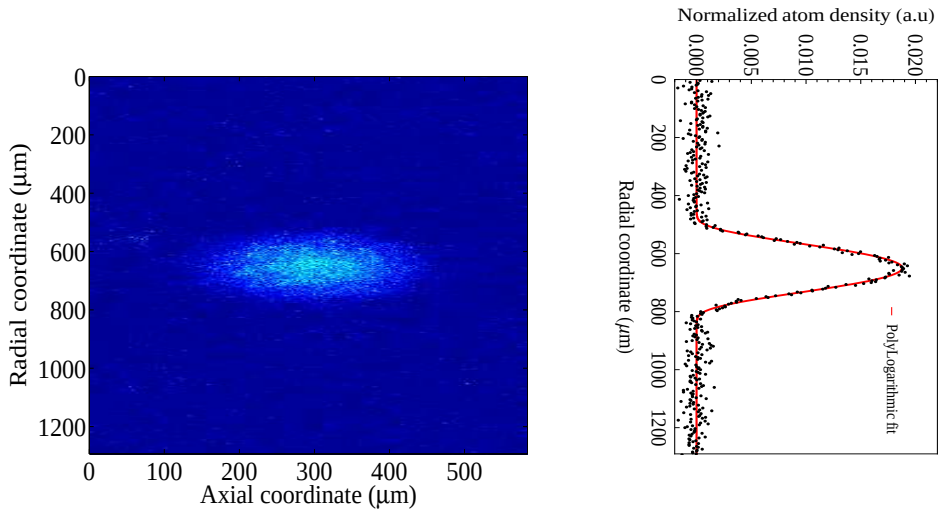

(a) Absorption image at 834 G.

(b) Integrated image(a) along the axial direction

Figure 8.8: Obtaining 1D-density profile from an absorption image (TOF = 4 ms). The temperature of the gas is obtained from the Polylogarithmic fit as T/T_{F}=0.06.

is given by [102]

$$n(x,T) = -\frac{3N}{\sqrt{\pi}\sigma_x}\left(\frac{T}{T_{\mathrm{F}}}\right)^{\frac{5}{2}} Li_{5/2}\left[-\exp\left(\frac{\frac{\mu}{E_{\mathrm{F}}} - \frac{x^2}{\sigma_x^2}}{T/T_{\mathrm{F}}}\right)\right], \tag{8.7}$$

where $Li_{5/2}$ is the polylogarithm function, μ is the chemical potential and σ_x is the Thomas-Fermi (TF) radius in the radial direction. Given that the number of atoms N can be measured from the absorption images, there are only three parameters (μ, σ_x and T) left for the fit. For a Fermi gas the value of μ determines the shape of the cloud, whereas σ_x and T appear as a product in the argument of the exponential ($\sigma_x^2\ T/T_{\mathrm{F}}$). If σ_x is known by other means then the temperature can be used as an independent fit parameter.

For this reason, σ_x is first determined by fitting a zero temperature 1D-Thomas-Fermi profile

$$n_{1D}(x) = \frac{16N}{5\pi\sigma_x}\left(1 - \frac{x^2}{\sigma_x^2}\right)^{\frac{5}{2}} \tag{8.8}$$

to the lowest temperature clouds achievable in our experiment. The profile is fitted

only to the central region of the clouds (excluding the wings) to obtain σ_x. This is a valid approximation as finite temperature effects in a Fermi gas mostly affect its wings [73, 74]. This procedure is different from the one mentioned in the thesis [102] where the full profile is fitted for a non-interacting Fermi gas to obtain σ_x. For a fixed trapping frequency ω_x, the TF radius is written as

$$\sigma_x = \sqrt{\frac{2E_{\rm F}}{m\omega_x^2}} = \sqrt{\frac{2(6)^{\frac{1}{3}}\hbar\bar{\omega}}{m\omega_x^2}} \left(\frac{N}{2}\right)^{\frac{1}{6}} = C_x \left(\frac{N}{2}\right)^{\frac{1}{6}}, \tag{8.9}$$

where C_x is a constant. Initially, an average value for C_x is obtained from a number of absorption images and from that an average value for σ_x is obtained. Once the value for σ_x is obtained from the 1D-TF fits, it is fixed for all higher temperatures leaving $T/T_{\rm F}$ as a free parameter in eq. 8.7.

Fitting procedure for a strongly interacting gas

The fitting procedure in this case is similar to that of the weakly interacting gas as mentioned above, except that the Fermi radius σ_x and Fermi temperature $T_{\rm F}$ should be replaced by their unitarity values σ_x^* and $T_{\rm F}^*$, respectively. At unitarity, $\sigma_x^* = (1+\beta)^{1/4}\sigma_x$ and $T_{\rm F}^* = (1+\beta)^{1/2}T_{\rm F}$, where β is a universal constant, and the fitting profile becomes

$$n(x,T) = -\frac{3N}{\sqrt{\pi}\sigma_x^*}\left(\tilde{T}\right)^{\frac{5}{2}} Li_{5/2}\left[-\exp\left(q - \frac{x^2}{(\sigma_x^*)^2\tilde{T}}\right)\right], \tag{8.10}$$

where $q = \frac{\mu}{E_{\rm F}\tilde{T}}$ determines the shape of the strongly interacting Fermi gas at unitartiy and $\tilde{T}$ is the reduced/empirical temperature given by

$$\tilde{T} = \frac{T}{T_{\rm F}\sqrt{1+\beta}}. \tag{8.11}$$

Similar to the weakly interacting case, the value of σ_x^* is obtained by fitting a zero temperature 1D-TF profile (n_{1D}) for the lowest temperature clouds achievable in our experiment, and then fixing this value constant for the fits at all higher temperatures

leaving only $\tilde{T}$ and q as the free parameters. The empirical temperature, at unitarity, for the lowest trap depth achievable in our experiment is obtained as $\tilde{T} = 0.1$. Thus the true temperature at unitarity is approximately $T/T_F = 0.06$ for $\beta = -0.56$ [23, 31, 72]. The fit is shown in fig. 8.9 along with an equivalent Maxwell-Boltzmann classical gas at the same temperature for comparison. The peak of the Fermi-Dirac (polylogarithmic) fit has a flat top whereas it is sharp for the classical gas (Gaussian fit). This is due to the Fermi pressure at the centre of the trap where the density is high.

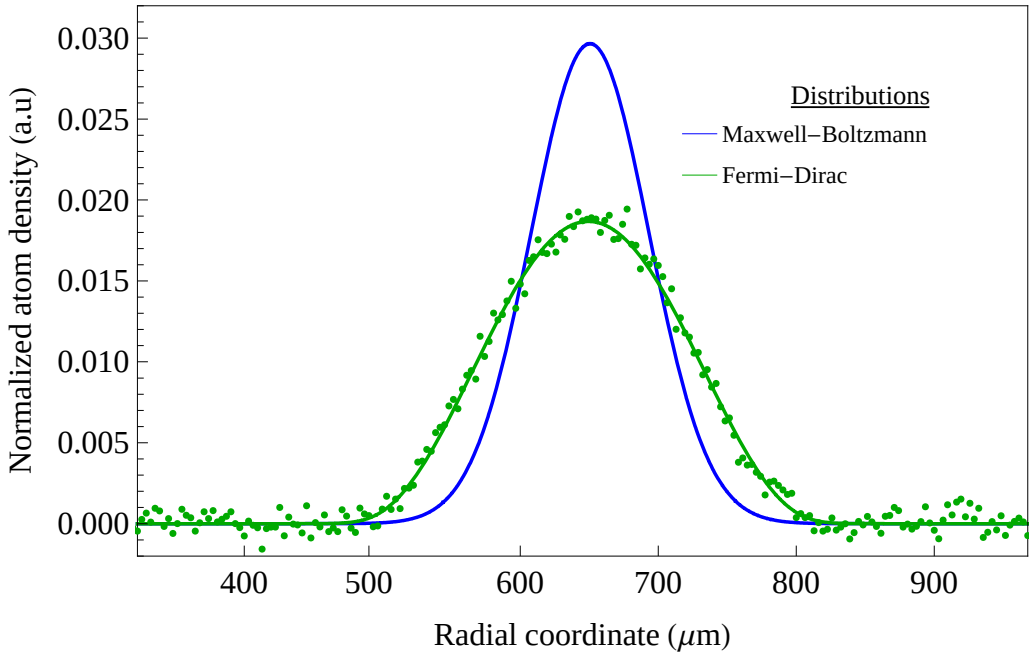

Figure 8.9: 1D Polylogarithmic fit to the data (TOF = 4 ms). For comparison a Gaussian distribution for the same temperature (T/T_F=0.06) is shown.

Comparison with isentropic magnetic field sweeps

The temperature obtained from the fitting functions can be verified by comparing it with the values evaluated following an isentropic sweep of the magnetic field [23]. This technique also gives a rough estimate of the temperature at magnetic fields other than unitarity (834 G). First, a sample of a strongly interacting Fermi gas is created at the desired magnetic field by evaporatively cooling it to the lowest trap depth (2 μK) achievable in our dipole trap and then adiabatically (15 ms) ramping to the BEC side of the Feshbach resonance. The temperature is then obtained by calculating the

condensate fraction at that magnetic field by fitting a bimodal (Thomas-Fermi and Gaussian) distribution to the expanded cloud. Using a model independent theory [103], these temperatures are calibrated against those of an interacting Fermi gas to obtain the final T/T_{F} values.

Thus, from the estimated T/T_{F} temperatures of a Fermi gas at unitarity (834 G) , the results of sec. 8.4 should be well below the superfluid transition temperature. Even above 834 G, the data should be in the superfluid regime according to the isentropic sweep predictions [104, 105, 106].

8.7 Summary

The first comprehensive Bragg spectroscopic study of a strongly interacting Fermi gas is presented in this chapter. A smooth transition from molecular to atomic spectra is observed with a clear signature of pairing at and above unitarity. These pair correlations are quantified by measuring the static structure factor across the BEC-BCS crossover. The features of these results qualitatively agree with the theoretically calculated values [51], using quantum Monte-Carlo simulations. Quantitative agreement is difficult to obtain as the calculations are performed for a uniform gas, whereas the experiments are carried out in a trapped gas, whose density varies across the trap. The correlated pair signal observed in the Bragg spectra, at magnetic fields at and above unitarity, is seen to decay as the density is lowered. However, the same signal on the BEC side is seen to approach a non-zero asymptotic value, as the density is lowered, which indicates the presence of true bound molecules.

Chapter 9

Summary and conclusions

In this thesis, an experimental investigation of pair correlations in a strongly interacting ^{6}Li Fermi gas via Bragg spectroscopy is presented. In the process, our earlier experimental set-up [64] was upgraded by including a tapered amplifier to create a six-beam MOT, setting up offset-locking for taking absorption images at high magnetic fields and setting up a high power (100 W) fibre laser for the single beam optical dipole trap. The main advantage of the new experimental set-up is the ability to perform absorption imaging continuously at any magnetic field across the BEC-BCS crossover which is achieved by the offset-locking of two master lasers. These improvements not only increased the trapped atom number in the dipole trap but also offered a powerful tool to directly probe the strongly interacting regime smoothly from the BEC to the BCS side of the Feshbach resonance. The Bragg spectra presented in this thesis are taken from single runs of the experiment with no averaging of the data. This reflects the robust nature of the physics and also the stability of our experimental setup. A summary of the main achievements of this investigation is given below.

9.1 Summary of the results

Production of degenerate quantum gases:

Our group has produced a molecular BEC of ^{6}Li dimers, initially in two different dipole trap geometries, viz., crossed and elongated crossed dipole traps using a low power (22 W) Yb:YAG thin disc laser (ELS VersaDisk 1030-20 SF) [66]. Subsequently, a high power (100 W) fibre laser (*IPG-Photonics*, YLR-100) was introduced to create a single dipole trap. The large initial trap depth (3 mK) from this laser and the loading of atoms from the six-beam MOT made it possible to achieve a high initial phase space density. Evaporative cooling is performed near the broad s-wave Feshbach resonance at 834 G. Due to three-body recombination at low temperatures, molecules are formed on the BEC side of the resonance and further evaporation led to the creation of a molecular BEC. When this condensate was isentropically ramped to the BCS side, a strongly or weakly interacting Fermi gas is created depending on the final magnetic field (scattering length).

Implementation of Bragg spectroscopy:

For the first time, Bragg spectroscopy was performed on a strongly interacting gas to probe the composition of the particles and pair correlations, across the BEC-BCS crossover. The momentum imparted to the gas was quantified based on the centre of mass (COM) displacement. Both the low density (collisionless regime) and the high density (interacting regime) clouds were subjected to Bragg scattering with high momentum transfer ($q \simeq 5k_F$) to probe free particle excitations across the crossover. In the collisionless regime, two-photon Rabi oscillations were measured both for molecules and atoms. In the interacting regime, the Bragg spectra revealed information about the dynamic and static structure factors.

Measurement of the structure factors:

In chapter. 6, the relation between the density correlations and structure factors was presented and the connection with the experimentally measured COM displacement was made. The dynamic structure factor (DSF) $S(q, \delta)$ gives a direct measure of elementary excitations, whereas the static structure factor (SSF) $S(q)$ gives information about pair correlations in an interacting gas. The DSFs of a molecular condensate and a weakly interacting degenerate Fermi gas were obtained and compared with an ideal gas at zero temperature. Good agreement between the measurements and theory was found. From these measurements the SSF was determined across the BEC-BCS crossover and the pair density correlations were quantified. These correlations were found to decay smoothly from the BEC regime to the BCS regime in qualitative agreement with theory (quantum Monte-Carlo simulations).

Verification of the density dependence:

The fact that correlated pairs can exist only in a strongly interacting many-body system was verified by Bragg spectroscopy. The Bragg signal (COM displacement) of the scattered pairs was found to gradually decrease from high density to low density clouds, eventually approaching zero. However, for bound molecules, this signal approached a non-zero asymptotic value indicating scattering of molecules as free particles. These observations establish the density dependence of pair correlations in a strongly interacting gas.

9.2 Outlook

The excitation spectrum: All of the experiments described in this thesis were performed by keeping the momentum q imparted to the gas constant and large. This allowed the exploration of only a small region of free particle excitations in the gas. If the angle between the two Bragg beams is varied then the value of q can be varied from

below k_F to above. Such a variation would allow access to the phonon regime. In the case of fermions, this could provide explicit detection of the superfluid gap. In addition, since pair correlations are related to the structure factor via a Fourier transform, the explicit pair correlation function can be obtained experimentally.

Detection of the particles: In this thesis, Bragg spectroscopy was used as a tool to distinguish between molecules (on the BEC side) and correlated pairs (at unitarity). Similarly, one can use this tool to detect the presence of Cooper pairs in a weakly interacting Fermi gas [62]. The same technique can also be used to detect p-wave molecules in 3D or 2D quantum gases. This work is in progress in our laboratory [81].

Mean-field broadening and shifts: Interactions in a condensate give rise to a mean-field shift of the Bragg resonant frequency and broadens the peak response. Ketterle's group at MIT has extensively studied the effect of mean-field interactions in atomic BECs [88] and on ultra-cold molecules [63]. Their work showed a surprisingly large shift in the Bragg resonant frequency, which could not be explained simply on the basis of mean-field effects. Meanwhile, no work has been reported on molecular condensates near the strongly interacting regime. Because ^{6}Li has a broad Feshbach resonance at 834 G, the scattering length can be varied smoothly and these effects could be studied more systematically.

Properties of pair correlations: In this work we have observed the density dependence of pairs at and above unitarity. Interestingly, the Bragg signal in this region was found to reach zero around the same density value for various magnetic fields (see fig. 8.7). This implies that further study is necessary to determine whether there is a critical density for many-body interactions to come into effect for pair formation. Also, we have quantified the SSF only for trapped (high density) gases across the BEC-BCS crossover. One can extend this for various densities to quantify the density dependence of the SSF, and hence the pair correlations. Finally, the SSF was measured only for the lowest temperature available in our set-up. This can be measured again for various temperatures to determine the temperature dependence of pairing.

Signature of superfluidity: Currently, we are working on the possibility of using the Bragg signal as a signature for superfluidity. Preliminary data taken by varying the temperature of the gas has shown a large COM displacement below the critical temperature (T_C) of the gas at unitarity. Once the temperature of the gas is measured accurately, one can even look only for the pairing signature above T_C and below T^*, the characteristic temperature for pairing (see fig. 1.1).

Retracing the phase-space diagram: A long-standing goal of the BEC-BCS crossover physics is to retrace the phase-space diagram experimentally across the crossover regime. If the signature of superfluidity can be verified by Bragg spectroscopy, as mentioned above, then one can obtain T_C and T^* experimentally at various magnetic fields. This is possible in our set-up as we can perform absorption imaging continuously at any magnetic field across the crossover. However, we still need to work on evaluating the temperatures accurately not only at unitarity but throughout the crossover where new theoretical models are needed.

Bibliography

[1] C. A. Regal, C. Ticknor, J. L. Bohn, and D. S. Jin. Creation of ultracold molecules from a Fermi gas of atoms. *Nature*, 424:47, 2003.

[2] C. A. Regal, M. Greiner, and D. S. Jin. Lifetime of Molecule-Atom Mixtures near a Feshbach Resonance in K. *Phys. Rev. Lett.*, 92:083201, 2004.

[3] J. Cubizolles, T. Bourdel, S. J. J. M. F. Kokkelmans, G. V. Shlyapnikov, and C. Salomon. Production of Long-Lived Ultracold Li_2 Molecules from a Fermi Gas. *Phys. Rev. Lett.*, 91:240401, 2003.

[4] Kevin E. Strecker, Guthrie B. Partridge, and Randall G. Hulet. Conversion of an Atomic Fermi Gas to a Long-Lived Molecular Bose Gas. *Phys. Rev. Lett.*, 91:080406, 2003.

[5] S. Jochim, M. Bartenstein, A. Altmeyer, G. Hendl, C. Chin, J. Hecker Denschlag, and R. Grimm. Pure Gas of Optically Trapped Molecules Created from Fermionic Atoms. *Phys. Rev. Lett.*, 91:240402, 2003.

[6] S. Jochim, M. Bartenstein, A. Altmeyer, G. Hendl, S. Riedl, C. Chin, J. Hecker Denschlag, and R. Grimm. Bose-Einstein Condensation of Molecules. *Science*, 302:2101–2103, 2003.

[7] M. Greiner, C. A. Regal, and D. S. Jin. Emergence of a molecular Bose Einstein condensate from a Fermi gas. *Nature*, 426:537, 2003.

[8] M. W. Zwierlein, C. A. Stan, C. H. Schunck, S. M. F. Raupach, S. Gupta, Z. Hadzibabic, and W. Ketterle. Observation of Bose-Einstein Condensation of Molecules. *Phys. Rev. Lett.*, 91:250401, 2003.

[9] H. Feshbach. Unified theory of nuclear reactions. II. *Annals of Physics*, 19:287, 1962.

[10] E. Tiesinga, B. J. Verhaar, and H. T. C. Stoof. Threshold and resonance phenomena in ultracold ground-state collisions. *Phys. Rev. A*, 47:4114–4122, 1993.

[11] S. Inouye, M. R. Andrews, J. Stenger, H.-J. Miesner, D. M. Stamper-Kurn, and W. Ketterle. Observation of Feshbach resonances in a Bose-Einstein condensate. *Nature*, 392:151, 1998.

[12] Ph. Courteille, R. S. Freeland, D. J. Heinzen, F. A. van Abeelen, and B. J. Verhaar. Observation of a Feshbach Resonance in Cold Atom Scattering. *Phys. Rev. Lett.*, 81:69–72, 1998.

[13] S. Chu, L. Hollberg, and J. E. Bjorkholm. Three-dimensional viscous confinement and cooling of atoms by radiation pressure. *Phys. Rev. Lett.*, 55:48, 1985.

[14] Steven Chu, J. E. Bjorkholm, A. Ashkin, and A. Cable. Experimental Observation of Optically Trapped Atoms. *Phys. Rev. Lett.*, 57:314, 1986.

[15] P. D. Lett, R. N. Watts, C. I. Westbrook, and W. D. Phillips. Observation of Atoms Laser Cooled below the Doppler Limit. *Phys. Rev. Lett.*, 61:169, 1988.

[16] E. Raab, M. Prentiss, A. Cable, S. Chu, and D. Pritchard. Trapping of Neutral-Sodium Atoms with Radiation Pressure. *Phys. Rev. Lett.*, 59:2631, 1987.

[17] M. H. Anderson, J. R. Ensher, M. R. Matthews, C. E. Wieman, and E. A. Cornell. Observation of Bose-Einstein Condensation in a Dilute Atomic Vapor. *Science*, 269:198, 1995.

[18] K. B. Davis, M.-O. Mewes, M. R. Andrews, N. J. van Druten, D. S. Durfee, D. M. Kurn, and W. Ketterle. Bose-Einstein Condensation in a Gas of Sodium Atoms. *Phys. Rev. Lett.*, 75:3969, 1995.

[19] C. C. Bradley, C. A. Sackett, J. J. Tollett, and R. G. Hulet. Bose-Einstein Condensation in an Atomic Gas with Attractive Interactions. *Phys. Rev. Lett.*, 75:1687, 1995.

[20] C. A. Regal, M. Greiner, and D. S. Jin. Observation of Resonance Condensation of Fermionic Atom Pairs. *Phys. Rev. Lett.*, 92:040403, 2004.

[21] M. Zwierlein, C. A. Stan, C. H. Schunck, S. M. F. Raupach, A. J. Kerman, and W. Ketterle. Condensation of Pairs of Fermionic Atoms near a Feshbach Resonance. *Phys. Rev. Lett.*, 92:120403, 2004.

[22] C. Chin, M. Bartenstein, A. Altmeyer, S. Riedl, S. Jochim, J. Hecker Denschlag, and R. Grimm. Observation of the Pairing Gap in a Strongly Interacting Fermi Gas. *Science*, 305:1128–1130, 2004.

[23] M. Bartenstein, A. Altmeyer, S. Riedl, S. Jochim, C. Chin, J. Hecker Denschlag, and R. Grimm. Crossover from a Molecular Bose-Einstein Condensate to a Degenerate Fermi Gas. *Phys. Rev. Lett.*, 92:120401, 2004.

[24] T. Bourdel, L. Khaykovich, J. Cubizolles, J. Zhang, F. Chevy, M. Teichmann, L. Tarruell, S. J. J. M. F. Kokkelmans, and C. Salomon. Experimental Study of the BEC-BCS Crossover Region in Lithium 6. *Phys. Rev. Lett.*, 93:050401, 2004.

[25] J. Kinast, S. L. Hemmer, M. E. Gehm, A. Turlapov, and J. E. Thomas. Evidence for Superfluidity in a Resonantly Interacting Fermi Gas. *Phys. Rev. Lett.*, 92:150402, 2004.

[26] G. B. Partridge, K. E. Strecker, R. I. Kamar, M. W. Jack, and R. G. Hulet. Molecular Probe of Pairing in the BEC-BCS Crossover. *Phys. Rev. Lett.*, 95:020404, 2005.

[27] H. K. Onnes. On the sudden rate at which the resistance of mercury disappears. *Akad. van Wetenschappen*, 14(113):818, 1911.

[28] D. D. Osheroff, R. C. Richardson, and D. M. Lee. Evidence for a new phase of solid He^3. *Phys. Rev. Lett.*, 28:885, 1972.

[29] A. Perali, P. Pieri, L. Pisani, and G. C. Strinati. BCS-BEC Crossover at Finite Temperature for Superfluid Trapped Fermi Atoms. *Phys. Rev. Lett.*, 92(22):220404, 2004.

[30] W. Ketterle and M. W. Zwierlein. *Making, probing and understanding ultracold Fermi gases, Proceedings of the International School of Physics Enrico Fermi, Varenna, 20-30 June 2006*. IOS press, Amsterdam, 2007.

[31] J. Kinast, A. Turlapov, J. E. Thomas, Q. Chen, J. Stajic, and K. Levin. Heat Capacity of a Strongly Interacting Fermi Gas. *Science*, 307:1296–1299, 2005.

[32] J. E. Thomas, J. Kinast, and A. Turlapov. Virial Theorem and Universality in a Unitary Fermi Gas. *Phys. Rev. Lett.*, 95:120402, 2005.

[33] L. Luo, B. Clancy, J. Joseph, J. Kinast, and J. E. Thomas. Measurement of the Entropy and Critical Temperature of a Strongly Interacting Fermi Gas. *Phys. Rev. Lett.*, 98:080402, 2007.

[34] J. T. Stewart, J. P. Gaebler, C. A. Regal, and D. S. Jin. Potential Energy of a ^{40}K Fermi Gas in the BCS-BEC Crossover. *Phys. Rev. Lett.*, 97:220406, 2006.

[35] Guthrie B. Partridge, Wenhui Li, Ramsey I. Kamar, Y. Liao, and Randall G. Hulet. Pairing and Phase Separation in a Polarized Fermi Gas. *Science*, 311:503–505, 2006.

[36] Hui Hu, Xia-Ji Liu, and P. D. Drummond. Universal thermodynamics of strongly interacting Fermi gases. *Nature Physics*, 3:469, 2007.

[37] J. G. Bednorz and K. Mueller. Possible high-Tc superconductivity in the Ba-La-Cu-O system. *Z. Physik B*, 64:189, 1986.

[38] J. Bardeen, L. N. Cooper, and J. R. Schriffer. Theory of Superconductivity. *Phys. Rev.*, 108:1175, 1957.

[39] D. S. Petrov, C. Salomon, and G. V. Shlyapnikov. Weakly Bound Dimers of Fermionic Atoms. *Phys. Rev. Lett.*, 93:090404, 2004.

[40] C. H. Schunck, Y. Shin, A. Schirotzek, and W. Ketterle. Determination of the fermion pair size in a resonantly interacting superfluid. *Nature*, 454:739, 2008.

[41] André Schirotzek, Yong il Shin, Christian H. Schunck, and Wolfgang Ketterle. Determination of the superfluid gap in atomic fermi gases by quasiparticle spectroscopy. *Physical Review Letters*, 101:140403, 2008.

[42] M. W. Zwierlein, J. R. Abo-Shaeer, A. Schirotzek, C. H. Schunck, and W. Ketterle. Vortices and superfluidity in a strongly interacting Fermi gas. *Nature*, 435:1047, 2005.

[43] M. W. Zwierlein, C. H. Schunck, A. Schirotzek, and W. Ketterle. Direct observation of the superfluid phase transition in ultracold Fermi gases. *Nature*, 442:54, 2006.

[44] C. H. Schunck, M. W. Zwierlein, A. Schirotzek, and W. Ketterle. Superfluid Expansion of a Rotating Fermi Gas. *Phys. Rev. Lett.*, 98:050404, 2007.

[45] C. H. Schunck, Y. I. Shin, A. Schirotzek, and W. Ketterle. Determination of the fermion pair size in a resonantly interacting superfluid. *Nature*, 454(7205):739–U70, 2008.

[46] S. Gupta, Z. Hadzibabic, M. W. Zwierlein, C. A. Stan, K. Dieckmann, C. H. Schunck, E. G. M. van Kempen, B. J. Verhaar, and W. Ketterle. Radio-frequency spectroscopy of ultracold fermions. *Science*, 300(5626):1723–1726, 2003.

[47] C. Chin, M. Bartenstein, A. Altmeyer, S. Riedl, S. Jochim, J. H. Denschlag, and R. Grimm. Observation of the pairing gap in a strongly interacting fermi gas. *Science*, 305(5687):1128–1130, 2004.

[48] J. T. Stewart, J. P. Gaebler, and D. S. Jin. Using photoemission spectroscopy to probe a strongly interacting fermi gas. *Nature*, 454(7205):744–747, 2008.

[49] M. Greiner, C. A. Regal, J. T. Stewart, and D. S. Jin. Probing pair-correlated fermionic atoms through correlations in atom shot noise. *Physical Review Letters*, 94(11):–, 2005.

[50] H. P. Büchler, P. Zoller, and W. Zwerger. Spectroscopy of superfluid pairing in atomic fermi gases. *Phys. Rev. Lett.*, 93:080401, 2004.

[51] R. Combescot, S. Giorgini, and S. Stringari. Molecular signatures in the structure factor of an interacting Fermi gas. *Europhys. Lett*, **75**:695, 2006.

[52] G. M. Bruun and Gordon Baym. Bragg spectroscopy of cold atomic fermi gases. *Phys. Rev. A*, 74:033623, 2006.

[53] D. Pines and P. Nozieres. *The Theory of Quantum Liquids*. Benjamin, New York, 1966.

[54] F. Zambelli, L. Pitaevskii, D. M. Stamper-Kurn, and S. Stringari. Dynamic structure factor and momentum distribution of a trapped Bose gas. *Phys. Rev. A*, **61**:063608, 2000.

[55] A. Brunello, F. Dalfovo, L. Pitaevskii, S. Stringari, and F. Zambelli. Momentum transferred to a trapped Bose-Einstein condensate by stimulated light scattering. *Phys. Rev. A*, **64**:063614, 2001.

[56] P. C. Hohenberg and P. M. Platzman. High-Energy Neutron Scattering from Liquid He^4. *Phys. Rev.*, **152**:198, 1966.

[57] J. L. Yarnell, G. P. Arnold, P. J. Bendt, and E. C. Kerr. Excitations in Liquid Helium: Neutron Scattering Measurements. *Phys. Rev.*, 113(6):1379–1386, Mar 1959.

[58] D. G. Henshaw and A. D. B. Woods. Modes of Atomic Motions in Liquid Helium by Inelastic Scattering of Neutrons. *Phys. Rev.*, 121(5):1266–1274, Mar 1961.

[59] David M. Lee. The extraordinary phases of liquid ^{3}He. *Rev. Mod. Phys.*, 69:645–666, Jul 1997.

[60] J. Steinhauer, R. Ozeri, N. Katz, and N. Davidson. Excitation Spectrum of a Bose-Einstein Condensate. *Phys. Rev. Lett.*, **88**:120407, 2002.

[61] D. M. Stamper-Kurn, A. P. Chikkatur, A. Görlitz, S. Inouye, S. Gupta, D. E. Pritchard, and W. Ketterle. Excitation of Phonons in a Bose-Einstein Condensate by Light Scattering. *Phys. Rev. Lett.*, **83**:2876, 1999.

[62] K. J. Challis, R. J. Ballagh, and C. W. Gardiner. Bragg Scattering of Cooper Pairs in an Ultracold Fermi Gas. *Phys. Rev. Lett.*, 98:093002, 2007.

[63] J. R. Abo-Shaeer, D. E. Miller, J. K. Chin, K. Xu, T. Mukaiyama, and W. Ketterle. Coherent molecular optics using ultracold sodium dimers. *Physical Review Letters*, 94(4):040405, 2005.

[64] J. Fuchs, G. J. Duffy, G. Veeravalli, P. Dyke, M. Bartenstein, C. J. Vale, P. Hannaford, and W. J. Rowlands. Molecular Bose-Einstein condensation in a versatile low power crossed dipole trap. *J. Phys. B.*, 40:4109–4118, 2007.

[65] U. Schünemann, H. Engler, R. Grimm, M. Weidemüller, and M. Zielonkowski. Simple scheme for tunable frequency offset locking of two lasers. *Review of Scientific Instruments*, 70(1):242–243, 1999.

[66] J. Fuchs. *Molecular Bose-Einstein condensates and p-wave Feshbach molecules of* $^6Li_2$. PhD thesis, Swinburne University of Technology, 2009.

[67] C. J. Pethick and H. Smith. *Bose-Einstein Condensation in Dilute Gases*. Cambridge University Press, 2001.

[68] L. Pitaevskii and S. Stringari. *Bose-Einstein Condensation*. Oxford University Press, 2003.

[69] Anthony J. Leggett. Bose-Einstein condensation in the alkali gases: Some fundamental concepts. *Rev. Mod. Phys.*, 73(2):307–356, 2001.

[70] Stefano Giorgini, Lev P. Pitaevskii, and Sandro Stringari. Theory of ultracold atomic Fermi gases. *Reviews of Modern Physics*, 80(4):1215, 2004.

[71] S. Giorgini, L. P. Pitaevskii, and S. Stringari. Condensate fraction and critical temperature of a trapped interacting Bose gas. *Phys. Rev. A*, 54(6):R4633–R4636, Dec 1996.

[72] M. W. Zwierlein, A. Schirotzek, C. H. Schunck, and W. Ketterle. Fermionic Superfluidity with Imbalanced Spin Populations. *Science*, 311:492, 2006.

[73] Qijin Chen, C. A. Regal, D. S. Jin, and K. Levin. Finite-temperature momentum distribution of a trapped Fermi gas. *Phys. Rev. A*, 74(1):011601, 2006.

[74] C. A. Regal, M. Greiner, S. Giorgini, M. Holland, and D. S. Jin. Momentum Distribution of a Fermi Gas of Atoms in the BCS-BEC Crossover. *Phys. Rev. Lett.*, 95(25):250404, 2005.

[75] J. J. Sakurai. *Modern Quantum Mechanics*. Addison Wesley, International Student Edition, 1989.

[76] M. Bartenstein. *From Molecules to Cooper Pairs: Experiments in the BEC-BCS Crossover*. PhD thesis, Innsbruck University, 2005.

[77] D. S. Petrov. Three-body problem in Fermi gases with short-range interparticle interaction. *Phys. Rev. A*, 67(1):010703, 2003.

[78] D. S. Petrov, C. Salomon, and G. V. Shlyapnikov. Scattering properties of weakly bound dimers of fermionic atoms. *Phys. Rev. A*, 71:012708, 2005.

[79] H. J. Metcalf and P. v. d. Straten. *Laser Cooling and Trapping*. Springer-Verlag, Heidelberg, 1999.

[80] M. E. Gehm. *Preparation of an optically-trapped degenerate Fermi gas of ^{6}Li: Finding the route to degeneracy*. PhD thesis, Duke University, 2003.

[81] J. Fuchs, C. Ticknor, P. Dyke, G. Veeravalli, E. Kuhnle, W. Rowlands, P. Hannaford, and C. J. Vale. Binding Energies of ^{6}Li p-wave Feshbach Molecules. *Phys. Rev. A*, 77:053616, 2008.

[82] W. I. McAlexander, E. R. I. Abraham, and R. G. Hulet. Radiative lifetime of the $2P$ state of lithium. *Phys. Rev. A*, 54:R5–R8, Jul 1996.

[83] R. Grimm, M. Weidemüller, and Y. Ovchinnikov. Optical dipole traps for neutral atoms. *Adv. At. Mol. Opt. Phys.*, 42:95, 2000.

[84] K. M. O'Hara, M. E. Gehm, S. R. Granade, and J. E. Thomas. Scaling laws for evaporative cooling in time-dependent optical traps. *Phys. Rev. A*, 64:051403, 2001.

[85] M. J. Holland, B. DeMarco, and D. S. Jin. Evaporative cooling of a two-component degenerate Fermi gas. *Phys. Rev. A*, 61:053610, 2000.

[86] W. H. Bragg. The Secondary Radiation Produced by the Beta Rays of Radium. *Phys. Rev. (Series I)*, 30(5):638–640, May 1910.

[87] M. Kozuma, L. Deng, E. W. Hagley, J. Wen, R. Lutwak, K. Helmerson, S. L. Rolston, and W. D. Phillips. Coherent Splitting of Bose-Einstein Condensed Atoms with Optically Induced Bragg Diffraction. *Phys. Rev. Lett.*, **82**:871, 1999.

[88] J. Stenger, S. Inouye, A. P. Chikkatur, D. M. Stamper-Kurn, D. E. Pritchard, and W. Ketterle. Bragg Spectroscopy of a Bose-Einstein Condensate. *Phys. Rev. Lett.*, **82**:4569, 1999.

[89] J. Joseph, B. Clancy, L. Luo, J. Kinast, A. Turlapov, and J. E. Thomas. Measurement of sound velocity in a Fermi gas near a Feshbach resonance. *Phys. Rev. Lett.*, 98:170401, 2007.

[90] P. B. Blakie, R. J. Ballagh, and C. W. Gardiner. Theory of coherent Bragg spectroscopy of a trapped Bose-Einstein condensate. *Phys. Rev. A*, **65**:033602, 2002.

[91] C. Cohen-Tannoudji and C. Robilliard. Wave functions, relative phase and interference for atomic Bose-Einstein condensate. *C. R. Acad. Sci. Paris*, **t.2, Série IV**:445, 2001.

[92] J. Dupont-Roc C. Cohen-Tannoudji and G. Grynberg. *Atom-Photon interactions: Basic Processes and Applications*. John Wiley & Sons, Inc., New York, 1992.

[93] A. L. Fetter and J. D. Walecka. *Quantum Theory of Many-Particle Systems*. McGraw-Hill, New York, 1971.

[94] S. Richard, F. Gerbier, J. H. Thywissen, M. Hugbart, P. Bouyer, and A. Aspect. Momentum Spectroscopy of 1D Phase Fluctuations in Bose-Einstein Condensates. *Phys. Rev. Lett.*, 91(1):010405, 2003.

[95] B. H. Bransden and C. J. Joachain. *Physics of Atoms and Molecules*. Prentice Hall, 1983.

[96] S. Gupta, A. E. Leanhardt, A. D. Cronin, and D. E. Pritchard. Coherent manipulation of atoms with standing light waves. *C. R. Acad. Sci. Paris*, **t.2, Série IV**:479, 2001.

[97] G. Veeravalli, E. Kuhnle, P. Dyke, and C. J. Vale. Bragg spectroscopy of strongly interacting Fermi gas. *Phys. Rev. Lett.*, 101:250403, 2008.

[98] M. E. Gehm, S. L. Hemmer, K. M. O'Hara, and J. E. Thomas. Unitarity-limited elastic collision rate in a harmonically trapped Fermi gas. *Phys. Rev. A*, 68(1):011603, 2003.

[99] Subhadeep Gupta, Zoran Hadzibabic, James R. Anglin, and Wolfgang Ketterle. Collisions in Zero Temperature Fermi Gases. *Phys. Rev. Lett.*, 92(10):100401, 2004.

[100] Le Luo and J. E. Thomas. Thermodynamic Measurements in a Strongly Interacting Fermi Gas. *Journal of Low Temperature Physics*, 154(1-2):1–29, 2009.

[101] Qijin Chen, Jelena Stajic, and K. Levin. Thermodynamics of Interacting Fermions in Atomic Traps. *Phys. Rev. Lett.*, 95:260405, 2005.

[102] J. M. Kinast. *Thermodynamics and superfluidity of a strongly interacting Fermi gas*. PhD thesis, Duke University, 2006.

[103] Aurel Bulgac, Joaquín E. Drut, and Piotr Magierski. Thermodynamics of a Trapped Unitary Fermi Gas. *Phys. Rev. Lett.*, 99(12):120401, 2007.

[104] Hui Hu, Xia-Ji Liu, and Peter D. Drummond. Temperature of a trapped unitary Fermi gas at finite entropy. *Phys. Rev. A*, 73(2):023617, 2006.

[105] R. Haussmann, W. Rantner, S. Cerrito, and W. Zwerger. Thermodynamics of the BCS-BEC crossover. *Phys. Rev. A*, 75(2):023610, 2007.

[106] R. Haussmann and W. Zwerger. Thermodynamics of a trapped unitary Fermi gas. *Phys. Rev. A*, 78(6):063602, 2008.

Publications of the author

From the contents of this thesis and contributions to the earlier experiments:

G. Veeravalli, E. Kuhnle, P. Dyke, and C. J. Vale.
Bragg spectroscopy of strongly interacting Fermi gas,
Phys. Rev. Lett. **101**, 250403 (2008).

J. Fuchs, C. Ticknor, P. Dyke, G. Veeravalli, E. Kuhnle, W. Rowlands, P. Hannaford and C. J. Vale.
Binding Energies of ^{6}Li p-wave Feshbach Molecules,
Phys. Rev. A. **77**, 053616 (2008).

J. Fuchs, G. J. Duffy, G. Veeravalli, P. Dyke, M. Bartenstein, C. J. Vale,
P. Hannaford and W. J. Rowlands.
Molecular Bose-Einstein condensation in a versatile low power crossed dipole trap,
J. Phys. B. **40**, 4109 (2007).

Other publications during the time of this thesis:

J. W. Wadsley, G. Veeravalli, and H. M. P. Couchman.
On the treatment of entropy mixing in numerical cosmology,
MNRAS - Monthly Notices of Royal Astronomical Society. **387**, pp. 427-438 (2008).